UNIVERSIDADE FEDERAL DO RIO GRANDE DO SUL
INSTITUTO DE INFORMÁTICA
PROGRAMA DE PÓS-GRADUAÇÃO EM MICROELETRÔNICA

THIAGO HANNA BOTH

Autocorrelation Analysis in Frequency Domain as a Tool for MOSFET Low-Frequency Noise Characterization

Thesis presented in partial fulfillment
of the requirements for the degree of
PhD in Microelectronics

Advisor: Prof. Dr. Gilson Inácio Wirth

Porto Alegre
December 2017

CIP — CATALOGING-IN-PUBLICATION

Both, Thiago Hanna

Autocorrelation Analysis in Frequency Domain as a Tool for MOSFET Low-Frequency Noise Characterization / Thiago Hanna Both. – Porto Alegre: PGMICRO da UFRGS, 2017.

121 f.: il.

Thesis (Ph.D.) – Universidade Federal do Rio Grande do Sul. Programa de Pós-Graduação em Microeletrônica, Porto Alegre, BR–RS, 2017. Advisor: Gilson Inácio Wirth.

1. 1/f noise. 2. CMOS. 3. Low-frequency noise. 4. MOSFET. 5. Random Telegraph Noise. I. Wirth, Gilson Inácio. II. Título.

“One person’s data is another person’s noise.”

— K.C. COLE

ACKNOWLEDGEMENT

I would like to thank my thesis advisor, Prof. Dr. Gilson I. Wirth, for directing my scientific research over the last 9 years, starting at the undergraduate level, through the master's degree and the current thesis.

I would also like to thank NXP Semiconductors, particularly the MCSL-Eindhoven group, for the invaluable opportunity of working as an invited researcher. The staff at NXP Semiconductors in Eindhoven, the Netherlands, was extremely hospitable, providing an ideal environment for the work to flourish. Particularly noteworthy are the contributions of Dr. Andries J. Scholten and Dr. Jeroen A. Croon, who not only suggested the correlation technique presented in this work, but also knowledgeably contributed to the analyses; Adrie Zegers-van Duijnhoven, who was responsible for the low-frequency noise measurements; and Dr. Hans P. Tuinhout, whose contribution to this work far exceeds that of a colleague or a supervisor.

The assistance of my colleagues at Laprot/UFRGS also deserves mention. Dr. Fábio F. Vidor provided valuable discussions regarding the results and also revised the final draft of the thesis; Dr. Maurício Banaszeski da Silva was instrumental for the derivation of the mathematical expressions; M.Sc. Alan Carlos J. Rossetto, M.Sc. Gabriela F. Furtado, M.Sc. Pablo I. Vaz and M.Sc. Thiago Copetti also contributed with ideas and insights.

Finally, I am exceedingly thankful to my parents, Carlos Estevan and Maria Lúcia, that, through their unconditional support, allowed me to improve as a scholar and as a person; to my brother and friend, Lucas, with whom I (unwillingly) learned about sharing; and to my beloved Bruna, who has been a safe harbour and my confidant.

ABSTRACT

Low-frequency noise (LFN) is a performance limiter for analog, digital and RF circuits, introducing phase noise in oscillators and reducing the stability of SRAM cells, for example. Metal-oxide-semiconductor field-effect-transistors (MOSFETs) are known for their particularly high $1/f$ and random telegraph noise levels, whose power may be orders of magnitude larger than thermal noise for frequencies up to dozens of kHz. With the technology scaling, the corner frequency — i.e. the frequency at which the contributions of thermal and shot noises to noise power overshadow that of the $1/f$ noise — is increased, making $1/f$ and random telegraph signal (RTS) the dominant noise mechanism in CMOS technologies for frequencies up to several MHz. Additionally, the LFN levels from device-to-device can vary several orders of magnitude in deeply-scaled devices, making LFN variability a major concern in advanced MOS technologies. Therefore, to assure proper circuit design in this scenario, it is necessary to identify the fundamental mechanisms responsible for MOSFET LFN, in order to provide accurate LFN models that account not only for the average noise power, but also for its variability and dependences on geometry, bias and temperature. In this work, a new variability-based LFN analysis technique is introduced, employing the autocorrelation of multiple LFN spectra in terms of parameters such as frequency, bias and temperature. This technique reveals information about the mechanisms responsible for the $1/f$ noise that is difficult to obtain otherwise. The correlation analyses performed on three different commercial mixed-signal CMOS technologies (140-nm, 65-nm and 40-nm) provide strong evidence that the LFN of both n- and p-type MOS transistors is primarily composed of the superposition of thermally activated random telegraph signals (RTS).

Keywords: 1/f noise. CMOS. low-frequency noise. MOSFET. Random Telegraph Noise.

Análise de autocorrelação no domínio frequência como ferramenta para a caracterização do ruído de baixa frequência em MOSFETs

RESUMO

O ruído de baixa frequência é um limitador de desempenho em circuitos analógicos, digitais e de radiofrequência, introduzindo ruído de fase em osciladores e reduzindo a estabilidade de células SRAM, por exemplo. Transistores de efeito de campo de metal-óxido-semicondutor (MOSFETs) são conhecidos pelos elevados níveis de ruído $1/f$ e telegráfico, cuja potência pode ser ordens de magnitude maior do que a observada para ruído térmico para frequências de até dezenas de kHz. Além disso, com o avanço da tecnologia, a frequência de *corner* — isto é, a frequência na qual as contribuições dos ruídos térmico e shot superam a contribuição do ruído $1/f$ — aumenta, tornando os ruídos $1/f$ e telegráfico os mecanismos dominantes de ruído na tecnologia CMOS para frequências de até centenas de MHz. Mais ainda, o ruído de baixa frequência em transistores nanométricos pode variar significativamente de dispositivo para dispositivo, o que torna a variabilidade de ruído um aspecto importante para tecnologias MOS modernas. Para assegurar o projeto adequado de circuitos do ponto de vista de ruído, é necessário, portanto, identificar os mecanismos fundamentais responsáveis pelo ruído de baixa frequência em MOSFETs e desenvolver modelos capazes de considerar as dependências do ruído com geometria, polarização e temperatura. Neste trabalho é proposta uma técnica para análise de ruído de baixa frequência baseada na autocorrelação dos espectros de ruído em função de parâmetros como frequência, polarização e temperatura. A metodologia apresentada revela informações importantes sobre os mecanismos responsáveis pelo ruído $1/f$ que são difíceis de obter de outras formas. As análises de correlação realizadas em três tecnologias CMOS comerciais (140 nm, 65 nm e 45 nm) fornecem evidências contundentes de que o ruído de baixa frequência em transistores MOS tipo-n e tipo-p é composto por um somatório de sinais telegráficos termicamente ativados.

Palavras-chave: CMOS, MOSFET, Ruído 1/f, Ruído de Baixa Frequência, Ruído Telegráfico.

LIST OF ABBREVIATIONS AND ACRONYMS

ACF	Autocorrelation Function
ACM	Advanced Compact MOSFET model
BSIM	Berkeley Short-Channel IGFET model
BTI	Bias Temperature Instability
CDF	Cumulative Distribution Function
CMOS	Complementary Metal-Oxide-Semiconductor
DUT	Device Under Test
EKV	Enz-Krummenacher-Vittoz MOSFET model
FinFET	Fin Field-Effect Transistor
GR	Generation-Recombination
HEMT	High-Electron-Mobility Transistor
IGFET	Insulated-Gate Field-Effect Transistor
LDD	Light Doped Drain
LFN	Low-Frequency Noise
MOSFET	Metal-Oxide-Semiconductor Field-Effect Transistor
NFET	n-type Metal-Oxide-Semiconductor Field-Effect Transistor
PFET	p-type Metal-Oxide-Semiconductor Field-Effect Transistor
PSD	Power Spectral Density
PSP	Penn-State Phillips MOSFET model
RTN	Random Telegraph Noise
RTS	Random Telegraph Signal
SNR	Signal-to-Noise Ratio
SRAM	Static Random Access Memory
WKB	Wentzel-Kramers-Brillouin approximation

LIST OF SYMBOLS

C_{ox}	Gate oxide capacitance per unit area
E	Energy
E_B	Activation Energy
E_c	Conduction band energy level
E_f	Fermi Energy
E_{Fn}	Electron quasi Fermi energy
E_i	Intrinsic Fermi energy
E_{ox}	Electric field across the oxide
E_{sat}	Electric field at which carrier velocity saturates
E_T	Trap energy level
E_{T0}	Trap energy in flat band conditions
E_v	Valence band energy level
E_x	Electric field along the x-axis
f	Frequency in Hz
f_H	Upper limit of the bandwidth
f_L	Lower limit of the bandwidth
f_{max}	Upper limit of the observation window
f_{min}	Lower limit of the observation window
f_{ref}	Reference frequency for autocorrelation analysis
$f_{rolloff}$	Measurement system roll-off frequency
f_t	Fermi-Dirac distribution
g_{ds}	Drain-to-source transconductance
g_m	Gate-to-source transconductance
g_{mbs}	Substrate-to-source transconductance

k	Boltzmann constant in $\mathrm{eV \cdot K^{-1}}$
k_B	Boltzmann constant in $\mathrm{J \cdot K^{-1}}$
K	Normalized variance
h	Planck constant in J·s
I	Electric current
I_D	Drain current
I_0	Dark saturation current
L	Transistor Length
L_{eff}	Effective channel length
N	Surface carrier concentration Total number of traps in a device
N_l	Estimated surface carrier concentration at the drain side
N_t	Surface trap density of occupied traps
N_{tr}	Surface trap density in area and energy
N_{tr}^*	Equivalent trap density in area and energy incorporating mobility fluctuations
N_{tr}/γ'	Surface trap density in energy, area, and log-domain of time constants
$N_{t,empty}$	Average number of empty traps
$N_{t,full}$	Average number of occupied
N_0	Estimated surface carrier concentration at the source side
q	Elementary charge
Q_{inv}	Inversion layer charge
R	Resistance Coupling coefficient between carrier number fluctuation and trap occupancy
R_{DS}	Drain-to-source resistance
R_{X}	Autocorrelation function of $\mathrm{X}(t)$
S_{I_D}	Power spectral density of the drain current noise

$S_{I_D,inv}$	$1/f$ Noise power spectral density estimated in strong inversion
$S_{I_D,subVt}$	$1/f$ Noise power spectral density estimated in subthreshold region
S_N	Power spectral density of the fluctuations in the charge carriers concentration
S_{V_G}	Gate referred noise power spectral density
S_{X}	Power spectral density of $\mathrm{X}(t)$
T	Temperature
T_{ox}	Gate oxide thickness
T_{ref}	Reference Temperature for autocorrelation analysis
V_D	Potential applied across a semiconductor junction
V_{DS}	Drain-to-source voltage
$V_{DS_{sat}}$	Saturation drain-to-source voltage
V_{dseff}	Effective drain-to-source voltage
V_{FB}	Flat band voltage
V_{GS}	Gate-to-substrate voltage
V_{GS}	Gate-to-source voltage
V_{gsteff}	Effective gate-to-source voltage
$V_{GS,ref}$	Reference gate voltage for autocorrelation analysis
V_T	Estimated threshold voltage of a device population
V_{th0}	Threshold voltage of the long-channel device at zero substrate bias
W	Transistor Width
W_p	Noise power integrated over a bandwidth
x_0	Location parameter of the Cauchy-Lorentz distribution
x_{tr}	Trap position along the channel
X_{tr}	Uniformly distributed trap position along the channel
z_{tr}	Trap depth within the oxide
α	Scattering coefficient

α_H	Hooge parameter
γ	Wave function attenuation factor
γ'	Log-uniform distribution parameter
Δf	Difference between f_1 and f_2
$\Delta f'$	Ratio between f_1 and f_2
ΔI	Difference between high and low current states
ΔI_D	Drain current difference between occupied and empty trap states
$\Delta \tilde{I_D}$	Normalized drain current deviation
ε	MOSFET thermal noise bias dependent parameter
λ	Frequency exponent of the low-frequency noise power spectral density
μ	Charge carrier mobility Location parameter of the log-normal distribution
μ_{eff}	Effective charge carrier mobility
ρ	Correlation coefficient
σ	Scale parameter of the log-normal distribution
τ	Characteristic time constant
τ_c	Average capture time constant
τ_e	Average emission time constant
τ_{max}	Maximum characteristic time constant in the defined bandwidth
τ_{min}	Minimum characteristic time constant in the defined bandwidth
τ_o	Lowest possible characteristic time constant
τ_0	Time spent at low current state
τ_1	Time spent at high current state
ϕ_s	Surface potential
ψ	Scale parameter of the Cauchy-Lorentz distribution
ω	Angular frequency

LIST OF FIGURES

LIST OF TABLES

CONTENTS

1 INTRODUCTION

The word *noise* is used to describe a plethora of phenomena that are (usually) unwanted. Commonly, *noise* refers to acoustic noise, which is characterized by disturbing, often loud, sounds, caused by e.g. traffic, aircraft, machines and bad musicians. Physically, noise and sound are indistinguishable; both are propagating mechanical waves of pressure. There is, therefore, an innate subjectivity in acoustic noise, i.e. what is agreeable and what is not to human hearing. The 1980 track by Australian band AC/DC, entitled *Rock and Roll ain't noise pollution*, plays on this idea by implying that their music, though loud and disturbing to some, is not *noise*.

Even though acoustic noise is certainly the most recognizable form of *noise*, several other fields — such as electronics, physics, biology and economy — are familiarized with the concept. And while the word *noise* usually carries the stigma of unwantedness, it is certainly not always the case: in computer graphics, for example, gradient and value noises (e.g. Perlin Noise) are widely employed for procedural generation of textures; in physics, Albert Einstein demonstrated in one of his works during the *Annus Mirabilis* of 1905 that the Avogadro number could be derived from a stochastic quantity (Brownian motion) (COHEN, 2005).

In electronics, however, *noise* is understood as undesirable fluctuations in measurable quantities, such as current and voltage. These fluctuations carry no meaningful information, and may obscure a signal. Using the acoustic analogy, imagine trying to convey a message to a friend on the other side of a bar. If the bar is empty and silent, it is easy to convey the message as the speech is easily audible. On the other hand, if the bar is crowded and loud, transmitting the information becomes difficult, meaning the transmitter may need to shout. In electronics the same is valid: transmitting a signal through a noisy medium requires a larger signal, i.e. more signal power.

Interestingly, the randomness and unpredictability are fundamental properties of both information and noise (HAYKIN; MOHER, 2007). If one could predict information, there would be no need to communicate it, as the receiver would be able to foresee it. Similarly, were the receiver able to predict noise, then the receiver would be able to remove the noise, negating its effects. The goal is, thus, to separate noise from information to the maximum extent possible (HAYKIN; MOHER, 2007).

Regarding its origins, noise in electronics can rise from external and internal sources. External sources cause deterministic disturbances due to electromagnetic and

electrostatic effects. One common example of this kind of noise is the crosstalk between telephone lines; the coupling between the lines causes the signal from one line to disturb another. This disturbance is not truly random, but may obscure the information on the line nonetheless. Internal sources, on the other hand, are stochastic processes, i.e. the value of the disturbance is random at any given time. The most fundamental example of internal noise source in electronics is the thermal noise (also known as Johnson or Nyquist noise), caused by the random-walk of electrons due to thermal agitation. Chapter 3 of this work provides a deeper discussion on the fundamental noise sources in electronics.

Due to its stochastic (i.e. random) nature, it is convenient to describe noise from internal sources using statistical quantities. While observing the probability density function and the autocorrelation function of noise signals are possible methods, the primary metric for noise analysis used in this work is the power spectral density (PSD), which provides the amount of noise power per unit frequency. It is possible to categorize noise based on its PSD behaviour; this classification is referred to as **colours of noise**. Typically, noise can be white, pink, blue, brown and violet. Noise sources that have a constant power over a bandwidth (that is, the power is independent of the frequency) are called white; those whose power decreases with $1/f$ and $1/f^2$ factors over the bandwidth are called pink and brown, respectively; those whose power increases with f and f^2 factors over the bandwidth are called blue and violet, respectively. This work focus mainly on pink noise, also known as $1/f$ noise or flicker noise.

Fluctuations with a $1/f$ power spectrum have been reported from voltages and currents in diodes and vacuum tubes; to frequency of quartz oscillators; average seasonal temperature; annual amount of rainfall; rate of traffic flow; rate of insulin take by diabetics; economic data; loudness and pitch of music; flow of the river Nile; and luminosity of stars (KESHNER, 1982; BAK; TANG; WIESENFELD, 1987). The observation of $1/f$ noise in a multitude of systems has led Bak, Tang and Wiesenfeld (1987) to propose a model for ubiquitous $1/f$ noise based on self-organized criticality, though Jensen, Christensen and Fogedby (1989) claimed that such model produces a $1/f^2$ spectrum.

Due to the $1/f$ decay of pink noise, lower frequencies contribute more significantly to noise power than higher frequencies. Thus, $1/f$ noise is one of the major components of low-frequency noise (LFN) in integrated circuits. Other important components of LFN are the random telegraph signal (RTS) and generation-recombination noise. These components will be further discussed in Chapters 3 and 4.

From a designers perspective, low-frequency noise is a performance limiter for

analog, digital and RF circuits. Providing accurate LFN models that account not only for the average noise power but also for variability and its dependences on geometry, bias and temperature is therefore imperative for proper circuit design.

Historically, two main schools of thought have emerged to explain the $1/f$ behaviour of the LFN power-spectral density in metal-oxide-semiconductor field-effect transistors (MOSFETs). The first assumes the origin of the LFN is related to the capture and emission of charge carriers by defects (traps) (MCWHORTER, 1957), and it is commonly referred to as number fluctuation theory. The second attributes the LFN to bulk mobility fluctuations (HOOGE, 1969), being referred to as mobility fluctuation theory.

While trapping/de-trapping has emerged as the prevalent model in recent years, the trapping mechanism itself is not thoroughly understood. While studies on random telegraph signals and $1/f$ noise (SURYA; HSIANG, 1988; KIRTON; UREN, 1989) suggest a thermally activated process, direct tunnelling (MCWHORTER, 1957), which is essentially temperature independent, is still the basis of the LFN in compact models, such as BSIM and PSP (HUNG et al., 1990b; HUNG et al., 1990c).

In this work, a novel technique, based on the analysis of the autocorrelation of numerous LFN power-spectra density measurements, is introduced. The analyses reveal the statistical relationship between the LFN levels at a given frequency and temperature compared to their levels under different conditions. It is shown that the correlation coefficient is extremely sensitive to the physical mechanisms assumed for interpreting and modelling the LFN PSD. Consequently, it proves possible to draw valuable conclusions about the frequency dependence of the fundamental noise sources causing the $1/f$ noise, as well as the origin of the trapping mechanism (tunnelling/thermal activation).

The analyses presented in this work were performed on measured LFN data from n- and p-type MOS transistors in 140-nm, 65-nm and 40-nm mixed-signal CMOS technologies. The results provide strong evidence for a unified description of N- and PFET LFN in terms of thermally activated random telegraph signals, providing a statistical approach to the classical work of Dutta and Horn (1981).

This work is organized as follows: the introductory chapters 2 and 3 provide a mathematical background for noise analysis, and a brief discussion on the fundamental noise sources in electronics, respectively. An in-depth review of MOSFET LFN modelling is presented in chapter 4, followed by a discussion on the temperature dependence of MOSFET LFN in chapter 5. In chapter 6, the noise measurement set-up as well as important noise quantities (such as expected value and variance) from commercial mixed-

signal CMOS technologies are displayed. The autocorrelation technique proposed for LFN analysis is discussed in chapter 7 and applied for several case studies. The closing remarks of this work are presented in chapter 8.

2 MATHEMATICAL REPRESENTATION OF NOISE

The study of noise in electronics consists in the analysis of random, unwanted, electric signals in devices, circuits and systems, aiming at providing an useful description of these processes for circuit designers. However, due to the stochastic nature of most noise processes (e.g. thermal noise), detailed knowledge about the time variation of a random signal is unavailable, meaning that it is not possible to predict exactly what waveform will be observed in the future.

For this reason, to deal with noise one must speak in terms of probabilities and statistical properties in order to convey a useful description of the process. The purpose of this chapter is to provide a brief introduction on the mathematical description of noise, in particular the definition of the *power spectral density*, which is the primary noise quantity analysed in this work.

The discussion in this chapter will consider only real-valued random processes.

2.1 Random Processes

A *random process* or *stochastic process*, $X(t)$, is a time-varying function which, due to randomness, can have many outcomes. Each outcome is a time function known as *sample function*, $x(t)$. The collection of all possible outcomes of an experiment is called the *sample space* or *ensemble* (CARLSON; CRILLY, 2010; LATHI; DING, 2009).

When the statistical characteristics of the random process are independent of time, the process is described as being *stationary*. It is said to be *strictly stationary* if the joint distribution of any set of random variables obtained by observing the random process $X(t)$ is independent of the location of the origin $t = 0$ (HAYKIN; MOHER, 2007), and wide-sense stationary if the average is independent of time and the autocorrelation function, $R_X(t, t+s)$, depends only on the time difference s (CARLSON; CRILLY, 2010), that is

$$\mathrm{E}[X(t)] = \text{constant} \tag{2.1}$$

and

$$R_X(t, t+s) = R(s)\ , \tag{2.2}$$

where **E** is the expected value operator.

2.2 Autocorrelation Function of a Random Process

Even though random processes are unpredictable by definition, similarities between samples of the process at different times may be observed, meaning they are correlated (HAYKIN; MOHER, 2007). The autocorrelation function (ACF) is the mathematical description of the similarity between observations of a random process with a certain lag in time. In other words, it describes the rapidity of the amplitude change of a signal in time (LATHI; DING, 2009).

For a generic wide-sense stationary random process, $\mathrm{X}(t)$, the autocorrelation function between times t and s, $R_{\mathrm{X}}(t,t+s)$, is given by

$$R_{\mathrm{X}} = \mathrm{E}\left[\mathrm{X}(t)\cdot\mathrm{X}(t+s)\right] \ . \tag{2.3}$$

If the ensemble average of the random process $X(t)$, $\mathrm{E}[X(t)]$ is equal to the time average of any sample function, $\langle x(t)\rangle$; and the autocorrelation function of the process, $R_X(t,t+s)$, is equal to the time autocorrelation function of any sample function, so that

$$\mathrm{E}[X(t)] = \langle x(t)\rangle \ , \tag{2.4}$$

$$\mathrm{E}\left[X(t)\cdot X(t+s)\right] = \langle x(t)\cdot x(t+s)\rangle \ , \tag{2.5}$$

the process is defined as *ergodic*.

For an ergodic wide-sense stationary random process

$$R_{\mathrm{X}}(s) = \lim_{T\to\infty}\frac{1}{2T}\int_{-T}^{T} x(t)\cdot x(t+s)dt \ . \tag{2.6}$$

It is worth noting that the ACF of a wide-sense stationary random process is maximum at the origins, i.e. $R_{\mathrm{X}}(0) \geq |R_{\mathrm{X}}(s)|$, and that its value at the origin is equal to the mean-square value of the random process, i.e. $R_{\mathrm{X}}(0) = \mathrm{E}\left[\mathrm{X}(t)^2\right]$ (HAYKIN; MOHER, 2007).

2.3 Power Spectral Density

The power spectral density describes the amount of power per unit frequency (Hz) of a given signal or random process. In order to determine the PSD of a random process from the sample function $x(t)$, it is necessary to define its Fourier transform. However, since power signals have infinite energy, the sample function may not be Fourier transformable (HAYKIN; MOHER, 2007). To overcome this limitation, the following steps are taken: consider the finite-duration (truncated) version of the sample function of an ergodic stationary process, given by

$$x_T(t) = \begin{cases} x(t), & \text{if } |t| < T/2 \\ 0, & \text{if } |t| > T/2 \, . \end{cases} \tag{2.7}$$

As long as T is finite, the truncated sample function, $x_T(t)$ has finite energy, which enables the determination of its Fourier transform $X_T(f)$. The *energy spectral density* of $x_T(t)$ is given by $|X_T(f)|^2$ and the average power, P_X, from Rayleigh's energy theorem (Parseval's Theorem), in the form of

$$\int_{-T/2}^{T/2} x^2(t)dt = \int_{-\infty}^{\infty} x_T(t)dt = \int_{-\infty}^{\infty} |X_T(f)|^2 df, \tag{2.8}$$

is given by

$$P_X = \lim_{T\to\infty} \frac{1}{T} \int_{-\infty}^{\infty} \mathrm{E}\left[x_T(t)^2\right] dt = \lim_{T\to\infty} \frac{1}{T} \int_{-\infty}^{\infty} \mathrm{E}\left[|X_T(f)|^2\right] df \, . \tag{2.9}$$

Notice that, as T increases, the energy in $x_T(t)$ also increases. Correspondingly, $|X_T(f)|^2$ increases with T and, as $T \to \infty$, so will $|X_T(f)|^2 \to \infty$. However, since that average power has to be finite, $|X_T(f)|^2$ must approach infinity at the same rate as T. This convergence allows the interchange between the limiting operation and the integration in the right-hand side of (2.9) (CARLSON; CRILLY, 2010; HAYKIN; MOHER, 2007; LATHI; DING, 2009), that is

$$P_X = \lim_{T\to\infty} \int_{-\infty}^{\infty} \frac{1}{T} \mathrm{E}\left[|X_T(f)|^2\right] df = \int_{-\infty}^{\infty} \lim_{T\to\infty} \frac{1}{T} \mathrm{E}\left[|X_T(f)|^2\right] df \, . \tag{2.10}$$

The *power spectral density* is then defined as

$$S_X = \lim_{T\to\infty} \frac{1}{T} \mathrm{E}\left[|X_T(f)|^2\right] \ , \tag{2.11}$$

and, consequently,

$$P_X = \int_{-\infty}^{\infty} S_X(f) df \ . \tag{2.12}$$

Following to the Wiener-Khinchine theorem (HAYKIN; MOHER, 2007; LATHI; DING, 2009; CARLSON; CRILLY, 2010), the PSD of a random process, $S_{\mathrm{X}}(f)$, is related to the autocorrelation function of the process, $R_{\mathrm{X}}(\tau)$, by the Fourier transform

$$S_{\mathrm{X}}(f) = \int_{-\infty}^{\infty} R_{\mathrm{X}}(s) \cdot e^{-j2\pi f\tau} ds \ , \tag{2.13}$$

$$R_{\mathrm{X}}(s) = \int_{-\infty}^{\infty} S_{\mathrm{X}}(f) \cdot e^{j2\pi f\tau} df \ . \tag{2.14}$$

which may be simplified for even, real-valued, functions in the form of

$$S_{\mathrm{X}}(f) = \int_{-\infty}^{\infty} R_{\mathrm{X}}(s) \cdot \cos(2\pi fs) ds \ , \tag{2.15}$$

$$R_{\mathrm{X}}(s) = \int_{-\infty}^{\infty} S_{\mathrm{X}}(f) \cdot \cos(2\pi fs) df \ . \tag{2.16}$$

Even though the PSD and the ACF contain, essentially, the same information about the noise source, the former is more commonly used to describe its behaviour. The reasons for that include the convenience of working in frequency-domain and the ease of determining the power within a bandwidth, required for signal-to-noise ratio (SNR) estimation.

2.3.1 Power Spectral Density Estimation

The problem of PSD estimation consists of obtaining, from a finite record of stationary data sequence, how the total power is distributed over frequency. There are two broad approaches to spectral analysis: the first, called non-parametric, is based entirely

on the definition of the PSD (2.11), which, for discrete-time data can be rewritten as

$$S_X = \lim_{N\to\infty} \frac{1}{N} \mathrm{E}\left[X[k]\right]^2; \tag{2.17}$$

the second, postulates a model for the data, providing a means to parametrize the spectrum, thereby reducing the spectral estimation problem to that of estimating the parameters in the assumed model.

The more common non-parametric estimators are the *periodogram* and the *correlogram*. The periodogram relies on the definition (2.17), neglecting the expected value and limit operations, such that

$$\tilde{S}_X = \frac{1}{N} \sum_{n=1}^{N} x[n] \cdot e^{-j2\pi f n}, \tag{2.18}$$

where $x[n]$ and $\tilde{S}_X$ are the sampled signal, and the PSD estimate, respectively.

The correlogram, on the other hand, uses the definition (2.13), so that

$$\tilde{S}_X = \sum_{k=-(N-1)}^{N-1} R[k] \cdot e^{-j2\pi k}, \tag{2.19}$$

where $R[k]$ and $\tilde{S}_X$ are covariance lag obtained from the sampled function (equivalent to the autocorrelation function), and the PSD estimate

Notice, however, that both the periodogram and the correlogram are poor estimates of the PSD (STOICA; MOSES, 1997). To circumvent the natural limitations of the periodogram, several periodogram-based methodologies have been proposed. Examples include the Bartlett (1950) method — which consists of splitting the available sample of N observations into $L = N/M$ subsamples of M observations each, and then averaging the periodograms obtained from the subsamples for each value of f —, and the Welch (1967) method — which is similar to the Bartlett method, but the data segments are allowed to overlap.

3 FUNDAMENTAL NOISE SOURCES IN ELECTRONICS

In order to properly address and model noise in integrated circuits it is necessary to identify the individual noise sources in electronic devices. Primarily, disturbances can originate from external sources — due to electrostatic and electromagnetic interaction — and from internal sources, i.e. random fluctuations in the physical mechanisms that govern electron transport. In this chapter, and henceforth in this work, the term *noise* will refer to the latter (internal sources).

The following sections provide a background on the fundamental noise sources present in electronics, which are: thermal noise, shot noise, generation-recombination noise (GR noise), random telegraph signal and $1/f$ noise.

3.1 Thermal Noise

The thermal noise is a broadband white noise — i.e. it has a constant power spectral density — that arises from the random motion of electron and is present in any passive resistor above absolute zero temperature, even without bias applied. Experimentally reported by Johnson (1928) and theoretically explained by Nyquist (1928), the thermal noise is also known as Johnson or Nyquist noise.

Each time an electron is scattered, its velocity is randomized; therefore, instantly, there could be a number of electrons flowing in a given direction, resulting in a small net current. Due to its random characteristic, this current fluctuates in amplitude and direction, but its expected value is always zero (HAARTMAN; ÖSTLING, 2007). The PSD of the thermal noise of a piece of material with resistance R and at a temperature T can be written as

$$S_I = \frac{4k_B T}{R} \,, \tag{3.1}$$

where k_B is the Boltzmann constant in Joules per Kelvin.

Notice, from (3.1), that the thermal noise in an ideal resistor is *white*, i.e. its intensity is constant throughout the frequency spectra. This approximation, however, is only valid if $k_B T \gg hf$ (where h and f are the Planck constant in J·s and f in Hz, respectively). At low temperatures and high frequencies, quantum effects become relevant

and the more general expression

$$S_I = 4 \cdot \frac{hf}{\exp\left(\frac{hf}{k_B T}\right) - 1} \cdot \frac{1}{R}\,, \tag{3.2}$$

proposed by Nyquist (1928), must be used. Note that if $k_B T \gg hf$, the quantum correction factor reduces to $k_B T$, resulting in equation (3.1).

For long-channel MOS transistors, the thermal noise can be estimated using

$$S_{I_D} = 4 k_B T \varepsilon g_m \tag{3.3}$$

where g_m is the small-signal transconductance and at the bias point and ε is a bias dependent parameter ($\varepsilon = 1/2$ for weak inversion and $\varepsilon = 2/3$ for strong inversion) (TEDJA; SPIEGEL; WILLIAMS, 1994).

From a transistor modelling perspective, the BSIM4 equation model provides two methods for channel thermal noise calculation: a charge-based model and an holistic model, whose schematics are shown in figure 3.1.

Figure 3.1: Schematics for the BSIM4 channel thermal noise modelling for the a) charge-based model and b) holistic model.

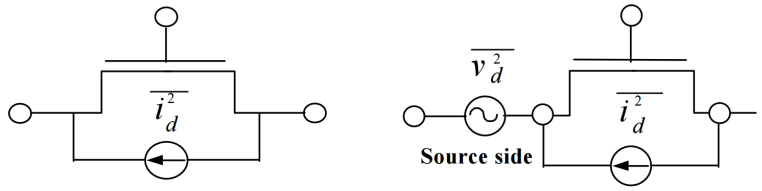

(a) ***tnoiMod*** = 0 (b) ***tnoiMod*** = 1

Source: BSIM4.6.0 MOSFET Manual (2006).

The charge-based model estimates the noise current using

$$\overline{i_d^2} = \frac{4 k_B T \Delta f}{R_{DS}(V) + \frac{L_{eff}^2}{\mu_{eff} |Q_{inv}|}} \cdot NTNOI\,, \tag{3.4}$$

where Δf is the system bandwidth, $R_{DS}(V)$ is the bias-dependent light doped drain (LDD) source-drain resistance, L_{eff} is the effective channel length, μ_{eff} is the effective carrier mobility, $NTNOI$ is a fitting parameter for short-channel devices, and Q_{inv} is the inversion layer charge.

Conversely, the holistic model estimates the thermal noise incorporating short-channel and velocity saturation effects, the thermal noise amplification through gate and substrate transconductances (g_m and g_{mbs}, respectively), as well as the induced-gate noise

with partial correlation to the channel thermal noise. The noise voltage partitioned to the source is given by

$$\overline{v_d^2} = 4k_B T \theta_{tnoi}^2 \cdot \frac{V_{dseff}\Delta f}{I_{ds}} \tag{3.5}$$

whereas the noise current source in the channel region is given by

$$\overline{i_d^2} = 4k_B T \cdot \frac{V_{dseff}\Delta f}{I_{ds}} \cdot [g_{ds} + \beta_{tnoi} \cdot (g_m + g_{mbs})]^2 - \overline{v_d^2} \cdot (g_m + g_{ds} + g_{mbs})^2 \tag{3.6}$$

where

$$\theta_{tnoi} = RNOIB \cdot \left[1 + TNOIB \cdot L_{eff} \cdot \left(\frac{V_{gsteff}}{E_{sat}L_{eff}}\right)^2\right] \tag{3.7}$$

$$\beta_{tnoi} = RNOIA \cdot \left[1 + TNOIA \cdot L_{eff} \cdot \left(\frac{V_{gsteff}}{E_{sat}L_{eff}}\right)^2\right] \tag{3.8}$$

and V_{dseff} is the effective voltage between drain and source; I_{ds} is the drain current; g_{ds} is the drain transconductance; V_{gsteff} is the the effective gate voltage subtracted of the threshold voltage; E_{sat} is the critical electric field at which the carrier velocity becomes saturated; $TNOIA$ and $TNOIB$ are the channel-length dependence of the total channel thermal noise and the channel thermal noise partitioning, respectively; and *RNOIA* and *RNOIB* are model parameters (DUNGA et al., 2006).

From a designer's perspective, thermal noise from resistive elements is unavoidable, but it is possible to minimize it through clever circuit design. Reactive elements, for example, do not generate thermal noise. Therefore, input matching techniques using reactive elements can be used to reduce thermal noise. Also, narrowing the system bandwidth reduces the thermal noise power. Finally, noise cancelling techniques have also been proposed to mitigate the thermal noise (BRUCCOLERI; KLUMPERINK; NAUTA, 2004).

3.2 Shot Noise

Due to the discrete nature of charge carriers (electrons), which have a quantized charge equal to the elementary charge, the current flow through a potential barrier, like a *pn* junction is not continuous; thus, shot noise current is generated when electrons flow independently and at random through the barrier (HAARTMAN; ÖSTLING, 2007). Simply put, if one could "observe" the flow of carriers through a barrier for an ensemble of

time intervals, the average number of carriers flowing in each interval would represent the DC current whereas the deviation from this average for each time interval would represent the shot noise current.

This effect was first described in the context of vacuum tubes by Schottky (1918). Since the shot noise is related to the corpuscular nature of the current flow through a potential barrier, a current is imperative for the existence of shot noise. The PSD of the shot noise can be expressed as

$$S_I = 2qI \tag{3.9}$$

where I is the DC current across the barrier and q is the elementary electron charge. From equation (3.9), the shot noise PSD is constant with frequency, resulting in a white noise spectrum.

For an ideal *pn* junction, the current flowing through the potential barrier is given by

$$I = I_0 \left[\exp\left(\frac{qV_D}{k_B T}\right) - 1 \right] \tag{3.10}$$

where I_0 is the dark saturation current and V_D is the potential applied across the junction. From equation (3.10), when no bias is applied, the forward and backward components of the current cancel each other, resulting in zero net current. The shot noise, however, is not zero; the total shot noise is given by the contributions to the shot noise of the forward and backward currents separately, as

$$S_I = 2qI_0 \cdot \exp\left(\frac{qV_D}{k_B T}\right) + 2qI_0, \tag{3.11}$$

hence, for $V_D = 0$

$$S_I = 4qI_0. \tag{3.12}$$

3.3 Generation-Recombination Noise

The generation-recombination (GR) noise in semiconductors originates from random transitions of the charge carriers between electronic states, which causes the number of free carriers available for current transport to fluctuate. These transitions occur not only between the valence and conduction bands, but also between the bands and localized states (bulk traps) within the semiconductor forbidden gap (SAH; NOYCE; SHOCKLEY, 1957).

These energy states exist due to various defects, such as the presence of impurities in the semiconductor and imperfections in its crystalline structure, and may be neutral or charged in its empty state. From the work of Sah, Noyce and Shockley (1957), there are four basic processes involved in the carrier generation and recombination. If an energy state is occupied by a hole, it may either emit the hole to the valence band or capture an electron from the conduction band to recombine with the hole; if it is occupied by an electron, it may either emit the electron to the conduction band or capture a hole from the valence band to recombine with the electron. These processes are illustrated in figure 3.2, where E_v, E_c and E_T are the top of the valence band, the bottom of the conduction band and the trap energy level, respectively.

Figure 3.2: Basic processes involved in the generation and recombination of carriers through traps. From left to right: a) electron capture; b) electron emission; c) hole capture; d) hole emission. Processes a) and c) result in recombination of a charge carrier; processes b) and d) result in generation of a charge carrier.

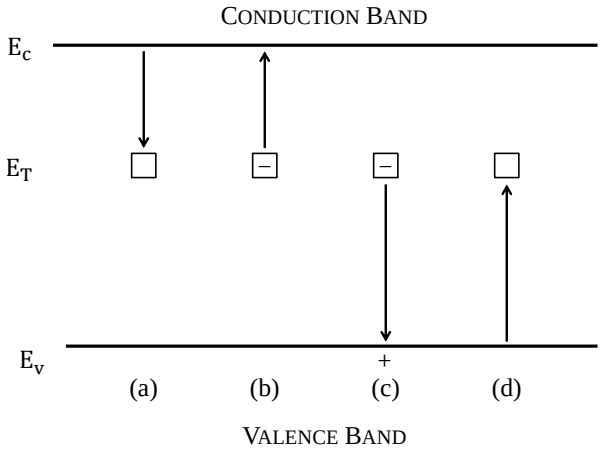

Source:Adapted from Sah, Noyce and Shockley (1957)

The GR noise is more significant for bulk traps located near the Fermi level, within few k_BT; if the Fermi level is far above or below the trap level, the trap will be filled or empty for the majority of the time, thus it will rarely transition. The PSD of the fluctuations in the number of carriers are given by

$$S_N(f) = 4\overline{\Delta N^2} \cdot \frac{\tau}{1+(2\pi f\tau)^2} \tag{3.13}$$

where τ is the time constant of the transitions and $\overline{\Delta N^2}$ is the variance, which can be

expressed as

$$\frac{1}{\overline{\Delta N^2}} = \frac{1}{N} + \frac{1}{N_{t,full}} + \frac{1}{N_{t,empty}} \tag{3.14}$$

where $N_{t,full}$ and $N_{t,empty}$ are the average number of full and empty traps, respectively (HAARTMAN; ÖSTLING, 2007). The spectrum given by (3.13) is called a *Lorentzian* due to its similarity with the probability density function of the Lorentz(ian) distribution (also known as Cauchy and Cauchy-Lorentz distribution), with parameters x_0 and ψ, shown in equation (3.15) for the sake of completion. The Lorentzian has a constant PSD for frequencies below the characteristic time constant, $1/\tau$, and decreases with $1/f^2$ for frequencies above $1/\tau$.

$$f(x;x_0,\psi) = \frac{1}{\pi\psi\left[1+\left(\frac{x-x_0}{\psi}\right)^2\right]} \tag{3.15}$$

3.4 Random Telegraph Signal

The random telegraph signal, also known as random telegraph noise (RTN), is a special case of GR noise (HAARTMAN; ÖSTLING, 2007). In MOS transistors, the telegraphic noise is characterized by discrete fluctuations in the channel conduction, producing a random telegraph signal (RTS). These fluctuations occur due to capture and emission of charge carriers by defects (traps) located in the oxide and at the oxide-semiconductor interface of these devices (KIRTON; UREN, 1989; HUNG et al., 1990a). Figure 3.3 illustrates the effect of RTS in the drain current of a MOS transistor under constant bias.

Figure 3.3: Random telegraph signal observed in the drain current of a transistor due to capture and emission of carriers by a single trap.

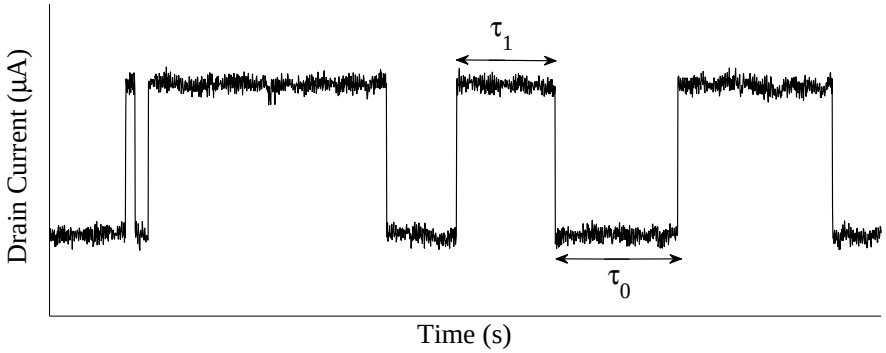

According to Yamamoto (2004), it can be demonstrated that the times spent at the high and low current states (τ_1 and τ_0, respectively) are exponentially distributed,

resulting in a Poisson process. For an ergodic process, the average time the signal spends at the high current state, $\langle \tau_1 \rangle$, is given by

$$\int_0^\infty t p_1(t) dt = \langle \tau_1 \rangle = \overline{\tau_1} \,, \tag{3.16}$$

where $\overline{\tau_1}$ is the ensemble average of τ_1 and $p_1(t)$ is the probability that state 1 will not transition between times 0 and t; the standard deviation is given by

$$\left[\int_0^\infty t^2 p_1(t) dt - \overline{\tau_1}^2 \right]^{\frac{1}{2}} = \langle \tau_1 \rangle = \overline{\tau_1} \,. \tag{3.17}$$

In essence, despite the inherent similarities between GR noise and RTS — as it will be discussed in the following chapter, RTS can also be modelled using (3.13) —, the first originates in the semiconductor bulk, whereas the latter originates from trapping in the oxide and at the oxide-semiconductor interface.

Random telegraph signals are usually observed in small-area devices for two main reasons: *i*) the reduced number of traps in these devices makes it easier to identify the two-level signal; and *ii*) the trap impact on the drain current is increased in small-area devices. Under certain circumstances (such as high drain bias), however, it is also possible to observe RTS in larger devices.

3.5 $1/f$ Noise

The $1/f$ noise, also known as flicker or pink noise, is characterized by fluctuations whose PSD have a $1/f^{\lambda}$ dependence, being $\lambda \approx 1$. Figure 3.4 shows noise PSD of a large-area NFET under uniformly charged channel conditions, which approximately follows the $1/f$ behaviour.

Given its importance, several MOSFET $1/f$ noise models have emerged over the last decades, assuming different physical mechanisms to explain its bias, area and temperature behaviour. These models, as well as the physical mechanisms underlying the $1/f$ noise, are discussed in detail in chapter 4.

To put the importance of the $1/f$ noise into perspective, the predicted thermal and shot noises are in the order of 10^{-23} A^2/Hz for the device shown in Figure 3.4. Thus, the corner frequency (the frequency at which the contributions of the shot and thermal noises

Figure 3.4: Measured LFN PSD of a large-area NFET (140-nm technology). The frequency exponent (λ), measured between 10 Hz and 30 Hz, is approximately 1.176. Bias conditions are $V_{DS} = 0.1$ V and $V_{GS} = 1.8$ V.

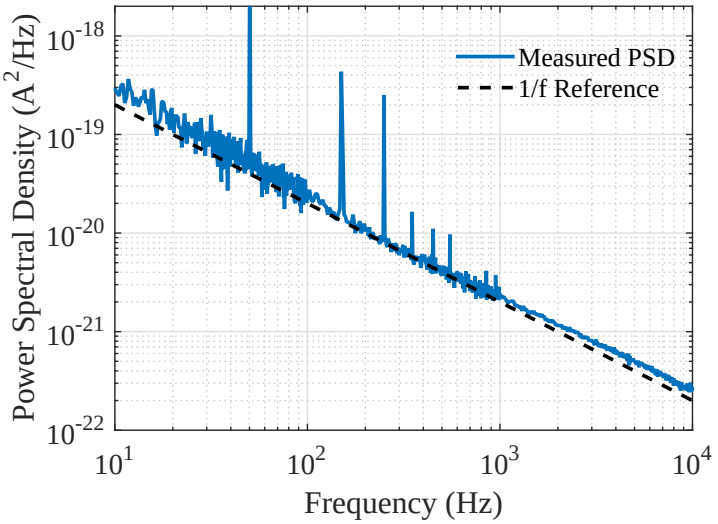

become more relevant than that of the $1/f$ noise) is expected to be between 10 kHz and 100 kHz. With the technology scaling, the corner frequency is further increased, making the $1/f$ noise the dominant noise mechanism, together with the RTS, in deeply-scaled CMOS technologies.

Throughout most of this work, a normalized noise PSD quantity is used, i.e. S_{I_D}/I_D^2 in Hz^{-1}. While this quantity is useful for the analysis proposed, from a designer's perspective, however, the input referred noise (or gate referred noise) provides better information. The conversion from drain current noise to gate referred noise is straightforward through

$$S_{V_G} = \frac{S_{I_D}}{g_m^2}, \tag{3.18}$$

where g_m is the transistor transconductance.

4 LOW-FREQUENCY NOISE MODEL IN MOSFETS

The modelling of LFN in MOSFET requires understanding of fundamental physical mechanisms responsible for the current fluctuations. The first section of this chapter presents the mathematical description of the RTS, critical for the derivation of the RTS-based $1/f$ noise model presented in section 4.2.4, which states that $1/f$ noise and RTS originate from the same physical mechanism: capture and emission of charges by traps (MCWHORTER, 1957; KIRTON; UREN, 1989; BANASZESKI DA SILVA et al., 2014). On the opposite hand, bulk mobility fluctuation models, more prominently the model by Hooge (1969), state that the $1/f$ noise and RTS have different origins.

In this chapter, the conventionally used RTS model as well as popular $1/f$ noise models are presented and discussed.

4.1 Random Telegraph Noise Model

The PSD of a telegraphic signal can be calculated based on its capture and emission time constants, as presented by Machlup (1954). From the Wiener-Khintchine theorem, the PSD of an ergodic, wide-sense stationary, random process, $S(f)$, can be obtained through the Fourier transform of the autocorrelation function of the process, $R(s)$, according to

$$S(f) = 4\int_0^\infty R(s)\cdot\cos(2\pi fs)ds\ . \tag{4.1}$$

From Machlup (1954), the autocorrelation function of a random telegraph process can be described by

$$R(s) = \sum_i\sum_j x_i\cdot x_j\cdot\{\text{prob. that } x(t)=x_i\}\cdot\{\text{prob. that } x(t+s)=x_j, \text{ given that } x(t)=x_i\}\ , \tag{4.2}$$

where x_i and x_j are the possible values for the telegraphic signal; $x(t)$ and $x(t+s)$ are the values of the telegraphic signal at times t and $t+s$, respectively; and i and j are the indexes of the RTS states (0 being the low state and 1 being the high state). The probability that, at any given time, the RTS in state 1 is given by

$$p_{x=1} = \frac{\overline{\tau_1}}{\overline{\tau_1}+\overline{\tau_0}}\ , \tag{4.3}$$

whereas the probability of being in state 0 is given by

$$p_{x=0} = \frac{\overline{\tau_0}}{\overline{\tau_1} + \overline{\tau_0}} \ , \tag{4.4}$$

being $\overline{\tau_1}$ and $\overline{\tau_0}$ the average times spent on states 1 and 0, respectively.

By assuming that $x_0 = 0$ and $x_1 = \Delta I$, where ΔI is the difference between the current between states 1 (high) and 0 (low), three out of the four summation terms in (4.2) are cancelled, reducing it to

$$R(s) = \Delta I^2 \cdot \frac{\overline{\tau_1}}{\overline{\tau_1} + \overline{\tau_0}} \cdot P_{11}(s) \ , \tag{4.5}$$

where $P_{11}(s)$ is the probability that the signal remains on state 1 after time s, that is, an even number of transitions occur during time s, starting at state 1. Taking $P_{01}(s)$ as the probability of an odd number of transitions occurring in a given time s, starting at state 1, from the Law of Total Probability

$$P_{11}(s) + P_{01}(s) = 1 \ . \tag{4.6}$$

The probability of an even number of transitions, P_{11}, at a given time $s + ds$ — being ds a sufficiently small time step so that the probability of more than one transition occurring is negligible — is comprised of two mutually exclusive probabilities: *i)* the probability of an odd number of transitions during time t, $P_{01}(s)$, followed by one transition during ds; *ii)* the probability of an even number transitions during time t, $P_{11}(s)$, and no transitions during ds. This probability can be written in differential form as

$$P_{11}(s+ds) = P_{10}(s) \cdot \frac{ds}{\overline{\tau_0}} + P_{11}(s) \cdot \left(1 - \frac{ds}{\overline{\tau_1}}\right) \ . \tag{4.7}$$

Substituting (4.6) in (4.7) and applying the limit $ds \to 0$, results in

$$\frac{d}{ds}\left[P_{11}(s+ds)\right] + \left(\frac{1}{\overline{\tau_0}} + \frac{1}{\overline{\tau_1}}\right) \cdot P_{11}(s) = \frac{1}{\overline{\tau_0}} \tag{4.8}$$

which can be solved for the initial condition $P_{11}(0) = 0$, since there can be no transitions at time 0, yielding

$$P_{11}(s) = \frac{\overline{\tau_1}}{\overline{\tau_0} + \overline{\tau_1}} + \frac{\overline{\tau_1}}{\overline{\tau_0} + \overline{\tau_1}} \cdot \exp\left[-\left(\frac{1}{\overline{\tau_0}} + \frac{1}{\overline{\tau_1}}\right) \cdot s\right] \ . \tag{4.9}$$

Replacing (4.9) in (4.5) gives the autocorrelation function of the process as

$$R(s) = \Delta I^2 \cdot \frac{\overline{\tau_1}}{\overline{\tau_0}+\overline{\tau_1}} \cdot \left\{ \frac{\overline{\tau_1}}{\overline{\tau_0}+\overline{\tau_1}} + \frac{\overline{\tau_0}}{\overline{\tau_0}+\overline{\tau_1}} \cdot \exp\left[-\left(\frac{1}{\overline{\tau_0}} + \frac{1}{\overline{\tau_1}} \right) \cdot s \right] \right\} . \tag{4.10}$$

Then solving (4.1) using (4.10) gives

$$S(f) = 4\int_0^\infty R(s) \cdot \cos(2\pi f s) ds = \frac{4\Delta I^2}{(\overline{\tau_0}+\overline{\tau_1}) \cdot \left[\left(\frac{1}{\overline{\tau_0}} + \frac{1}{\overline{\tau_1}} \right)^2 + (2\pi f)^2 \right]} \tag{4.11}$$

which gives the PSD of a telegraphic signal as a function of its average times spent on high and low states. In the context of trapping and de-trapping of charge carriers by defects, the average times spent on low and high states can be understood as the average time required to emit (τ_e) and capture (τ_c) a charge carrier, respectively.

Equation (4.11) can be rewritten in a more useful form by substituting

$$\beta = \frac{\tau_e}{\tau_c} \tag{4.12}$$

and

$$\frac{1}{\tau} = \frac{1}{\tau_c} + \frac{1}{\tau_e} , \tag{4.13}$$

resulting in

$$S(f) = 4\Delta I^2 \cdot \frac{\beta}{(1+\beta)^2} \cdot \frac{\tau}{1+(2\pi f \tau)^2} , \tag{4.14}$$

where β and τ are the ratio between emission and capture, and the characteristic time constant, respectively. From detailed balance (KIRTON; UREN, 1989),

$$\beta = \frac{\tau_e}{\tau_c} = g \cdot \exp\left(\frac{E_F - E_T}{kT} \right) , \tag{4.15}$$

where g, k, E_F and E_T are the degeneracy (approximately equal to one), Boltzmann constant in eV·K^{-1}, Fermi energy and trap energy, respectively

For the particular case in which $\overline{\tau_0} = \overline{\tau_1} = \overline{\tau_x}$, (4.14) can be simplified into

$$S(f) = 2\Delta I^2 \cdot \frac{\overline{\tau_x}}{4+(2\pi f \overline{\tau_x})^2} , \tag{4.16}$$

resulting in maximum total noise power. For this reason, experimentally identifiable telegraphic signals usually display $\tau_c \approx \tau_e$, which may be wrongly interpreted as a correlation between the two parameters that are, essentially, uncorrelated (GRASSER et al., 2009).

4.2 $1/f$ Noise Models

Historically, two main schools of thought have emerged to explain and model the $1/f$ behaviour of the power-spectral density. The first assumes the origin is related to the capture and emission of charge carriers by surface defects (traps) (MCWHORTER, 1957), and is commonly referred to as *number fluctuation theory*. The second attributes the $1/f$ to bulk mobility fluctuations (HOOGE, 1969; HOOGE; VANDAMME, 1978), and is commonly referred to as *mobility fluctuation theory*. A unified theory has been proposed (HUNG et al., 1990b; HUNG et al., 1990c; GHIBAUDO et al., 1991), incorporating mobility fluctuations due to Coulomb scattering to the number fluctuation model. This unified model is not, however, a combination of both models (SCHOLTEN et al., 2003), as the mobility fluctuations share the same origin as number fluctuations and are, thus, correlated.

While bulk mobility fluctuation models have been used to describe the $1/f$ noise bias dependence of PFETs (CHANG; ABIDI; VISWANATHAN, 1994; VANDAMME; HOOGE, 2008; HAARTMAN; ÖSTLING, 2007), number fluctuation models have been recently shown to explain the $1/f$ bias dependence of both P- and NFETs if a non-uniform distribution of traps in energy (VAN DER WEL et al., 2005; WIRTH; SILVA; KACZER, 2011) is assumed for p-type devices (BANASZESKI DA SILVA et al., 2014; BANASZESKI DA SILVA et al., 2016). Even in the context of trapping of charges, the trapping mechanism itself is not thoroughly understood. While studies on random telegraph signals and $1/f$ noise (DUTTA; HORN, 1981; SURYA; HSIANG, 1988; KIRTON; UREN, 1989) suggest a thermally activated process, compact $1/f$ noise models models, such as BSIM and PSP (HUNG et al., 1990b; HUNG et al., 1990c), still employ direct tunnelling (MCWHORTER, 1957), which is temperature independent.

In this section, number and mobility fluctuation models are presented. The correlated mobility model is also presented, as well as its compact version.

4.2.1 Number Fluctuation Model - McWhorter Model

Number fluctuation models assume that the primary mechanism responsible for the $1/f$ noise are the capture and emission of carriers by traps, which cause fluctuations to the surface potential of the device. As discussed in section 4.1, the activity of a single trap produces a Lorentzian power-spectrum. The work of Surdin (1939) proved that a $1/f$

spectrum could be obtained by the superposition of Lorentzian spectra with τ homogeneously distributed in log-scale, as shown in Figure 4.1.

Figure 4.1: Sum of uniformly-spaced (in log-scale) Lorentzians, resulting in an approximately $1/f$ spectrum.

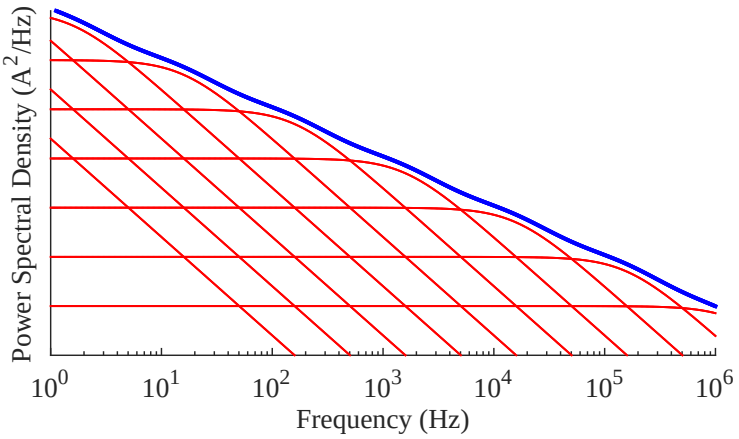

A physical model was proposed by McWhorter (1957) for a semiconductor with an oxide on the surface. This model, widely regarded as the McWhorter model, assumes that the uniformly distributed τ arise from direct tunnelling of charge carriers to traps located within the oxide, causing the current to fluctuate. Essentially, variations in trap occupancy result in carrier number fluctuations in the channel. The normalized drain current fluctuation can be written as

$$\frac{\partial I_D}{I_D} = \left[\frac{1}{\Delta N}\frac{\partial \Delta N}{\partial \Delta N_t}\right]\partial \Delta N_t \,, \tag{4.17}$$

where $\Delta N = NW\Delta x$ and $\Delta N_t = N_t W \Delta x$, being N and N_t the number of channel carriers and and occupied traps per unit area, respectively; W the transistor width and Δx a distance along the transistor length. The ratio $\partial \Delta N/\partial \Delta N_t = R$ is the coupling coefficient between the carrier number fluctuation in the channel and the trap occupancy. This ratio, R, is approximately 1 for strong inversion, but may assume smaller values for other regions of operation, being expressed by

$$R = \frac{C_i}{C_{ox} + C_i + C_d + C_{it}} \,, \tag{4.18}$$

where C_{ox}, C_i, C_d and C_{it} are the oxide, inversion layer, depletion, and interface trap capacitances per unit area. Substituting

$$C_i \approx \frac{q^2 N}{k_B T} \,, \tag{4.19}$$

equation (4.18) can be rewritten as

$$R = -\frac{N}{N+N^*} \,, \tag{4.20}$$

where

$$N^* = \frac{k_B T}{q^2} \cdot (C_{ox} + C_d + C_{it}) \,, \tag{4.21}$$

with typical N^* values being of the order of 10^{-10} cm^{-2} (HUNG et al., 1990b).

Consequently, the power spectral density of the local drain current fluctuation is given by

$$S_{\Delta I_D}(x,f) = \left(\frac{I_D}{W\Delta x}\right)^2 \cdot \left(\frac{R}{N}\right)^2 \cdot S_{\Delta N_t}(x,f) \,, \tag{4.22}$$

where $S_{\Delta N_t}(x,f)$ is the PSD of the mean-square fluctuations in the number of occupied traps in the area $W\Delta x$, and it is given by

$$S_{\Delta N_t}(x,f) = \int_{E_v}^{E_c} \int_0^W \int_0^{T_{ox}} 4N_{tr}(E,x,y,z)\Delta x f_t \cdot (1-f_t) \cdot \frac{\tau(E,x,y,z)}{1+\omega^2\tau(E,x,y,z)^2} dz dy dE \,, \tag{4.23}$$

where $N_{tr}(E,x,y,z)$ is the distribution of the traps in the oxide and over the energy, length, width, and depth; $\tau(E,x,y,z)$ is the trapping time constants; $\omega = 2\pi f$ is the angular frequency; T_{ox} is the oxide thickness; $E_c - E_v$ is the silicon band gap; and f_t is the trap occupancy function. This function, f_t, is given by

$$f_t = \left[1 + \exp\left(\frac{E - E_{Fn}}{kT}\right)\right]^{-1} \,, \tag{4.24}$$

where E_{Fn} is the electron quasi Fermi level.

In order to evaluate the integral in (4.23), the following suppositions are made: a) the distribution of the traps is uniform close to the interface, thus $N_{tr}(E,x,y,z) = N_{tr}(E)$; b) the probability of an electron penetrating into the oxide decreases exponentially with the distance from the interface; as a result, the trapping time constant is given by

$$\tau = \tau_o(E) \cdot \exp(\gamma z) \,, \tag{4.25}$$

where $\tau_o(E)$ is the time constant at the interface and γ is the wave function attenuation factor given by the WKB theory for carrier tunnelling in the Si-SiO_2 system (HUNG et al., 1990b). Notice that, while the McWhorter model traditionally employs direct tunnelling,

thermal activation, given by

$$\tau = \tau_o \cdot \exp\left(E_B/kT\right) \ , \tag{4.26}$$

where E_B is an activation energy, has been suggested by Surya and Hsiang (1988). The temperature dependence of the characteristic time constant is further explored in chapter 5 of this work.

Figure 4.2 illustrates the $f_t(1-f_t)$ term of equation (4.23), which behaves like a delta function around the quasi Fermi level. Thus, the main contribution for the integral is for traps close to the quasi Fermi level, hence one can approximate $N_{tr}(E) = N_{tr}(E_{Fn})$, removing $N_{tr}(E_{Fn})$ from the integral. The spread of the curve around the quasi Fermi level is related to the temperature of the system, as shown in figure 4.3. The area below the curve can be shown to increase with kT, meaning a larger number of traps are active at higher temperatures.

Figure 4.2: Behaviour of the $f_t(1-f_t)$ term for different electron quasi Fermi levels, E_{Fn}.

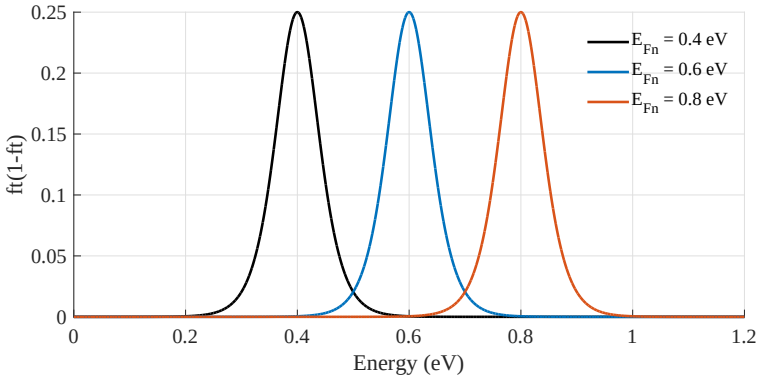

Figure 4.3: Behaviour of the $f_t(1-f_t)$ term as a function of trap energy for different temperatures and $E_F = 0.6$ eV.

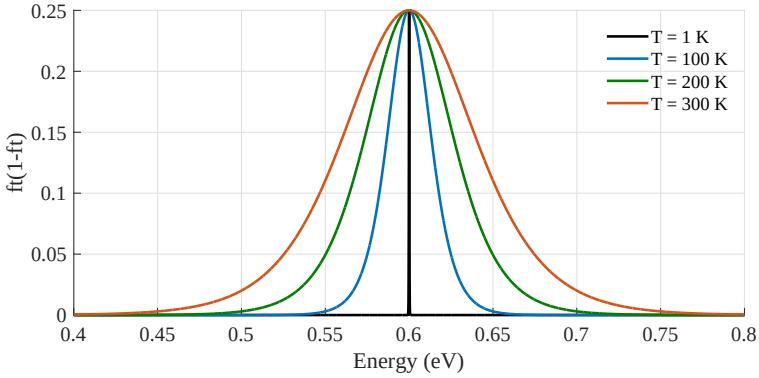

Thus, replacing $f_t(1-f_t) = -kT\frac{df_t}{dE}$ in equation (4.23) and solving the integration, results in

$$S_{\Delta N_t}(x,f) = N_{tr}(E_{Fn}) \cdot \frac{kTW\Delta x}{\gamma f}. \tag{4.27}$$

Hence, the total drain current noise power spectral density can be calculated using

$$S_{I_D} = \frac{1}{L^2} \int_0^L S_{\Delta I_D}(x, f) \cdot \Delta x dx \,, \tag{4.28}$$

where L is the channel length.

Finally, replacing (4.27) in (4.22) and then (4.22) in (4.28), results in

$$S_{I_D} = \frac{kT{I_D}^2}{\gamma f W L^2} \int_0^L N_{tr}(E_{Fn}) \cdot \left[\frac{R}{N(x)}\right]^2 dx \,, \tag{4.29}$$

which provides a description of the $1/f$ noise in terms of bias, temperature and geometry.

4.2.2 Mobility Fluctuation Model - Hooge Model

The work of Hooge (1969) demonstrated, based on $1/f$ noise measurements of homogeneous samples, that surfaces effects were not primarily responsible for the $1/f$ noise, indicating that the noise was essentially a bulk effect. This observation naturally contradicts the explanation given by McWhorter (1957), that attributes the $1/f$ to surface effects (traps).

The bulk mobility fluctuation model proposed by Hooge (1969), and Hooge and Vandamme (1978) is given by the empirical formula

$$S_{I_D}(f) = \frac{q\alpha_H I_D^2}{fWL^2} \int_0^L \frac{dx}{Q_i nv(x)} \tag{4.30}$$

where $\alpha_H$and $Q_i nv(x)$ are the Hooge parameter and inversion layer charge, respectively. These bulk mobility fluctuations were attributed to phonon scattering (HOOGE; VANDAMME, 1978). Since mobility in the channel depends not only on technology but also on the electric field, the Hooge parameter depends both on technology and bias conditions.

The works of Handel (1980) and Ngai (1980) attempted to explain the bulk mobility fluctuations through quantum beats between elastically scattered and weakly inelastically scattered carriers, respectively, being the distinct inelastic scattering mechanism the difference between both theories. These hypothesis, however, require unrealistic assumptions, as stated by Weissman (1988). The work of Jindal and van der Ziel (1981) proposed an explanation based on the fluctuation in the mean free path of the carriers; this

explanation is also insufficient according to Weissman (1988), as the characteristic times would be too short to produce low-frequency fluctuations.

For deeply-scaled devices (sub-$1\mu m^2$ area), the Lorentzian-like profiles of single traps become more prominent than the typical $1/f$ spectra, which indicates that trapping is, at least for small-area devices, the dominant noise mechanism. According to Vandamme and Hooge (2008), this is not evidence that the $1/f$ spectra of large-area devices is caused by the superposition of these Lorentzians, reinforcing the importance of bulk mobility fluctuations.

4.2.3 Correlated Fluctuations Model - Hung Model

The $1/f$ noise model implemented in the BSIM3, BSIM4 and PSP models was developed by Hung et al. (1990b) and Hung et al. (1990c). This model is considered an 'unified' model due to the fact that it accounts for both carrier number fluctuations and mobility fluctuations in the channel of the device. Notice that this unified model is not a combination of both models, as pointed out by Scholten et al. (2003). The mobility fluctuations are a consequence of the Coulombic scattering due to trap occupation. Therefore, these mobilities fluctuations are not a bulk effect, rather sharing the same surface origin as number fluctuations. Hence, these fluctuations are correlated.

The derivation of the model, is similar to that of the McWhorter model. Variations in trap occupancy, however, result not only in fluctuations in carrier number, but also in correlated fluctuations in carrier mobility in the channel (HUNG et al., 1990b). The normalized drain current fluctuation is similar to that of (4.17), but has an added mobility factor, and is given by

$$\frac{\partial I_D}{I_D} = -\left[\frac{1}{\Delta N}\frac{\partial \Delta N}{\partial \Delta N_t} \pm \frac{1}{\mu}\frac{\partial \mu}{\partial \Delta N_t}\right]\partial \Delta N_t \, . \tag{4.31}$$

The signal ahead of the mobility term in equation (4.31) is chosen according to the trap charge (if the trap is neutral or charged when occupied). The ratio $\partial\mu/\partial\Delta N_t$ is the coupling coefficient between the carrier mobility fluctuation and the trap occupancy. According to Hung et al. (1990b), it can be demonstrated, through Mathiessen rule, that

$$\frac{\partial \mu}{\partial N_t} = \frac{\alpha \mu^2}{W \Delta x}, \tag{4.32}$$

where α is the scattering coefficient.

Given that the relation $\partial\Delta N/\partial\Delta N_t = R$ from the McWhorter model is still valid, then (4.31) can be rewritten as

$$\frac{\partial I_D}{I_D} = -\left(\frac{R}{N} \pm \alpha\mu\right) \cdot \frac{\partial \Delta N_t}{W\Delta x}. \tag{4.33}$$

Consequently, the power spectral density of the local drain current fluctuation is given by

$$S_{\Delta I_D}(x,f) = \left(\frac{I_D}{W\Delta x}\right)^2 \cdot \left(\frac{R}{N} \pm \alpha\mu\right)^2 \cdot S_{\Delta N_t}(x,f) \tag{4.34}$$

where $S_{\Delta N_t}(x,f)$ is the PSD of the mean-square fluctuations in the number of occupied traps in the area $W\Delta x$, given by (4.23).

Following the same steps of the McWhorter model derivation — including the assumption that direct tunnelling is responsible for the distribution of characteristic time constants —, the $1/f$ noise PSD is found to be

$$S_{I_D} = \frac{kT{I_D}^2}{\gamma f W L^2} \int_0^L N_{tr}(E_{Fn}) \cdot \left[\frac{R}{N(x)} \pm \alpha\mu\right]^2 dx. \tag{4.35}$$

From (4.35), the works of Hung et al. (1990b), Hung et al. (1990c) derived a compact model that has been widely employed in MOSFET models, such as BSIM and PSP. Substituting $dx = -dV/E$ and obtaining E from the drain current equation

$$I_D = W\mu qNE_x \tag{4.36}$$

results in

$$S_{I_D} = \frac{kTqI_D\mu}{\gamma f L^2} \int_0^{V_D} N_{tr}(E_{Fn}) \cdot \left(1 \pm \alpha\mu N R^{-1}\right)^2 \cdot \frac{R^2}{N} dV. \tag{4.37}$$

In order to solve (4.37) the bias dependence of parameters α, μ and $N_t(E_{Fn})$ is required. Since α and μ are a function of the carrier concentration, N, which, in turn, is a function of the carrier quasi Fermi level, (4.37) can be rewritten as

$$S_{I_D} = \frac{kTqI_D\mu}{\lambda f L^2} \int_0^{V_D} N^*_{tr}(E_{Fn}) \cdot \frac{R^2}{N} dV \tag{4.38}$$

where

$$N^*_{tr} = N_t(E_{Fn}) \cdot (1 \pm \alpha\mu N R^{-1})^2. \tag{4.39}$$

In this form, $N^*_{tr}(E_{Fn})$ is the apparent oxide trap density that produces the same

noise power as if there were no contribution from the mobility fluctuation (HUNG et al., 1990b). The model proposed by Hung et al. (1990b) provides an empirical parametric function which is sufficiently simple to provide an analytical expression for S_{I_D}, but robust enough to be applicable for MOSFETs fabricated by different technological processes. The proposed model, equation (4.40), has three parameters — *NOIA*, *NOIB* and *NOIC* — and is a function of the carrier concentration, N.

$$N_{tr}^{*} = NOIA + NOIB \cdot N + NOIC \cdot N^2 \tag{4.40}$$

Parameters *NOIA*, *NOIB* and *NOIC* are technology-dependent parameters. Assuming that the trap density, N_t, is independent of energy, then

$$NOIA = N_t \tag{4.41}$$

$$NOIB = \pm 2\alpha\mu_{eff}R^{-1}N_t \tag{4.42}$$

$$NOIC = (\alpha\mu_{eff}R^{-1})^2 N_t. \tag{4.43}$$

Substituting (4.40) in (4.38) an analytical expression can be derived for the $1/f$ noise PSD for different device operating regions, as presented by Hung et al. (1990b). In strong inversion, the $1/f$ noise PSD is given by

$$\begin{aligned} S_{I_D,inv}(f) = & \frac{kTq^2\mu I_D}{a\lambda f L^2 C_{ox}} \cdot [NOIA \cdot log(\frac{N_0 + N^*}{N_l + N^*}) + NOIB \cdot (N_0 - N_l) + \frac{NOIC}{2}({N_0}^2 - {N_l}^2)] \\ & + \Delta L \frac{kT{I_D}^2}{\lambda f W L^2} \cdot [\frac{NOIA + NOIB \cdot N_l + NOIC \cdot {N_l}^2}{(N_l + N^*)^2}], \end{aligned} \tag{4.44}$$

where

$$N_0 = N(0) = \frac{C_{ox}}{q} \cdot (V_{GS} - V_{th0}) \, , \tag{4.45}$$

$$N_l = N(L) = \frac{C_{ox}}{q} \cdot (V_{GS} - V_{th0} - aV_{DS}), \tag{4.46}$$

being a, V_{th0}, V_{DS} and V_{GS} a bulk charge effect modelling parameter, threshold voltage of the long channel device at zero substrate bias, gate-to-source voltage, and drain-to-source voltage (in the case of saturation, the saturation voltage, $V_{DS_{sat}}$), respectively (DUNGA et

al., 2006). For subthreshold region, $S_{I_D}(f)$ is given by

$$S_{I_D,subVt}(f) = \frac{NOIA \cdot kT{I_D}^2}{WL\lambda fN^{*2}.}. \tag{4.47}$$

The parameters of equations (4.44) and (4.47) are presented in Table 4.1.

Table 4.1: BSIM4 Noise Simulation Parameters

Symbol	Definition
k	Boltzmann Constant
T	Temperature
q	Elementary Charge
μ	Effective Carrier Mobility
I_D	Drain Current
C_{ox}	Oxide Capacitance
L	Effective Channel Length
W	Effective Channel Width
a	Bulk charge effect modelling parameter
γ	Attenuation coefficient given by WKB theory
$NOIA$	Noise modelling parameter A
$NOIB$	Noise modelling parameter B
$NOIC$	Noise modelling parameter C
N_0	Carrier density at source terminal
N_l	Carrier density at drain terminal
ΔL	Channel length modulation parameter

The 1/f noise PSD at any operating point is then given by

$$S_{I_D}(f) = \frac{S_{I_D,inv}(f) \cdot S_{I_D,subVt}(f)}{S_{I_D,inv(f)} + S_{I_D,subVt}(f)}\ . \tag{4.48}$$

Despite its popularity, the correlated fluctuations model has been criticized by Vandamme and Hooge (2008), arguing that the correlated mobility parameters is but a mere curve fitting parameter, with unrealistic values.

4.2.4 RTS-Based Statistical Model

RTS-based models are fundamentally similar to number fluctuation models, as capture and emission of carriers by traps is also assumed, and the LFN PSD is a result

of the summation of Lorentzians. In opposition to the McWhorter model, however, these models attribute statistical distribution to specific noise parameters — such as number of traps in a device and individual trap impact —, which allow the estimation of the noise variability, for instance. Among the models that propose a RTS-based LFN are the works of Wirth et al. (2005); Wirth, da Silva and Brederlow (2007); da Silva, Wirth and Brusamarello (2008); Banaszeski da Silva et al. (2014); Banaszeski da Silva et al. (2016).

The model proposed by Banaszeski da Silva et al. (2014) provides an analytical expression for the noise variance. The following assumptions are taken for the derivation of the model:

(i) the total number of traps in a device (N) is a Poisson distributed random variable;
(ii) τ is a log-uniformly distributed random variable;
(iii) $\beta/(1+\beta)^2$ and $\beta^2/(1+\beta)^4$ are approximated by delta functions multiplied by kT and $kT/6$, respectively;
(iv) ΔI_D, N and τ are independent.

4.2.4.1 Expected Value

The work of Banaszeski da Silva et al. (2014) demonstrated that, from the RTS framework, the expected value of the LFN in MOS devices is given by

$$\mathrm{E}\left[S_{I_D}(f)\right] = \frac{kTI_D^2}{WL^2 f} \int_0^L \mathrm{E}\left[\widetilde{\Delta I_D}^2 | \mathrm{X}_{tr} = x\right] \cdot \frac{N_{tr}(E_{Fn})}{\gamma'} dx \,, \tag{4.49}$$

where the trap position along the channel, $\mathrm{X}_t r$, is assumed to be a uniformly distributed random variable; $\widetilde{\Delta I_D}$ is the normalized current deviation, given by

$$\widetilde{\Delta I_D} = \frac{WL\Delta I_D}{I_D} \,; \tag{4.50}$$

and $N_{tr}(E_{Fn})/\gamma$ gives the trap density in the area, energy and in the log-domain of time constants ($\mathrm{cm}^{-2}\mathrm{eV}^{-1}$ per neper). It is important to notice that γ' in the model is the parameter of the log-uniform distribution of time constants.

For the particular case in which the channel is uniformly charged, if the drain current fluctuations are assumed to be exponentially distributed, (4.49) can be simplified to

$$\mathrm{E}\left[S_{I_D}(f)\right] = 2\frac{kTI_D^2}{WLf} \cdot \frac{N_{tr}(E_{Fn})}{\gamma'} \cdot \mathrm{E}\left[\widetilde{\Delta I_D}\right]^2 \,. \tag{4.51}$$

Incorporating number fluctuation and correlated mobility fluctuations, the average drain current fluctuation, $\mathrm{E}\left[\Delta\widetilde{I_D}\right]$, is given by

$$\mathrm{E}\left[\Delta\widetilde{I_D}\right] = \left(\frac{R}{N} + \alpha\mu\right) , \tag{4.52}$$

and R is given by (4.20).

4.2.4.2 Variance

Similarly to the expected value, the variance of the LFN PSD can be derived from the RTS-based framework, as shown by Banaszeski da Silva et al. (2014). The variance is given by

$$\mathrm{Var}\left[S_{I_D}(f)\right] = \frac{kTI_D^4}{3\pi^2 f^2 W^3 L^4} \int_0^L \mathrm{E}\left[\Delta\widetilde{I_D}^4 | \mathrm{X}_T = x\right] \cdot \frac{N_{tr}(E_{Fn})}{\gamma'} dx \, . \tag{4.53}$$

For the particular case in which the channel is uniformly charged, if the drain current fluctuations are assumed to be exponentially distributed, and carrier number fluctuations and correlated mobility fluctuations are considered, (4.53) can be simplified to

$$\mathrm{Var}\left[S_{I_D}(f)\right] = 24\frac{kTI_D^4}{3\pi^2 f^2 W^3 L^3} \cdot \frac{N_{tr}(E_{Fn})}{\gamma'} \cdot \left(\frac{R}{N} + \alpha\mu\right)^4 . \tag{4.54}$$

The aforementioned work has also shown that it is possible to relate the expected value and variance of the LFN PSD to the standard deviation of $\ln(S_{I_D})$ using

$$\sigma\left[\ln(S_{I_D})\right] = \sqrt{\ln\left(1 + \frac{\mathrm{Var}\left[S_{I_D}\right]}{\mathrm{E}\left[S_{I_D}\right]^2}\right)} , \tag{4.55}$$

which can be rewritten as

$$\sigma\left[\ln(S_{I_D})\right] = \sqrt{\ln\left(1 + \frac{K}{WL}\right)} , \tag{4.56}$$

for $K = WL \cdot \mathrm{Var}\left[S_{I_D}\right] / \mathrm{E}\left[S_{I_D}\right]^2$. For the uniformly inverted channel condition, the K parameter is easily obtained analytically through

$$K = \frac{2}{\pi^2 kT} \cdot \frac{\gamma'}{N_{tr}(E_{Fn})} \, . \tag{4.57}$$

Notice that K is geometry independent and, thus, is a technology parameter, suitable for comparing noise variability in different technology nodes.

4.2.4.3 Correlation Coefficient

For upcoming analyses presented in this work, the correlation coefficient between two LFN PSD populations is pivotal. Thus, it is necessary estimate the correlation coefficient using the same RTS-based framework employed for the expected value and variance expressions. The Pearson product-moment correlation coefficient, R, of two random variables, X and Y, is given by the covariance of the two variables divided by the square root of the product of their variance, so that

$$\mathrm{R}\left[\mathrm{X},\mathrm{Y}\right] = \frac{\mathrm{Cov}\left[\mathrm{X},\mathrm{Y}\right]}{\sqrt{\mathrm{Var}[\mathrm{X}]\cdot\mathrm{Var}[\mathrm{Y}]}}\ , \tag{4.58}$$

where **Cov** is the covariance operator. In the context of this work, X and Y are the PSDs of the LFN and are treated as stochastic processes in respect to a given system variable – such as frequency, temperature and biasing. Since the same stochastic process is been compared to itself under different conditions, these analyses are called *autocorrelation analyses*.

From the RTS-based framework presented in section 4.1, the LFN PSD of a MOSFET is given by the sum of the contribution of individual traps, thus

$$\mathrm{E}\left[S_{I_D}\right] = \mathrm{E}\left[\sum_{i=1}^{\mathrm{N}} L_{x,i}\right]\ , \tag{4.59}$$

in which N and $L_{x,i}(f)$ are the number of traps in the device (which, itself is a random variable) and the Lorentzian PSD of the individual trap i at a given condition x, respectively.

Using the Law of Total Variance gives

$$\mathrm{Var}\left[\sum_{i=1}^{\mathrm{N}} L_{x,i}\right] = \mathrm{E}\left[\mathrm{Var}\left[\sum_{i=1}^{\mathrm{N}} L_{x,i}\middle|\mathrm{N}\right]\right] + \mathrm{Var}\left[\mathrm{E}\left[\sum_{i=1}^{\mathrm{N}} L_{x,i}\middle|\mathrm{N}\right]\right]\ . \tag{4.60}$$

For N and $L_{x,i}$ independent yields

$$\mathrm{E}\left[\mathrm{Var}\left[\sum_{i=1}^{\mathrm{N}} L_{x,i}\middle|\mathrm{N}\right]\right] = \mathrm{E}\left[\mathrm{N}\right]\cdot\mathrm{Var}\left[L_x\right] \tag{4.61}$$

and

$$\mathrm{Var}\left[\mathrm{E}\left[\sum_{i=1}^{\mathrm{N}} L_{x,i}\middle|\mathrm{N}\right]\right] = \mathrm{Var}\left[\mathrm{N}\right]\cdot\mathrm{E}\left[L_x\right]^2 \ . \tag{4.62}$$

Assuming that N is Poisson distributed and, thus

$$\mathrm{E}[\mathrm{N}] = \mathrm{Var}[\mathrm{N}] \ , \tag{4.63}$$

and writing the variance as

$$\mathrm{Var}\left[\mathrm{X}\right] = \mathrm{E}\left[\mathrm{X}^2\right] - \mathrm{E}\left[\mathrm{X}\right]^2 \ , \tag{4.64}$$

it is possible to simplify (4.60) to

$$\mathrm{Var}\left[\sum_{i=1}^{\mathrm{N}} L_{x,i}\right] = \mathrm{E}\left[\mathrm{N}\right]\cdot\mathrm{E}\left[L_x^2\right] \ . \tag{4.65}$$

Similarly, using the Law of Total Covariance

$$\begin{aligned}&\mathrm{Cov}\left[\sum_{i=1}^{\mathrm{N}} L_{x,i}, \sum_{i=1}^{\mathrm{N}} L_{y,i}\right] \\ &\quad = \mathrm{E}\left[\mathrm{Cov}\left[\sum_{i=1}^{\mathrm{N}} L_{x,i}, \sum_{i=1}^{\mathrm{N}} L_{y,i}\middle|\mathrm{N}\right]\right] + \mathrm{Cov}\left[\mathrm{E}\left[\sum_{i=1}^{\mathrm{N}} L_{x,i}\middle|\mathrm{N}\right], \mathrm{E}\left[\sum_{i=1}^{\mathrm{N}} L_{y,i}\middle|\mathrm{N}\right]\right] \ .\end{aligned} \tag{4.66}$$

For N independent of $L_{i,x}$ and $L_{i,y}$, (4.66) reduces to

$$\mathrm{Cov}\left[\sum_{i=1}^{\mathrm{N}} L_{x,i}, \sum_{i=1}^{\mathrm{N}} L_{y,i}\right] = \mathrm{E}[\mathrm{N}]\cdot\mathrm{Cov}\left[L_x, L_y\right] + \mathrm{Cov}\left[\mathrm{N},\mathrm{N}\right]\cdot\mathrm{E}\left[L_x\right]\cdot\mathrm{E}\left[L_y\right] \ . \tag{4.67}$$

Naturally, $\mathrm{Cov}[\mathrm{N},\mathrm{N}] = \mathrm{Var}\left[\mathrm{N}\right]$. If N is again assumed to be Poisson distributed, then (4.67) can be further simplified to

$$\mathrm{Cov}\left[\sum_{i=1}^{\mathrm{N}} L_{x,i}, \sum_{i=1}^{\mathrm{N}} L_{y,i}\right] = \mathrm{E}[\mathrm{N}]\cdot\left(\mathrm{Cov}\left[L_x, L_y\right] + \mathrm{E}\left[L_x\right]\cdot\mathrm{E}\left[L_y\right]\right) \ . \tag{4.68}$$

Finally, using the definition of covariance

$$\mathrm{Cov}\left[\mathrm{X},\mathrm{Y}\right] = \mathrm{E}\left[\mathrm{X}\cdot\mathrm{Y}\right] - \mathrm{E}\left[\mathrm{X}\right]\cdot\mathrm{E}\left[\mathrm{Y}\right] \tag{4.69}$$

simplifies (4.68) to

$$\mathrm{Cov}\left[\sum_{i=1}^{\mathrm{N}} L_{x,i}, \sum_{i=1}^{\mathrm{N}} L_{y,i}\right] = \mathrm{E}\left[\mathrm{N}\right] \cdot \mathrm{E}\left[L_x \cdot L_y\right] \ . \tag{4.70}$$

Substituting (4.65) and (4.70) into (4.58) results in

$$\mathrm{R}\left[S_{I_D,x}, S_{I_D,y}\right] = \frac{\mathrm{E}\left[L_x \cdot L_y\right]}{\sqrt{\mathrm{E}\left[L_x^2\right] \cdot \mathrm{E}\left[L_y^2\right]}} \ . \tag{4.71}$$

Equation (4.71) will be used in Chapter 7 of this work to analytically and numerically calculate the correlation coefficient between two LFN PSD populations under different conditions using the RTS framework. These predictions can be compared to measured data in order to verify whether the models properly describe the behaviour of the fundamental noise sources.

4.3 Summary and Discussion

Random telegraph noise and $1/f$ noise are the primary contributors to CMOS LFN power. While bulk-mobility fluctuation models (more prominently the Hooge model) support that RTS and $1/f$ noise have distinguished origins, number fluctuation models (including the correlated mobility fluctuations) not only attribute both RTS and $1/f$ noise to the trapping and de-trapping of charge carrier, but also support the view that they are, essentially, the same process.

Vandamme and Hooge (2008) questioned this unified view, stating that "*the typical bumpy spectra in small MOSTs do not represent a conclusive proof that the* $1/f$ *noise in large devices result from the superposition of many elementary RTS fluctuations*." Using the methodology proposed in this work, it is demonstrated in section 7.2 that there is strong evidence to support the claim that $1/f$ noise in large-area MOS transistors is indeed a product of RTS fluctuations, even if no bumps are visible in the spectrum.

In the context of charge trapping, the assumption that the characteristic time constant of traps is governed by direct tunnelling has been employed not only in noise models (MCWHORTER, 1957; HUNG et al., 1990b; HUNG et al., 1990c), but also in works where the position of the trap within the oxide is extracted, such as Lukyanchikova et al. (2009) and Ding, Misra and Srinivasan (2016), despite observations of a thermally activated process being reported in several works, such as Surya and Hsiang (1988), Kirton

and Uren (1989), Xiong et al. (2002) and Wei, Xiong and Zhou (2009).

Notice that in section 7.3, the methodology proposed in this work is applied to experimental data and the results support the view direct tunnelling is not sufficient to describe the behaviour of the LFN with the temperature; a thermally activated model, in the likes of that proposed by Dutta and Horn (1981); Surya and Hsiang (1988); and Kirton and Uren (1989), is required to fully explain the observed LFN behaviour. Consequently, it should be accounted for in the aforementioned LFN models.

The following chapter addresses this important discussion on the temperature dependence of MOSFET LFN.

5 LOW-FREQUENCY NOISE TEMPERATURE DEPENDENCE

The temperature dependence of the 1/f noise has been an important aspect for the modelling of $1/f$ noise and the understanding of its dynamics. Among the first studies of the $1/f$ noise in semiconductor devices is the work by McWhorter (1957), which observed a weak dependence of the $1/f$ noise magnitude on temperature. This behaviour led to proposition of a noise model based on electron tunnelling, which is inherently a temperature independent process, stating that the time constant distribution is related to the spatial distribution of traps depth-wise. Recent works, however, have shown modern oxides are simply too thin to support the elastic tunnelling model (CAMPBELL et al., 2009) and capture and emission times are uncorrelated to the trap distance from the interface (NAGUMO et al., 2010).

In contradiction to the model proposed by McWhorter (1957), the work of Surya and Hsiang (1988) observed that the $1/f$ noise of commercial p-channel MOSFETs varied significantly, not only in magnitude, but also in form, when operated from 60 K up to 290 K. Based on these experimental results, Surya and Hsiang (1988) proposed a different approach to the calculation of the times constants, based on the thermal activated model for $1/f$ noise in semiconductors by Dutta and Horn (1981)[1].

Figure 5.1a displays experimental data for the noise PSD at 200 Hz as a function of the absolute temperature. The result indicates that the magnitude of the $1/f$ noise PSD is, in fact, temperature dependent. Additionally, Figure 5.1b displays extracted frequency exponent, γ, of the $1/f$ noise spectrum at 200 Hz as a function of temperature, indicating that the shape of noise spectrum is strongly dependent on the temperature and that this relation is non-linear.

Figure 5.1: a) Noise PSD and b) measured frequency exponent as a function of temperature for a p-channel device in linear region.

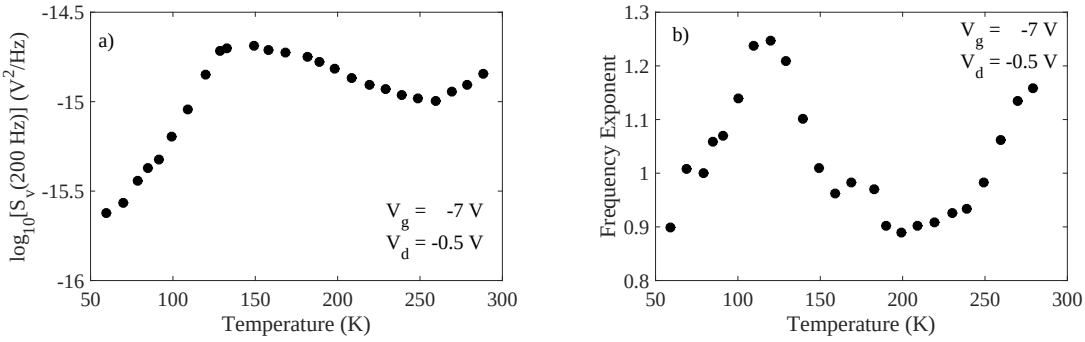

Source: Adapted from Surya and Hsiang (1988)

[1] If the reader is not familiarised with the Dutta and Horn identity, please refer to section 5.1 of this work.

According to Surya and Hsiang (1988), the simplistic spatial distribution of traps is insufficient to fully account for the temperature dependence of the noise magnitude, thus questioning the validity of the elastic tunnelling model. Conversely, the work claims that using the thermal activation model it is possible to account for both the magnitude and the functional form of the $1/f$ noise PSD.

The work of Wong and Cheng (1990) delves further into the temperature dependence of the $1/f$ noise by analysing n-channel MOS devices with different gate insulators. Figure 5.2 displays the frequency exponent as a function of the temperature for different devices. According to their work, there is a correlation of the peak locations in the plots and the major trapping centres in the Si-SiO_2 interface.

Figure 5.2: Frequency exponent as a function of absolute temperature for n-channel devices with different insulators.

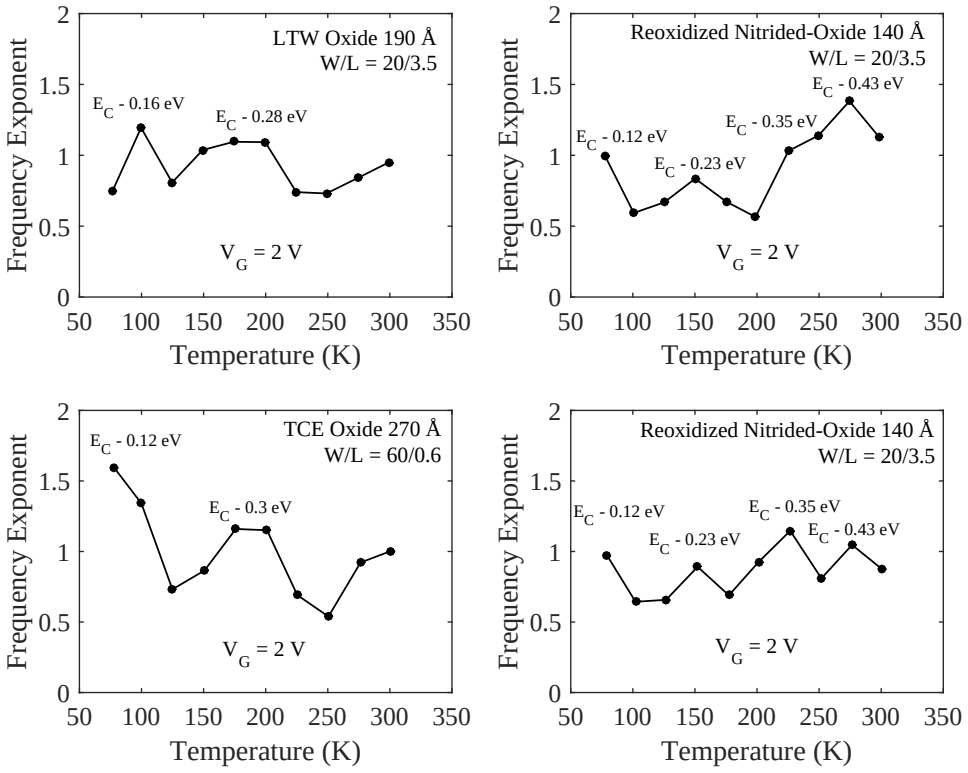

Source: Adapted from Wong and Cheng (1990).

A comparison between commercially available CMOS transistors from subthreshold to strong inversion was performed by Chang, Abidi and Viswanathan (1994). For NFETs in strong inversion, no significant magnitude variation was observed in the input-referred noise spectrum at different temperatures, and only a slope change was verified, as shown in Figure 5.3a. These results, associated to the weak bias dependence observed, gave credence to the tunnelling model proposed by McWhorter (1957).

The PFETs, on the other hand, showed strong bias dependence on the input-referred noise spectra at all temperatures. Figure 5.3b displays the input referred noise for the p-channel device in strong inversion for different temperatures; a significant $1/f$ noise spectra variation with temperature can be observed, in contrast to that of the NFET. According to Chang, Abidi and Viswanathan (1994), the behaviour of the p-channel transistor can be modelled using mobility fluctuations. Therefore, it concludes that noise in the n-channel device is more conveniently modelled using a number fluctuation model, whereas the p-channel device is more conveniently modelled using a bulk mobility fluctuation model.

Figure 5.3: Noise PSD for a) p-channel transistor and b) n-channel transistor at different temperatures in the linear region of operation.

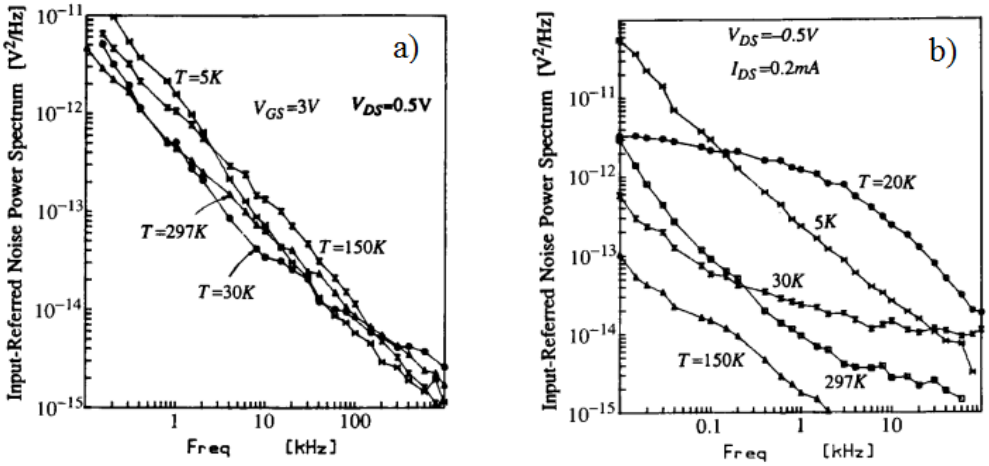

Source: Adapted from Chang, Abidi and Viswanathan (1994)

A study regarding the impact of total ionizing dose (TID) on the $1/f$ noise spectra of NFETs at different temperatures was performed by Xiong et al. (2002). The noise magnitude variation with temperature of an NFET device before and after irradiation, and after annealing, are shown in figure 5.4a. Their findings reinforce the idea that the $1/f$ noise in n-channel devices is a thermally activated process, in accordance to Surya and Hsiang (1988), agreeing that the relation presented by Dutta and Horn (1981) provides a very reasonable quantitative description of the noise, as shown in figure 5.4b. The success of the Dutta and Horn relation in describing the correlated temperatures and frequency dependence of the noise allows the energy distribution of the defect responsible for the noise to be estimated from noise measurements as a function of temperature (XIONG et al., 2002).

Figure 5.4: a) Noise PSD of an NFET at 1 Hz as a function of temperature prior and after irradiation. b) Measured and calculated frequency exponent for the pre-irradiated condition.

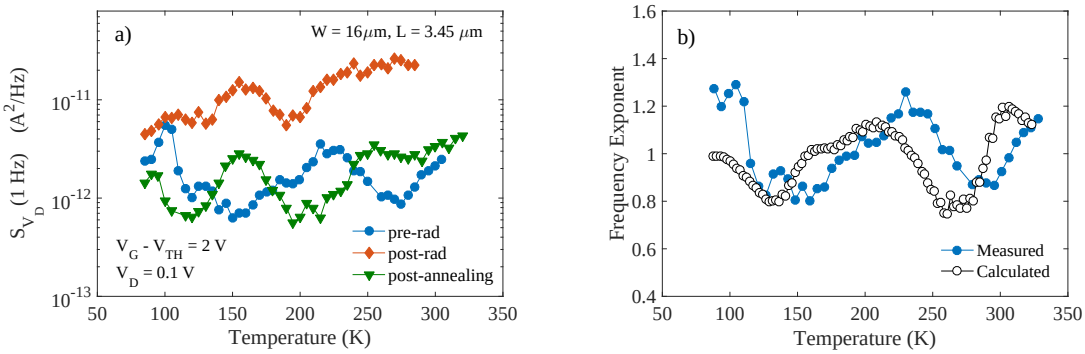

Source: Adapted from Xiong et al. (2002)

Lee et al. (2006) studied the $1/f$ noise in sub-100 nm MOSFETs. Figure 5.5 shows the $1/f$ noise PSD for NFETs and PFETs at different temperatures. For the p-channel device, a small noise magnitude reduction from 27 ºC to 70 ºC is observed, but little variation is observed from 70 ºC to 150 ºC. For the n-channel device, the result is similar to the one presented in figure 5.3, as there is little noise power variation with temperature. Here, however, the Lorentzian-like lumps are clearly visible in the n-channel $1/f$ noise spectra due to the small device area (W=150 nm and L=50 nm). Interestingly, the lumps of the Lorentzian curves seem to shift with temperature, giving a complex relation with temperature. Also, due to these shifts, the frequency exponent varies significantly with temperature.

Figure 5.5: $1/f$ noise spectra of N- and PFETs at different temperatures.

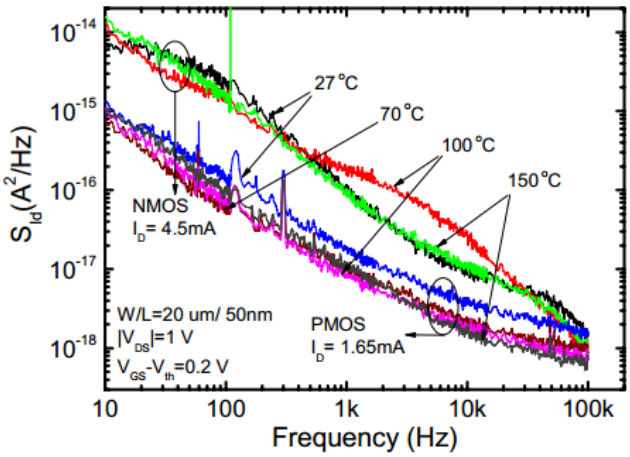

Source: Lee et al. (2006)

Regarding the temperature dependence of the $1/f$ noise in FINFETs, the work of Wei, Xiong and Zhou (2009) provided experimental data on the issue, concluding that the noise characteristics of FINFETs are comparable to their bulk-CMOS counterparts.

Figure 5.6 displays the temperature dependence of the $1/f$ noise of two FINFETs, *device 1* and *device 2*, in the linear region of operation.

Figure 5.6: Measured drain-voltage noise spectral density at 10 Hz versus temperature for two FINFETs in linear region of operation.

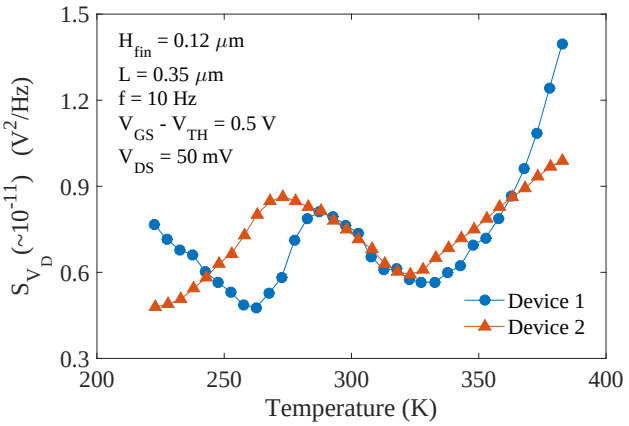

Source: Adapted from Wei, Xiong and Zhou (2009)

Their results indicate that for the thermal activation model is more convincing for FINFETs than the elastic tunnelling model. Figure 5.7 displays the measured and calculated frequency exponent using the Dutta and Horn relation, presented in equation (5.10) of the following section.

Figure 5.7: Frequency exponent as a function of temperature at 10 Hz for a) device 1 and b) device 2.

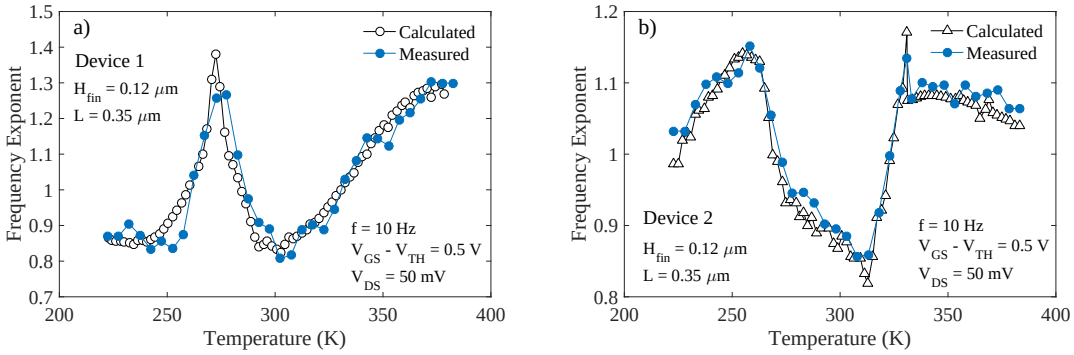

Source: Adapted from Wei, Xiong and Zhou (2009)

In the context of AlGaN/GaN HEMTs (high-electron-mobility transistors), Wang et al. (2017) demonstrated that, while bulk-mobility fluctuations are commonly applied to analyse $1/f$ noise in such devices, they do not properly describe the temperature, bias and frequency dependence of the noise. In addition, it was also reported that there is close agreement between experimental data and the Dutta-Horn model. The findings reinforce that the noise is well-described by number fluctuations and that the capture and emission process is thermally activated.

5.1 The Dutta-Horn Identity

The work of Dutta and Horn (1981) provides an important relation between the slope of the PSD spectrum (derivative of the noise spectrum in terms of frequency) and the derivative of the noise spectrum in terms of temperature. If the Dutta-Horn identity is satisfied, it is a strong indication that underlying mechanisms of trapping and de-trapping of carriers is thermally activated (DUTTA; HORN, 1981; SURYA; HSIANG, 1988; WEI; XIONG; ZHOU, 2009).

From Chapter 4, equation (4.23), if number fluctuations are assumed as the primary responsible for the $1/f$ noise in MOS devices, then the noise PSD follows

$$S_{I_D}(\omega,T) \propto \int_{-\infty}^{\infty} \frac{\tau(E,x,y,z)}{1+\omega^2\tau(E,x,y,z)^2} \cdot f_\tau d\tau \ . \tag{5.1}$$

If thermal activation and position independence is assumed for τ, then (5.1) can be rewritten as

$$S_{I_D}(\omega,T) \propto \int_{-\infty}^{\infty} \frac{\tau_o \cdot e^{E_B/kT}}{1+(\omega\tau_o \cdot e^{E_B/kT})^2} \cdot D(E_B) dE_B \ , \tag{5.2}$$

where $D(E_B)$ is the probability density function of the activation energies distribution. If $D(E_B)$ is constant within the window of interest, i.e. the activation energies are uniformly distributed, then $S(\omega,T)$ follows a $1/\omega$ behaviour. If $D(E_B)$ is not constant, however, the solution is not simple, though a solution is possible after expanding $D(E_B)$ in a Taylor series (DUTTA; HORN, 1981). When $D(E_B)$ varies slowly over the range of $\Delta E_B \approx kT$ then (5.2) reduces to

$$S_{I_D}(\omega,T) \propto \frac{kT}{\omega} \cdot D(\overline{E_B}) \ , \tag{5.3}$$

where $\overline{E_B}$ is the activation energy at which the function

$$h(\omega,T) = \frac{\tau_o \cdot e^{E_B/kT}}{1+(\omega\tau_o \cdot e^{E_B/kT})^2} \tag{5.4}$$

peaks. This energy can be obtained by calculating the maximum of (5.4) through

$$\frac{\partial h}{\partial E_B} = 0 \ , \tag{5.5}$$

resulting in

$$\overline{E_B} = -kT \cdot \ln(\omega\tau_o) \ . \tag{5.6}$$

Rewriting (5.3) as

$$D(\overline{E_B}) \propto \frac{\omega}{kT} \cdot S_{I_D}(\omega, T) \ , \tag{5.7}$$

it becomes clear that if ω and T are varied in order to keep $\overline{E_B}$ unchanged in (5.6), then $(\omega/kT) \cdot S_{I_D}$ must also remain unchanged, since $D(\overline{E_B})$ is constant. The conclusion is that there must be a ratio $\Delta\omega/\Delta T$ that satisfy

$$\left(\Delta\omega \cdot \frac{\partial}{\partial \omega} + \Delta T \frac{\partial}{\partial T} \right) \cdot [-kT \cdot \ln(\omega\tau_o)] = 0 \tag{5.8}$$

and

$$\left(\Delta\omega \cdot \frac{\partial}{\partial \omega} + \Delta T \frac{\partial}{\partial T} \right) \cdot \left[\frac{\omega}{kT} \cdot S_{I_D}(\omega, T) \right] = 0 \ . \tag{5.9}$$

Equations (5.8) and (5.9) essentially translate the previous ideas into their mathematical form. There should be a combination of $\Delta\omega$ and ΔT values that cause $\overline{E_B}$ to remain constant and, consequently, also $D(\overline{E_B})$. Solving these equations results in the Dutta and Horn identity, given by

$$\frac{\partial \ln [S_{I_D}(\omega, T)]}{\partial \ln(\omega)} = \frac{1}{\ln(\omega\tau_o)} \cdot \left[\frac{\partial S_{I_D}(\omega, T)}{\partial \ln(T)} - 1 \right] \ . \tag{5.10}$$

Though the relation may seem surprising at first, relating the slope of the noise PSD (i.e. the derivative of the noise in terms of frequency) to the derivative of the noise PSD in terms of temperature, one should keep in mind that the characteristic time constant of the traps is exponentially dependent on temperature when thermal activation is assumed. Therefore, temperature increments cause the characteristic time constants to decrease, shifting the noise PSD towards higher frequencies. It is important to notice that the sum of finite individual traps do not produce perfect 1/f noise and, thus, small bumps are always present in the noise PSD. This means that increasing the temperature, these bumps "slide" towards higher frequencies.

The Dutta-Horn identity thus assumes that, at different temperatures, the shape of the PSD is preserved but shifted in frequency, so that the same slope of the PSD is found at different frequencies for different temperatures. This idea will be further explored in upcoming chapters of this work.

This relation has been used in a multitude of works (SURYA; HSIANG, 1988; XIONG et al., 2002; WEI; XIONG; ZHOU, 2009) to provide strong evidence that the $1/f$ noise originates from a thermally activated process. The drawback of this method is that it requires several noise measurements of a single transistor at different temperatures.

5.2 Summary and Discussion

While several works in the literature exist on the temperature dependence of the LFN, they do not necessarily converge to a single theory. While the Dutta-Horn identity provides a strong case for a thermally activated process, conventionally used compact models (such as BSIM, PSP, ACM and EKV) still employ elastic tunnelling to account for the distribution of time constants (HUNG et al., 1990b, 1990b; ARNAUD; GALUP-MONTORO, 2003; ARNAUD; GALUP-MONTORO, 2004; MAVREDAKIS et al., 2016). Moreover, statistical studies on the temperature dependence of the $1/f$ are lacking, as most results shown in this chapter are for individual devices.

Identifying these gaps, this work provides a methodology to study, statistically, the temperature dependence of the LFN. Based on the work of Dutta and Horn (1981) it is clear that a thorough statistical analysis of the frequency dependence of the fundamental LFN sources is also necessary, given its intimate relation to the temperature.

6 NOISE MEASUREMENTS

The DC and LFN measurements were performed on large populations (from 43 up to 320 devices) using the EDGE^{TM} system from Cascade Microtech, depicted in Figure 6.1, at NXP Semiconductors, Eindhoven, The Netherlands. The measurements were supervised and conducted by Dr. Hans Tuinhout and technician Adrie Zegers-van Duijnhoven. Three different CMOS technologies from different foundries[1] — 140-nm, 65-nm and 40-nm — were analysed under several bias conditions. All devices were measured over a frequency range from 10 Hz to 100 kHz. Averaging was set to 20 times for the lowest band (10-100 Hz) and 80 times for the highest bands (TUINHOUT; DUIJNHOVEN, 2013). Unless stated otherwise, the measurements were conducted at 25 ºC.

Figure 6.1: EDGE^{TM} low-frequency noise measurement system.

Source: Tuinhout and Duijnhoven (2013)

The schematic for the low-frequency noise measurement is shown in Figure 6.2. The source and load resistors, R_s and R_{load}, respectively, set the impedance conditions for the device-under test (DUT) during noise measurements and can be adjusted to accommodate different devices. The low noise amplifier (LNA) amplifies the noise signals from the DUT without significantly adding noise of its own. Its performance is determinant for the system noise floor. The filter units (low-pass filters) block the noise generated from the SMUs. The dynamic signal analyser (DSA) conditions and converts the signal to a digital format so that it can be processed by a computer, where the Fast Fourier Transform (FFT) is determined (HANSEN, 2009).

The frequency at which the frequency response of the system dominates the be-

[1] Undisclosed for contractual reasons.

Figure 6.2: Schematic of low-frequency noise test setup.

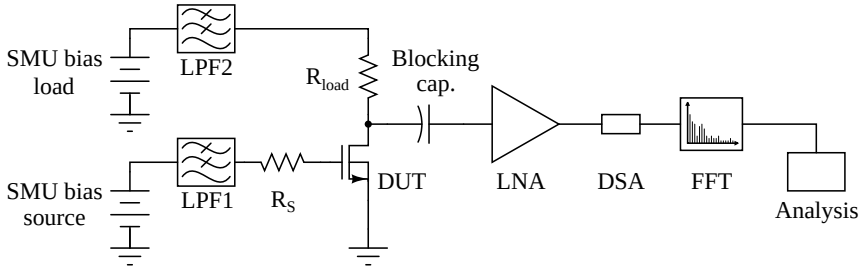

Source: Adapted from Hansen (2009)

haviour of the noise PSD is called *roll-off frequency*. It can be calculated as

$$f_{rolloff} = \frac{1}{2\pi RC}, \tag{6.1}$$

where R is the Thevenin equivalent of the resistive loads and C is the capacitance of the measuring system and cables. The load resistor can be optimized in order to increase the roll-off frequency.

Notice that the estimation of the PSD is performed using a non-parametric method and, therefore, is inherently noisy, particularly for low frequencies, where the averaging is lower (20 times instead of 80 times). Therefore, additional smoothing of the spectra was performed via MATLAB. Figure 6.3 illustrate the data before and after the smoothing.

Figure 6.3: LFN spectra of a) four small-area NFETs and b) three large-area NFETs and their respective smoothed spectra (red line).

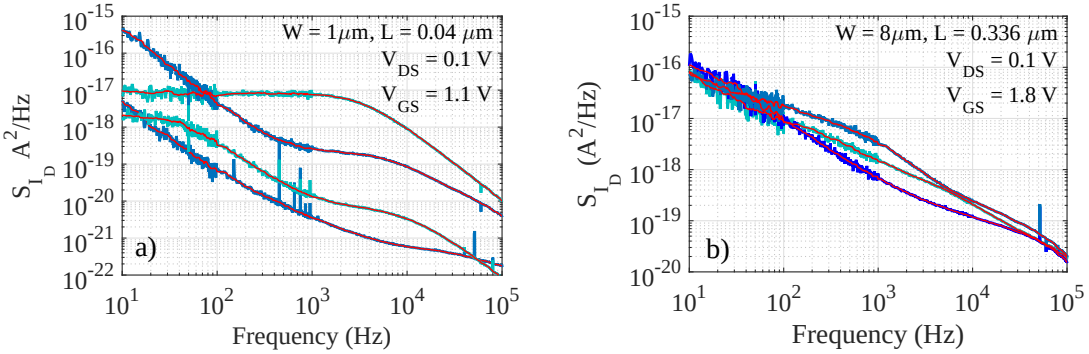

For all measurements presented in this work, the statistical uncertainty is displayed through error bars obtained using bootstrapping, which is a technique to estimate the sample distribution that relies on random sampling with replacement. In this work, the size of the bootstrapping samples are the same as that of the original sample, as proposed by Efron (1979). Unless stated otherwise, the number of bootstrapping samples is equal to 5,000.

This chapter presents the measured data from a statistical standpoint. First, the distribution of the LFN PSD at a given frequency is analysed, followed by its expected value and variance. Then, the reproducibility of the measurements are verified, in order to ascertain that the LFN PSD is unchanged with time (i.e. the noise process is wide-sense stationary). The average power integrated over a bandwidth is also discussed. Finally, an analysis of the spectra of small-area devices as a function of temperature is presented.

6.1 Distribution

Based on the works of Yu et al. (2012) and Banaszeski da Silva et al. (2014), as well as experimental data obtained from several populations from three different technology nodes (140-nm, 65-nm and 40-nm), the LFN at a given frequency is found to be approximately log-normally distributed. By definition, a log-normal distribution is normally distributed in log-scale, i.e. if X is a log-normally distributed random variable, then $\mathrm{Y} = \ln(\mathrm{X})$ is normally distributed.

By establishing that LFN PSD at a given frequency is, approximately, log-normally distributed, it is possible to estimate the expected value and variance of the distribution using the maximum likelihood estimators of the log-normal distribution, as performed by Banaszeski da Silva et al. (2014) and Banaszeski da Silva et al. (2016). These parameters are

$$\mu = \mathrm{E}\left[\ln(\mathrm{X})\right] , \tag{6.2}$$

$$\sigma = \mathrm{SD}\left[\ln(\mathrm{X})\right] , \tag{6.3}$$

where **SD** is the standard deviation operator. Using these parameters, the expected value and variance of a log-normal distributed population can be estimated from the sampled data using

$$\mathrm{E}[\mathrm{X}] = e^{\mu+\frac{1}{2}\sigma^2} , \tag{6.4}$$

$$\mathrm{Var}[\mathrm{X}] = \left(e^{\sigma^2} - 1\right) e^{2\mu+\sigma^2} . \tag{6.5}$$

Figures 6.4 to 6.6 display the quantile-quantile plot (QQ-Plot) of several LFN measurements from different populations. The natural logarithm of the noise quantity (data quantiles) is displayed on the y-axis. Using standard normal quantiles on the x-axis,

if the data falls on a straight line, it indicates that the data is normally distributed. Though small deviations are observed, it is clear that the measured data follow a straight line, indicating a normal behaviour, meaning the S_{I_D} of both N- and PFETs are well-described by a log-normal distribution.

Figure 6.4: Quantile plot of the LFN PSD at 20 Hz for six 43-DUT a) NFET and b) PFET populations (140-nm). Bias conditions are $V_{GS} = 1.8$ V and $V_{DS} = 0.1$ V.

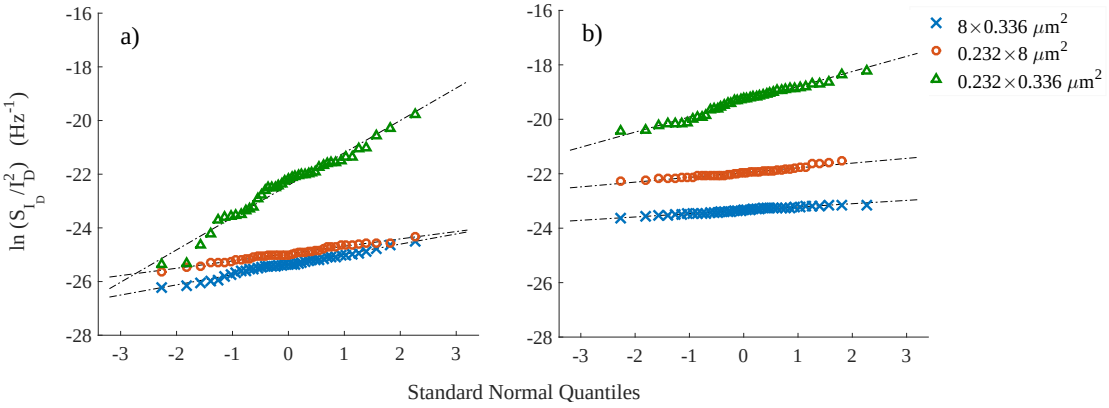

Figure 6.5: Quantile plot of the LFN PSD at 20 Hz for six 60-DUT a) NFET and b) PFET populations (40-nm node). Bias conditions are $V_{GS} = 0.9$ V and $V_{DS} = 50$ mV.

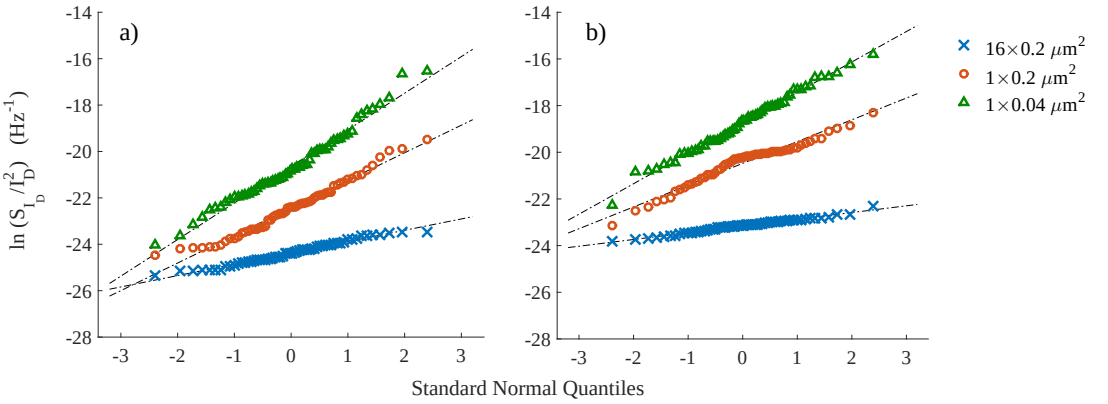

Figure 6.6: Quantile plot of the LFN PSD at 20 Hz for three 282-DUT NFET populations (65-nm node). Bias conditions are $V_{GS} = 1.2$ V and $V_{DS} = 0.5$ V.

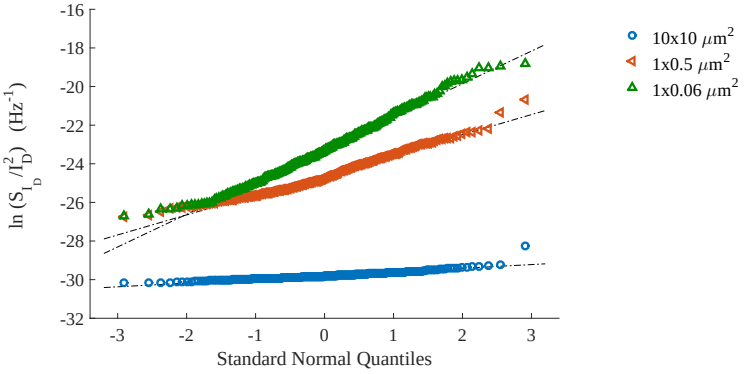

While measurements under low drain bias (uniformly charged channel conditions) usually display approximately log-normal behaviour, as shown in figures 6.4 to 6.6, deviations may appear under high drain bias, particularly for long-channel devices. Figure 6.7a illustrates the deviation observed in a 160-DUT 1 μm long NFET population. Bias conditions are $V_{GS} = 0.7$ V and $V_{DS} = 0.5$ V. From the quantile plot, it is clear that the left-side tail is lighter than the normal distribution, whereas the right-side tail is heavier. To put the length dependence into perspective, figure 6.7b displays the quantile plot of a 0.04 μm long NFET population under the same bias conditions. While the left-side tail is also lighter than the normal distribution, only a slight deviation on the right-side tail is observed. It should be noted that these deviations on the right-side tail are particularly important when considering transistor yield, as outliers (devices with large noise) will appear more often than expected if normality is assumed.

Figure 6.7: Quantile plots of the LFN PSD at 20 Hz for two 160-DUT NFET population (40-nm node): a) long-channel devices and b) short-channel device. Bias conditions are $V_{GS} = 0.7$ V and $V_{DS} = 0.5$ V.

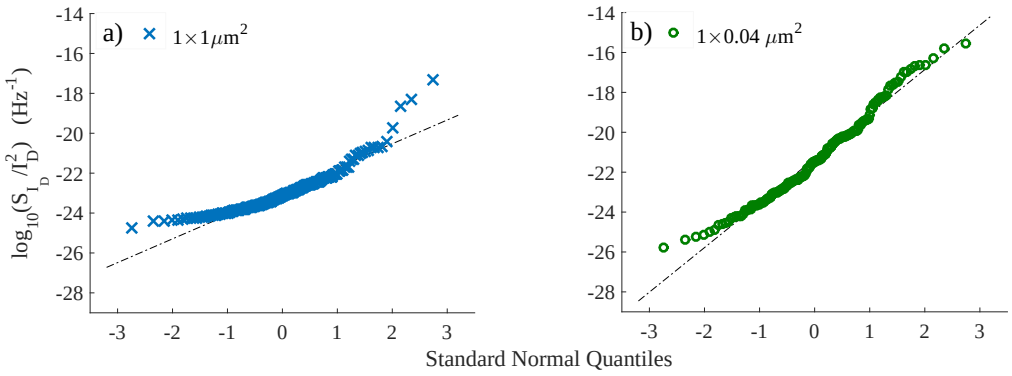

An explanation for this phenomenon was given by Banaszeski da Silva et al. (2016). Under high drain bias (non-uniformly charged channel condition), the trap impact depends heavily on the trap position along the channel. For long-channel devices in saturation regime, traps located near the pocket implants, particularly at the drain side, have their impact amplified. This trap-impact enhancement due to trap position along the channel is important because it may increase the LFN variability of long-channel devices. Accurately modelling this effect is, therefore, crucial for proper noise simulation in electronic circuits.

In order to verify whether the RTS-based model discussed in Section 4.2.4 produce log-normal distribution, Monte Carlo simulations were performed. These simulations, which employed the assumptions discussed in Section 4.2.4, reinforce that the

Figure 6.8: Quantile plots of the LFN PSD at 20 Hz for a) Monte Carlo simulated 500,000-device $0.3\times0.04\mu\text{m}^2$ NFET population and b) measured 320-DUT $0.3\times0.04\mu\text{m}^2$ NFET population. Parameters N_{tr}/γ' and δI_D extracted from b) were 4.9×10^{12} $\text{m}^{-1}\text{eV}^{-1}$ and 5.6×10^{-17} m^2, respectively.

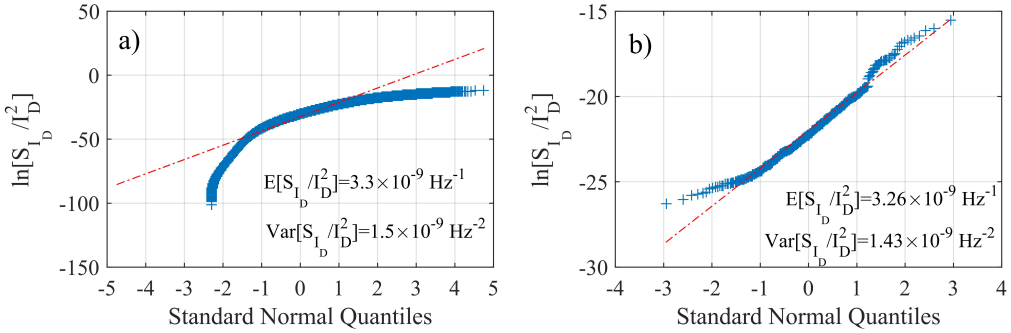

LFN distribution is indeed approximately log-normal for most devices under uniformly inverted channel condition. The predicted behaviour for small-area devices (less than $1\mu m^2$), however, deviates from log-normality. For these devices, the Monte Carlo simulation predicts a different distribution, as shown in figure 6.8a. Measured LFN PSD for smallest area devices available ($0.3 \times 0.04\ \mu m^2$), however, do follow the approximately log-normal behaviour, as seen in figure 6.8b. Notice that the Monte Carlo simulation was performed using the same transistor size and the parameters extracted from figure 6.8b using equations (4.51), (4.54) and (4.57).

While no conclusive explanation for this distinct behaviour between simulation and measurement has been reached, the log-normal behaviour is approached when the average number of traps per device increases. If that is the case, then it would implicate that the exponential distribution of trap impacts is incorrectly assumed. There are several works that attempt to estimate or simulate the distribution of trap impacts (ASENOV et al., 2003; TEGA et al., 2009; TAKEUCHI et al., 2009), being the exponential and log-normal distributions the most prominent ones. Notice that for the Monte Carlo simulations performed, using the exponential distribution of trap impacts resulted the average number of traps to be sufficiently small so that approximately 1% of the simulated devices had no traps whatsoever.

6.2 Expected Value and Variability

In this section the bias dependence of the expected value and variance of the measured data is presented. For low drain bias (i.e. uniformly charged channel condition) the extracted values of K, described in eq. (4.57), are also presented. The experimental results are in agreement with typical $1/f$ noise behaviour of MOSFETs found in other works (SIMOEN; CLAEYS, 1999; MAVREDAKIS; ANTONOPOULOS; BUCHER, 2010).

6.2.1 140-nm Technology

The 140-nm technology devices measured consist of 24 populations (12 NFET and 12 PFET) composed of 43 devices each. Three drain voltages were applied (0.1 V, 0.5 V and 1.8 V) for several different gate biases, from weak inversion to strong inversion. The threshold voltage of the devices is around 0.4 V.

Figure 6.9: Expected value of the normalized LFN PSD at 20 Hz as a function of gate and drain bias for two 43-DUT NFET populations (140-nm technology). Both device populations have the same width (8 μm), but different lengths (a) 0.336 μm and b) 8 μm).

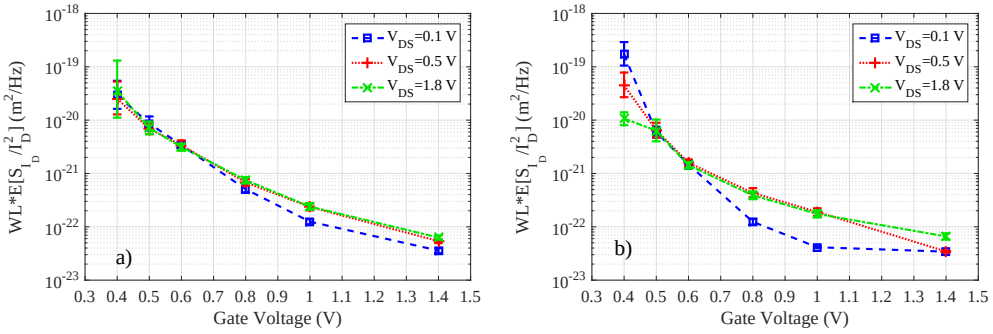

Figure 6.10: Expected value of the normalized LFN PSD at 20 Hz as a function of gate and drain bias for two 43-device NFET populations. Both device populations have the same length (0.16 μm), but different widths (a) 0.232 μm and b) 8 μm).

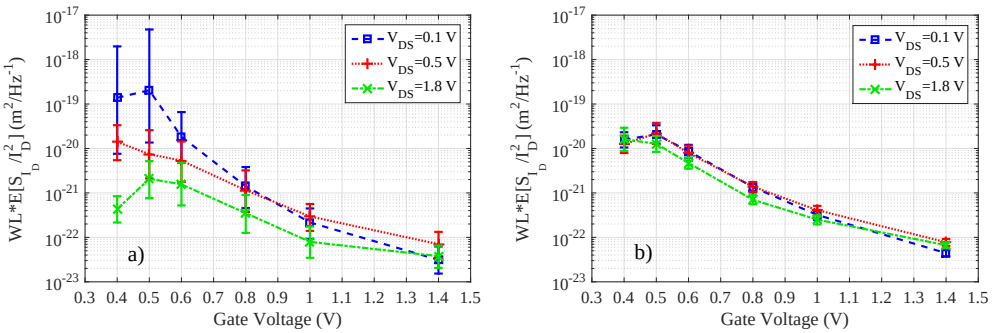

Figure 6.11: Expected value of the normalized LFN PSD at 20 Hz as a function of gate and drain bias for two 43-device PFET populations. Both device populations have the same width (8 μm), but different lengths (a) 0.336 μm and b) 8 μm).

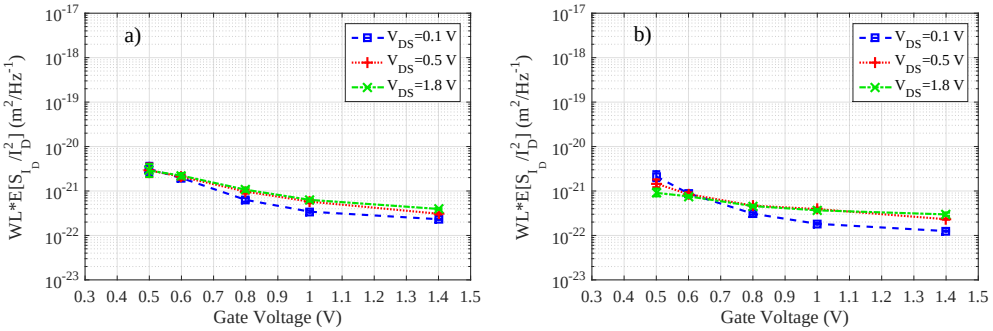

Figure 6.12: Expected value of the normalized LFN PSD at 20 Hz as a function of gate and drain bias for two 43-device PFET populations. Both device populations have the same length (0.16 μm), but different widths (a) 0.232 μm and b) 8 μm).

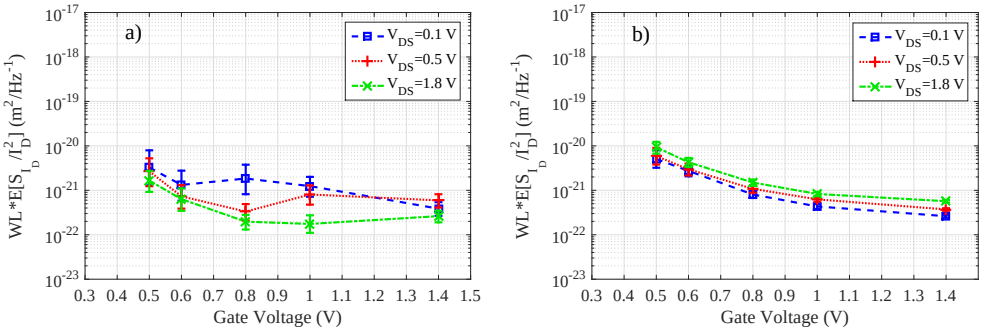

The expected value of the LFN PSD as a function of gate voltage for four different geometries is presented in Figures 6.9 to 6.12. From moderate to strong inversion, the expected value of S_{I_D}/I_D^2 shows a stronger bias dependence for NFET than for PFETs.

The standard deviation of $\ln\left[S_{I_D}/I_D^2\right]$ as a function of area, Figure 6.13, did not follow a $1/\sqrt{WL}$ dependence, but rather one that follows equation (4.56) (BANASZESKI DA SILVA et al., 2014).

Figure 6.13: Standard deviation of $\ln(S_{I_D}/I_D^2)$ as a function of a) $1/\sqrt{WL}$ and b) WL for ten 43-device NFET populations. Bias conditions are $V_{DS} = 0.1$ V and $V_{GS} = 1.4$ V.

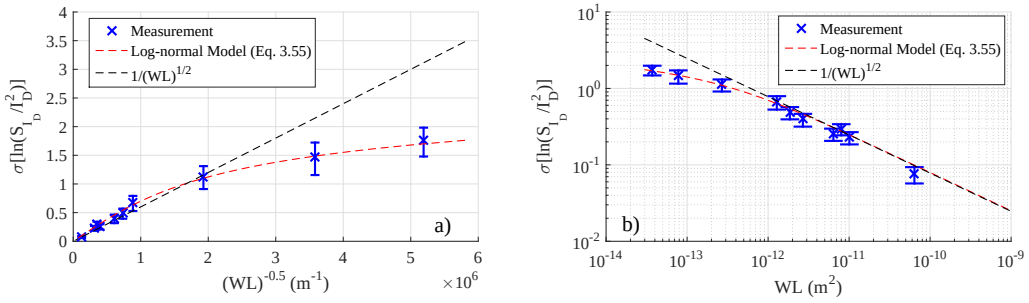

Under uniformly charged channel conditions, a constant K parameter — i.e. the normalized variance multiplied by the area, discussed in section 4.2.4.2 — is able to describe the LFN variability for all geometries, following (4.56) (BANASZESKI DA SILVA et al., 2014). The K parameter extracted from ten 43-device NFET populations, each with a different geometry, is shown in Figure 6.14.

Figure 6.14: Extracted and fitted K parameter as a function of area WL for ten 43-device NFET populations. Bias conditions are $V_{DS} = 0.1$ V and $V_{GS} = 1.4$ V.

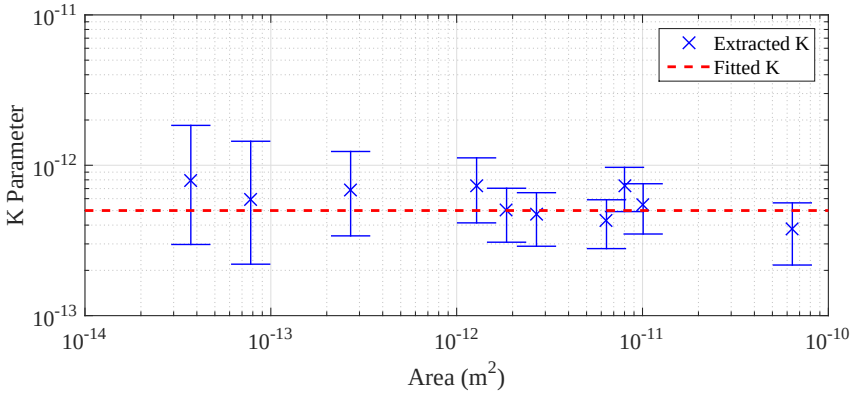

Under high drain bias, however, the enhancement of trap impacts near the drain region causes long channel devices to exhibit larger-than-predicted variability. Figure 6.15 displays the standard deviation of $\ln\left[S_{I_D}/I_D^2\right]$ as a function of area under high drain bias, in which it is visible that the variability in long-channel devices deviates from the behaviour predicted under uniformly inverted channel condition.

Figure 6.15: Standard deviation of $\ln\left[S_{I_D}/I_D^2\right]$ as a function of area for two 43-device NFET populations. Bias conditions are a) $V_{DS} = 0.5$ V and $V_{GS} = 1.4$ V and b) $V_{DS} = 1.8$ V and $V_{GS} = 1.4$ V. Deviations from the predicted behaviour are observed for long channel devices when $V_{DS} > V_{GS} - V_T$

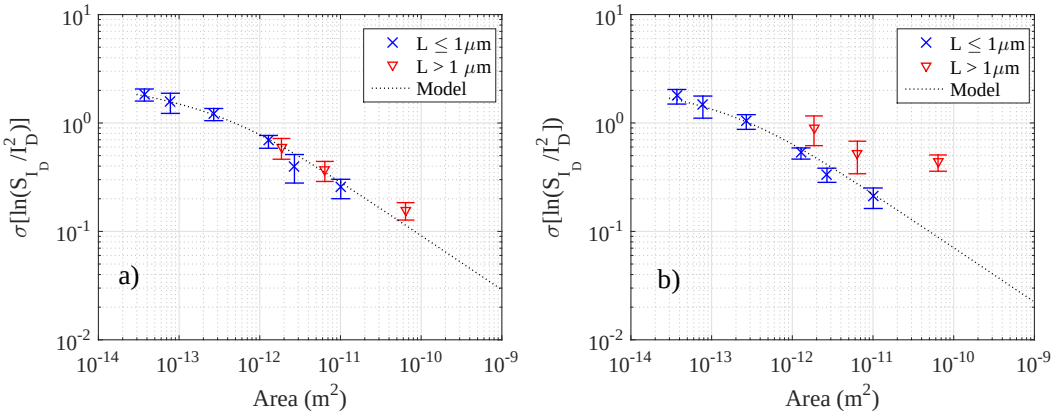

6.2.2 65-nm Technology

For the 65-nm technology, devices from two different foundries (A and B) were measured. From foundry A, two 68-device NFET populations were measured at 4 different bias conditions. From foundry B, three 282-device NFET populations were measured, also at 4 different bias. The expected value of the normalized LFN PSD as a function of the $I_D \cdot L/W$ is shown in Figure 6.16. Note that for comparing two different technology process, using the normalized drain current instead of the gate voltage is more convenient.

Notice that the noise levels are similar for both technologies (devices from foundry B show slightly lower noise levels). Additionally, both technology processes display similar K parameter (normalized variability), as shown in Figure 6.17), indicating that N_{tr}/γ' is similar for both technology processes. The increased variability observed for the $10 \times 10 \mu m^2$ at lower gate biases is attributed to the increased impact of the halo implants in this region of operation (BANASZESKI DA SILVA et al., 2016).

Figure 6.16: Expected value of the normalized LFN PSD at 20 Hz as a function of the normalized drain current ($I_D \cdot L/W$) for two 68-device NFET populations from foundry A and three 282-device NFET populations from foundry B ($V_T \approx 0.4$ V).

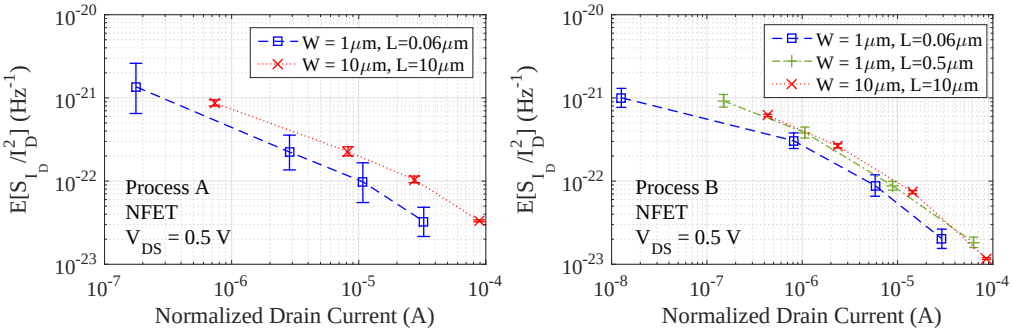

Figure 6.17: K parameter at 20 Hz as a function of the normalized drain current ($I_D \cdot L/W$) for two 68-device NFET populations from foundry A and two 282-device NFET populations from foundry B (65-nm node).

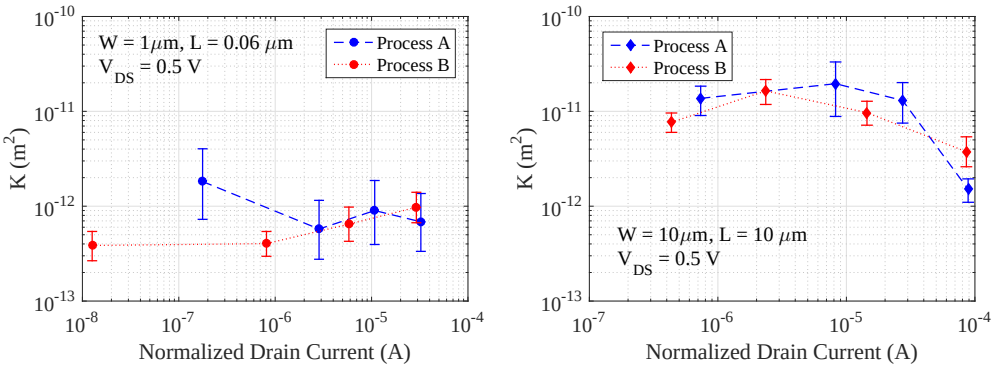

6.2.3 40-nm Technology

The 40-nm technology devices measured consist of 10 populations (5 NFET and 5 PFET) composed of 60 devices each. These populations were measured at three drain voltages (50 mV, 0.55 V and 1.1 V) for several different gate biases, from weak to strong inversion. Additionally, two 180-device NFET populations were also measured under $V_{DS} = 0.5$ V. The threshold voltage of these devices is approximately 0.4 V.

The expected value of the LFN PSD as a function of gate voltage for two different geometries is presented in Figures 6.18 and 6.19. As previously observed for the 140-nm technology, from moderate to strong inversion, the expected value of S_{I_D}/I_D^2 shows a stronger bias dependence for NFET than for PFETs.

Figure 6.18: Expected value of the normalized LFN PSD at 20 Hz as a function of gate and drain bias for two 60-DUT NFET populations. Both device populations have the same width (1 μm), but different lengths a) 1 μm and b) 0.2 μm).

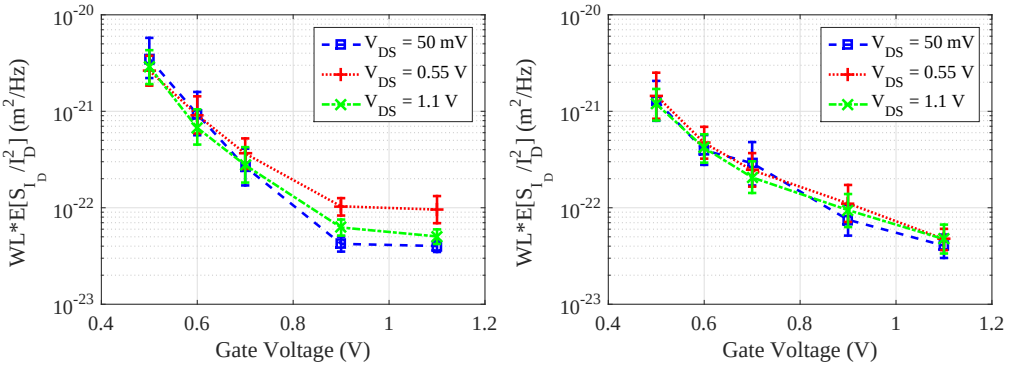

Figure 6.19: Expected value of the normalized LFN PSD at 20 Hz as a function of gate and drain bias for two 60-DUT PFET populations. Both device populations have the same width (1 μm), but different lengths a) 1 μm and b) 0.2 μm).

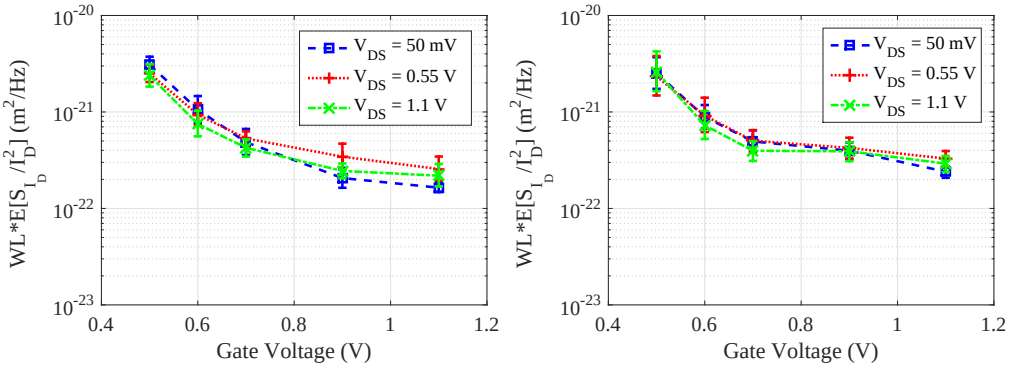

In figure 6.20, the expected value of the normalized LFN PSD at 20 Hz as a function of drain current and temperature is shown. The advantage of plotting versus drain

current in this case is the fact that the threshold voltage shifts with temperature and, thus, the bias condition $V_{GS} - V_T$ is modified. Notice that the expected value of the LFN is weakly temperature dependent, specially in strong inversion.

Figure 6.20: Expected value of the normalized LFN PSD at 20 Hz as a function of drain current and temperature for two 80-DUT NFET populations.

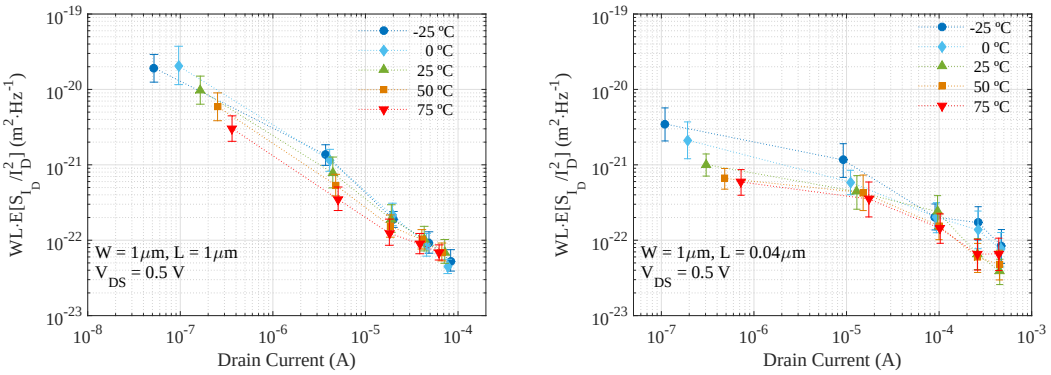

Following the behaviour observed for the 140-nm technology, the standard deviation of $\ln\left[S_{I_D}/I_D^2\right]$ as a function of area, Figure 6.21, did not follow a $1/\sqrt{WL}$ dependence, but rather one that predicted by the log-normal model. Notice that the normalized variability parameter (K) extracted for PFET devices is smaller than that of NFET devices. From equation 4.57, reproduced here for simplicity, it is possible to conclude that the trap density in the area, energy and in the log-domain of time constants ($\mathrm{cm}^{-2}\mathrm{eV}^{-1}$ per neper), $N_{tr}(E_{Fn})/\gamma$, is larger in PFET devices than in NFET devices for this particular technology at the given bias condition.

$$K = \frac{2}{\pi^2 kT}\frac{\gamma'}{N_{tr}(E_{Fn})}\,. \tag{6.6}$$

Figure 6.21: Standard deviation of the natural logarithm of S_{I_D}/I_D^2 for five NFET and PFET devices populations as a function of $1/\sqrt{WL}$ for $V_{DS} = 50$ mV and $V_{GS} = 1.1$ V.

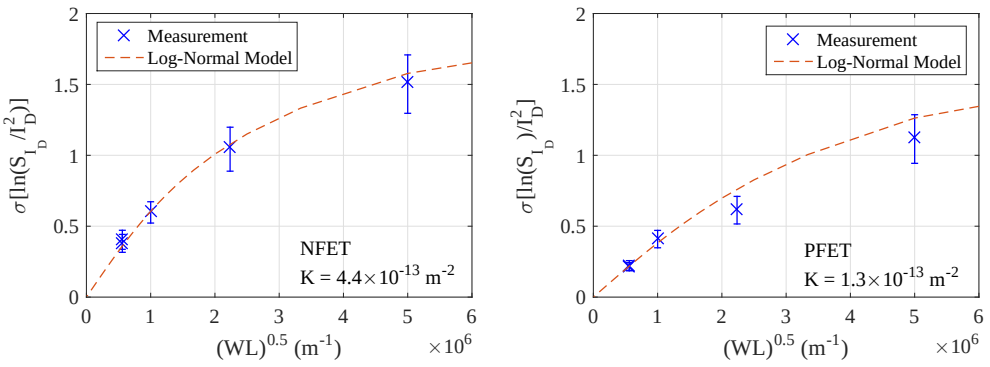

Figure 6.22: Scatter plot of the normalized LFN PSD (S_{I_D}/I_D^2) versus the drain current for two 180-DUT NFET populations. Different colours indicate different gate bias applied.

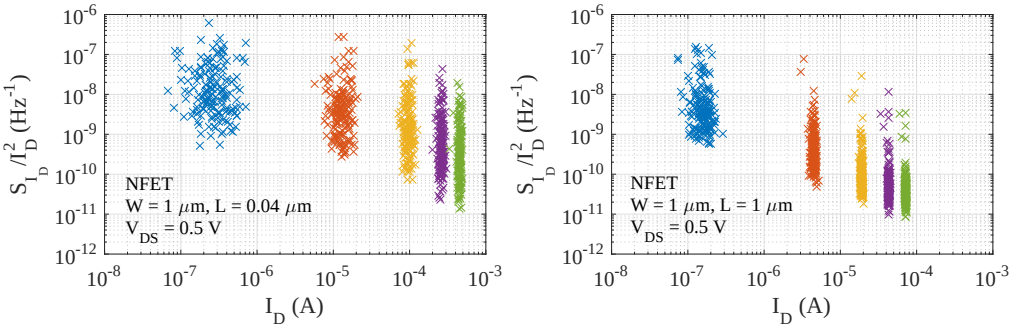

It is important to observe that the normalized LFN PSD (S_{I_D}/I_D^2) is not correlated to the drain current, as shown in Figure 6.22 for two 180-DUT NFET populations. It is also possible to confirm that drain current variability is not the primary source of LFN variability, as the drain current variability is several orders magnitude lower than that of LFN.

6.3 Reproducibility

For the analyses presented in chapter 7 of this work, it is critical that the measured LFN PSD of each device remains the same if the experiment is reproduced after a few hours or days (under the same bias conditions). Particularly for the correlation coefficient analyses presented in Chapter 7 of this work, it is critical to ascertain that defects are not created or annealed during device measurement or wafer storage, i.e. the PSD of the LFN remains roughly unchanged over time.

To verify the reproducibility of the PSD measurements within the desired bandwidth, a population of 282 65-nm technology devices ($W = 1$ μm and $L = 0.06$ μm) was measured twice with seven weeks of interval between experiments. The average and variance of $f \cdot S_{I_D}/I_D^2$ at different bias conditions is shown in Figures 6.23 and 6.24. The multiplication of S_{I_D}/I_D^2 by the frequency is for compactness of the figures. The correlation coefficient as a function of frequency are shown in Figure 6.25. Notice that drain bias is kept low in order to avoid defect creation due to hot carrier injection during measurement.

The near-identical behaviour of the expected value and variance, as well as the high value of correlation coefficient (above 0.95) between experimental results indicate

that the measurement set-up is stable and that the LFN PSD of the population at a given frequency can be considered a stationary random process, i.e. the average and variance do not change over time.

Figure 6.23: Average value of $f \cdot S_{I_D}/I_D^2$ for different frequencies and biases. Blue and red lines indicate the first and second measurements, respectively. Despite the time interval between experiments, the average value falls within the statistical uncertainty obtained using bootstrapping. Drain voltage is 0.5 V.

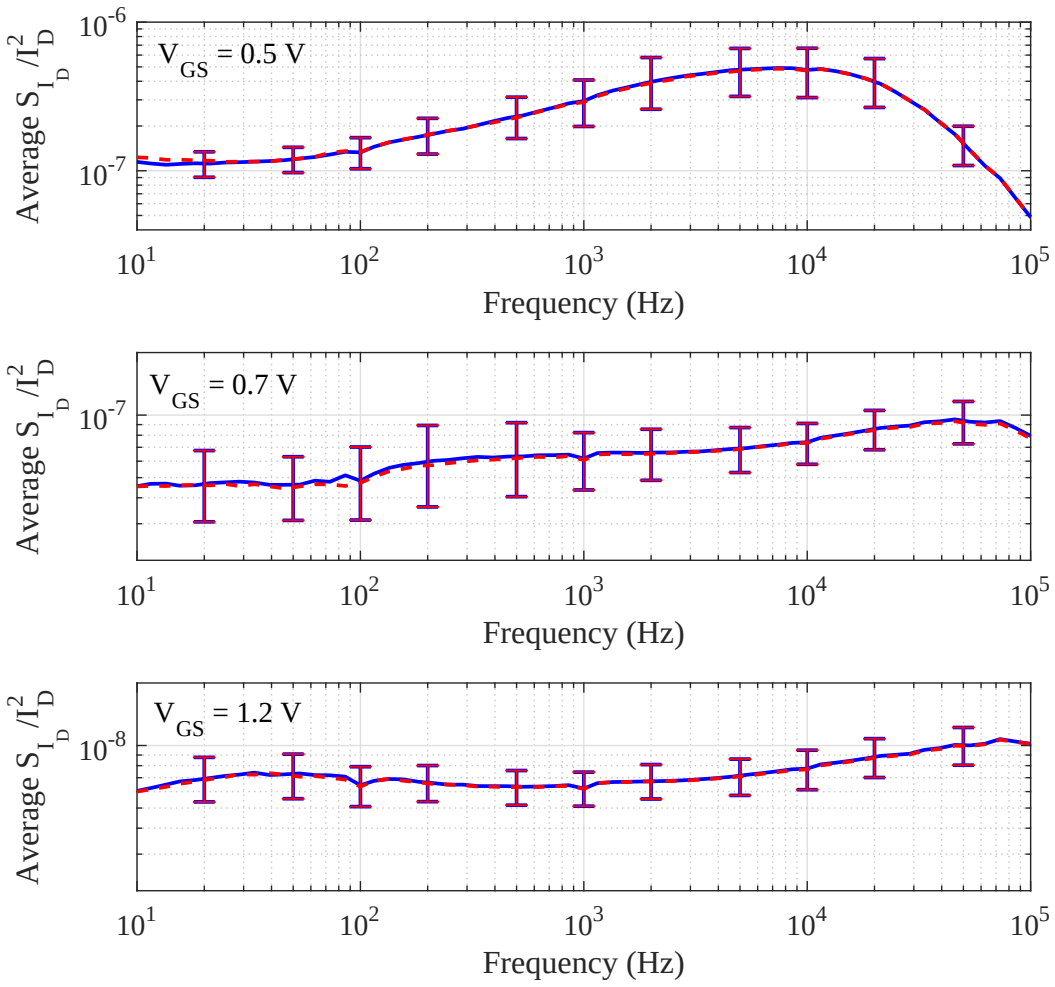

Figure 6.24: Variance of $f \cdot S_{I_D}/I_D^2$ for different frequencies and biases. Blue and red lines indicate the first and second measurements, respectively. Despite the time interval between experiments, the average value falls within the statistical uncertainty obtained using bootstrapping. Drain voltage is 0.5 V.

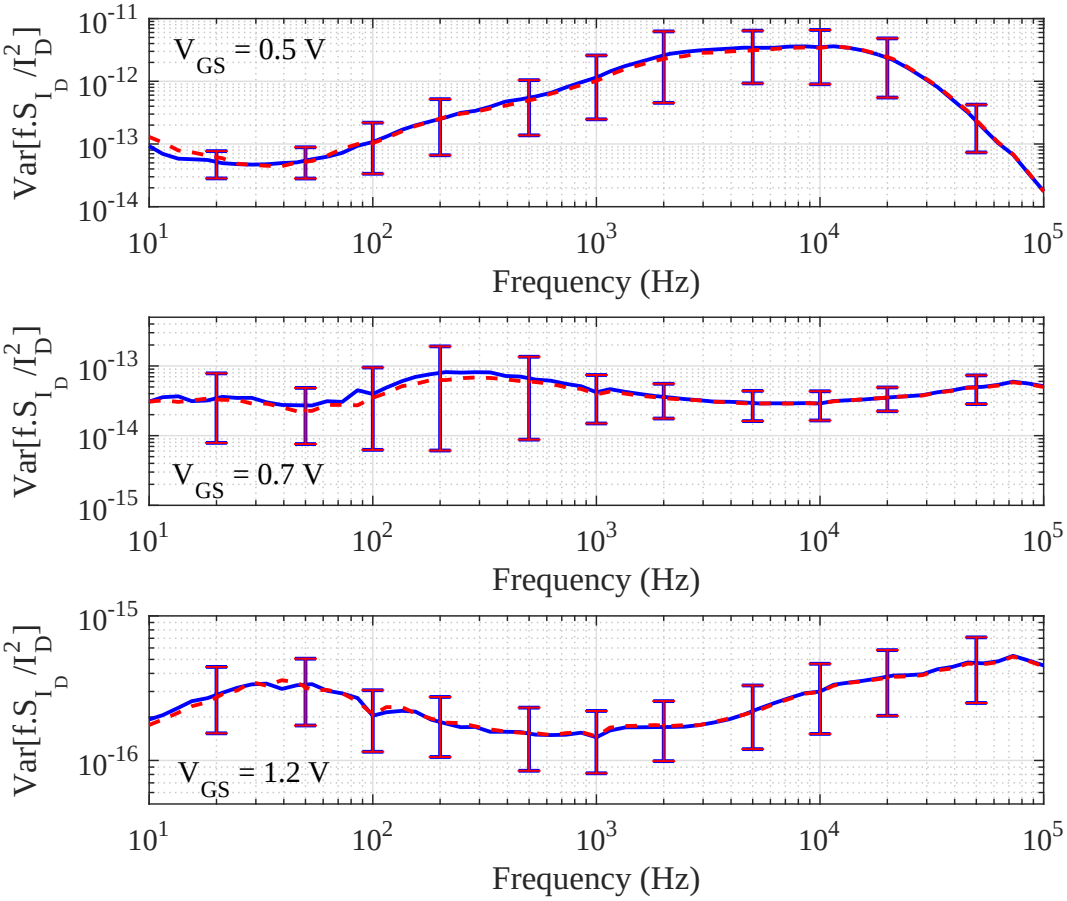

Figure 6.25: Correlation coefficient of S_{I_D}/I_D^2 between experiments 1 and 2 as a function of frequency for different bias. Drain voltage is 0.5 V.

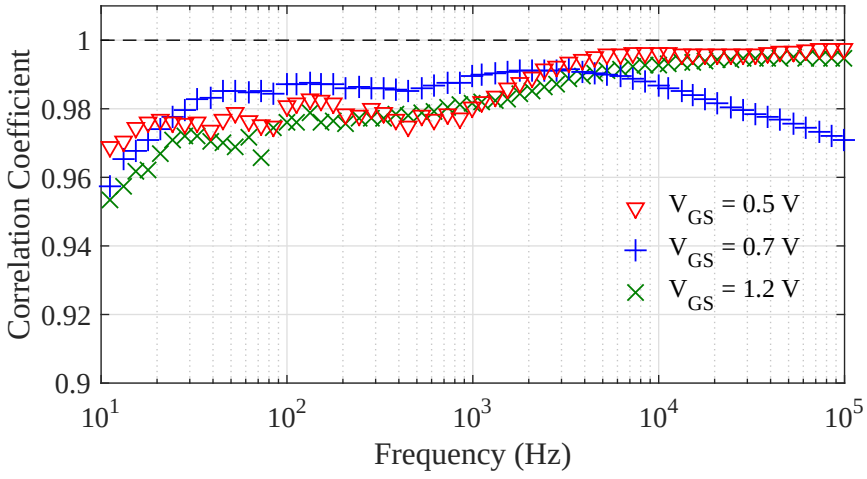

6.4 Noise Power Integrated over a Bandwidth

The noise power of a given device integrated over a bandwidth $[f_L, f_H]$ is given by

$$W_p = \int_{f_L}^{f_H} S_{I_D}(f) df \ . \tag{6.7}$$

The work of Silva, Wirth and Brederlow (2006) demonstrated that for any frequency range region the mean noise as well as the relative error are invariant under a scale transformation $f_H \rightarrow cf_H$ and $f_L \rightarrow cf_L$, where c is a constant. Following the assumptions from Section 4.2.4, under the premise that $f_L > 1/2\pi\tau_{max}$ and $f_H < 1/2\pi\tau_{min}$ (i.e. the observation window is within the log-uniform distribution of time constants), it can be demonstrated that

$$\mathrm{E}\left[W_p\right] = 2\mathrm{E}\left[\Delta I_D\right]^2 \cdot kTWL \cdot \frac{N_{tr}(E_{Fn})}{\gamma} \cdot \ln\left(\frac{f_H}{f_L}\right) \ , \tag{6.8}$$

where $N_{tr}(E_{Fn})/\gamma$ is the trap density in the area, energy and in the log-domain of time constants ($\mathrm{cm}^{-2}\mathrm{eV}^{-1}$ per neper).

Experimental results from two different technologies (40-nm and 65-nm) shown in Figures 6.26 and 6.27 corroborate this finding, given that the quantity $\mathrm{E}\left[W_p\right]/\ln(f_H/f_L)$ is approximately constant, regardless of the bandwidth. Notice that, in Figure 6.26, the same population was measured twice, at different drain bias conditions, whereas two different populations (i.e. different geometries) were measured at the same bias conditions in Figure 6.27.

Figure 6.26: Expected value of the integrated noise normalized by I_D^2 and $\log(f_H/f_L)$ over different bandwidths for a 78-DUT 40-nm technology NFET population ($W = 1\ \mu$m and $L = 1\ \mu$m) under two different drain biases. Dashed red line is a guide for the eye.

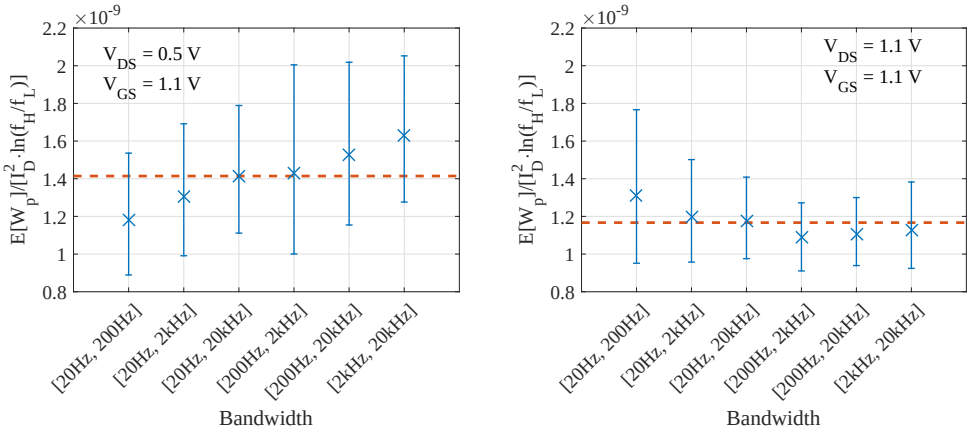

Figure 6.27: Expected value of the integrated noise normalized by I_D^2 and $\log(f_H/f_L)$ over different bandwidths for two 282-DUT 65-nm technology NFET population under $V_{GS} = 1.2$ V and $V_{DS} = 1.2$ V. Dashed red line is a guide for the eye.

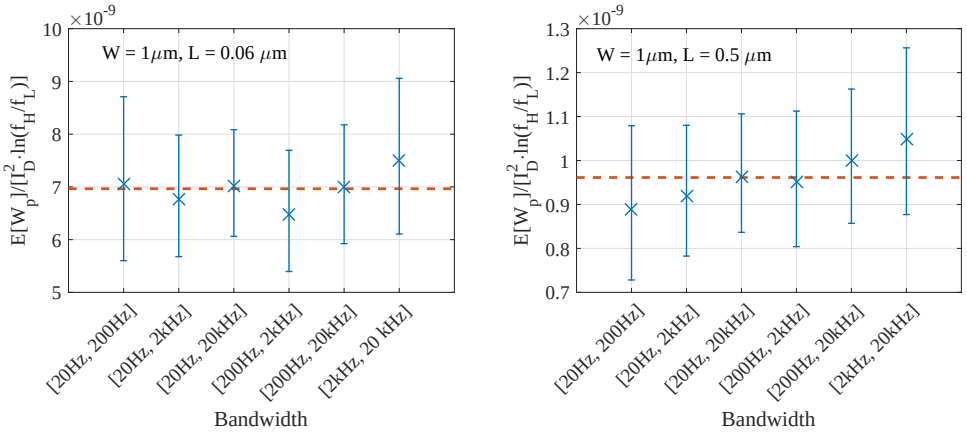

Notice, however, that if the noise is not exactly $1/f$ (i.e. when the distribution of time constants is not exactly uniform in log-scale), the relation is not valid. One example is shown in Figure 6.28 for a 140-nm technology PFET population, in which the frequency exponent is larger than 1.

Figure 6.28: Expected value of the integrated noise normalized by I_D^2 and $\log(f_H/f_L)$ over different bandwidths for two 43-DUT 140-nm technology PFET population under $V_{GS} = 1.8$ V and $V_{DS} = 1.8$ V. Dashed red line in a) represents an ideal $1/f$.

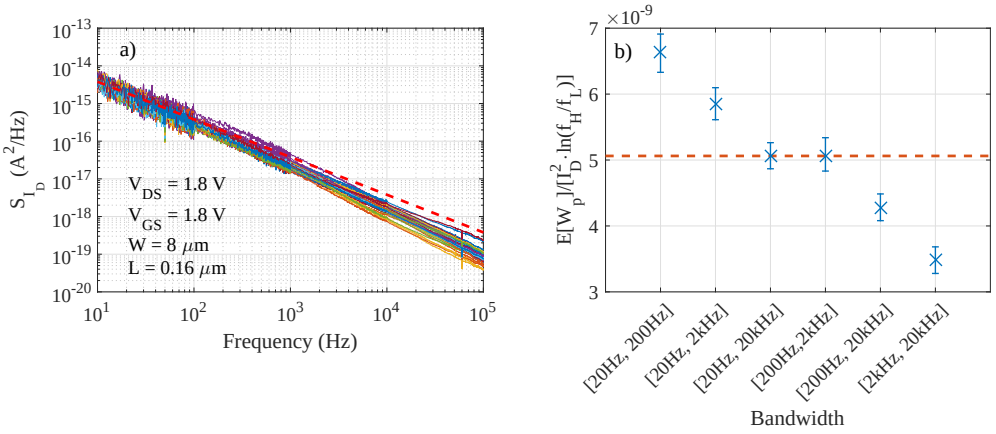

6.5 Analysis of Individual Lorentzians

The identification and analysis of individual Lorentzian spectra enables the verification of basic assumptions, such as the log-uniform distribution of time constants. Each clearly visible Lorentzian spectrum is attributed to the RTS of a single trap, enabling

the extraction of the characteristic time constant of such trap. By multiplying S_{I_D}/I_D^2 by the frequency, the cut off frequency of the trap (f_c) is found at the peaks of $f \cdot S_{I_D}/I_D^2$. The characteristic time constant can then be estimated through $\tau = 1/(2\pi f)$. There are drawbacks to such method though — e.g. Lorentzian are only clearly identifiable in small-area devices and traps that have similar characteristic time constant can be difficult to distinguish —, which are further discussed in this section. For this reason, in chapter 7 a methodology is proposed to extract important information from the LFN spectra without the need of identifying individual Lorentzians; the methodology not only enables analysing large-area devices, but also for small-area devices without visible Lorentzians.

From a 320-DUT NFET population ($W = 0.3\mu$m and $L = 0.04\mu$m), several bumpy, Lorentzian-like, spectra were identified from the LFN PSD at two different temperatures (25 ºC and 50 ºC). The window of observation was set between 20 Hz and 20 kHz. This is due to the fact that at lower frequencies the number of samples is small and, thus, uncertainty is large; at higher frequencies, on the other hand, the noise level approaches the noise floor of the measurement set-up. In Figure 6.29, the LFN PSD of devices with pronounced Lorentzians at both temperatures are shown. Notice that the cut off frequencies of the Lorentzian is increased with increasing temperature, meaning that the characteristic time constant decreased, following a thermally activated process.

Figure 6.29: LFN spectra of two NFET devices at the same bias conditions and at two different temperatures.

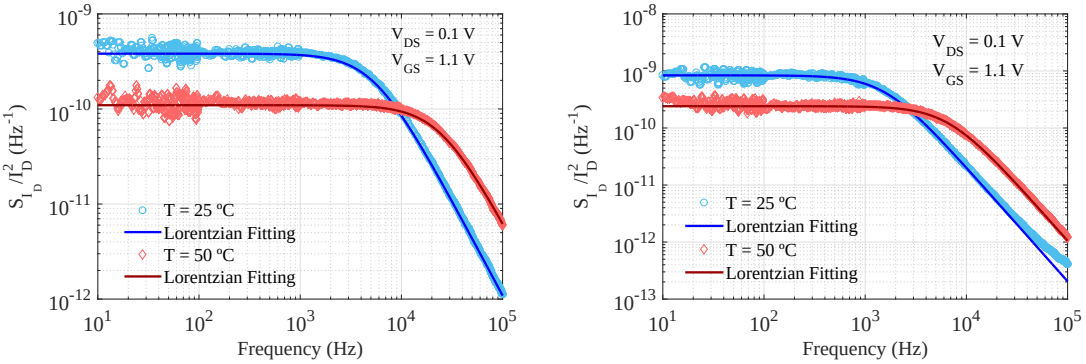

On the other hand, while a Lorentzian spectrum is visible at both temperatures in Figure 6.30, there is little observable shift in the cut-off. This temperature independent behaviour is in line with that expected for direct tunnelling. Overall, however, the majority of the identified Lorentzian spectra seemed to follow a thermally activated behaviour, which is explored further in this section.

Figure 6.30: LFN spectra of an NFET device at the same bias conditions and at two different temperatures.

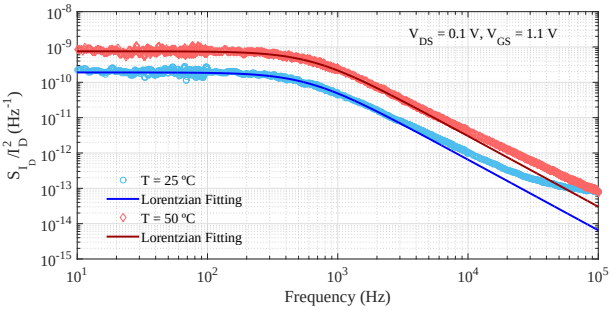

Analysing the behaviour of these Lorentzians individually from an ensemble, however, is not simple. Even in small-area devices, these Lorentzians are not always easily identifiable. Their spectra may be less prominent due to, for example, the presence of other Lorentzians with τ near or within the observation window. Figure 6.31 illustrates two devices with less pronounced, yet identifiable, profiles.

Figure 6.31: LFN spectra of two NFET devices at the same bias conditions and at two different temperatures.

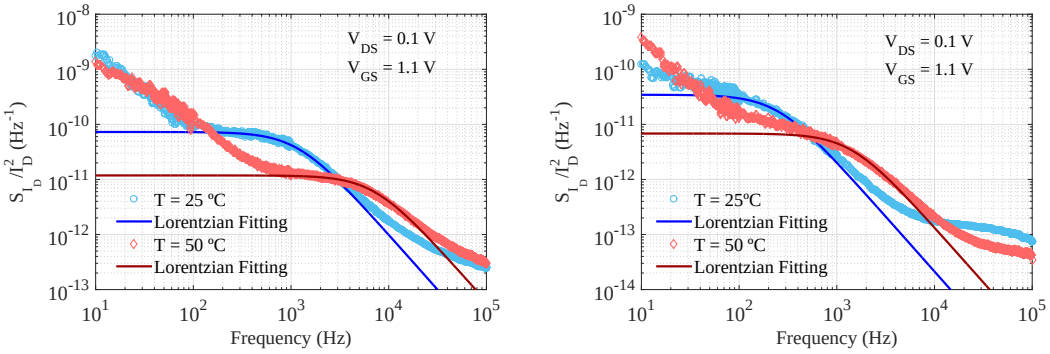

A significant share of devices exhibited no Lorentzians at all at either temperatures. Such devices displayed a approximately $1/f$ noise spectrum, as illustrated in Figure 6.32. Finally, in order to illustrate the difficulty of identifying these individual Lorentzians, Figure 6.33 displays the LFN spectra of a device at 25 ºC and 50 ºC in which the lumps that are not visible to the naked eye may have been incorrectly identified by the algorithm.

From the 320-DUT population, 187 and 193 individual Lorentzians were identified at 25 ºC and 50 ºC, respectively. Figure 6.34 displays the cumulative probability plot of $\log_{10}\tau$ extracted from the measured PSD at 25 ºC and 50 ºC. The linear behaviour indicates the characteristic time constant is approximately uniformly distributed in log scale within the window of observation. From the frequency range defined (20 Hz to 20 kHz), the uniform distribution of $\log_{10}\tau$ spans from $\tau_{min} = 1/(2\pi f_{max})$ to $\tau_{max} = 1/(2\pi f_{min})$.

Figure 6.32: LFN spectra of a device at the same bias conditions at two different temperatures. No visible Lorentzians.

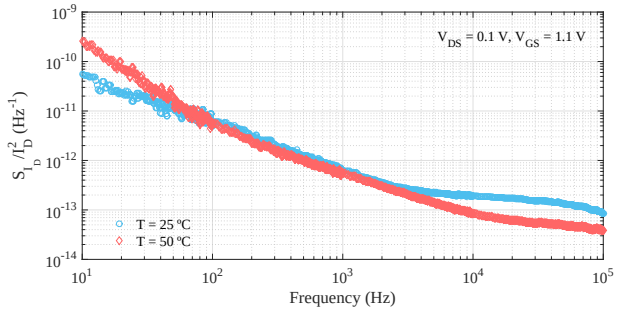

Figure 6.33: LFN spectra of a device at the same bias conditions at two different temperatures. No visible Lorentzians.

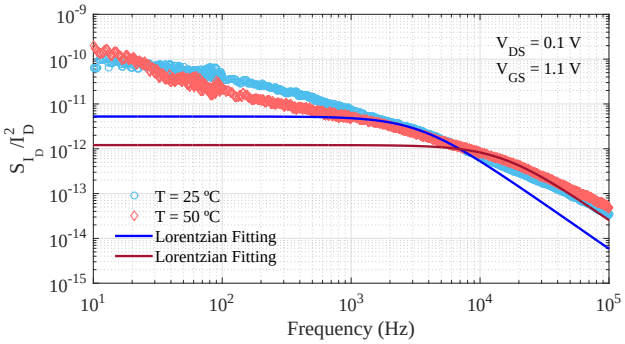

The observed log-uniform distribution of τ reinforce the relation between $1/f$ noise and trap activity, since such distribution produces a $1/f$ spectrum when multiple Lorentzians are present within the observation window (SURDIN, 1939; MCWHORTER, 1957). It is important to observe that, by identifying prominent Lorentzians, only information about traps that contribute significantly to noise power is obtained; thus, it is not possible to ascertain, from this analysis, that the $1/f$ noise in devices in which no Lorentzian profile was identified is also produced by trap activity.

Figure 6.34: Cumulative probability plot compared to the expected uniform distribution of $\log_{10}\tau$. The observation window is defined between 20 Hz and 20 kHz.

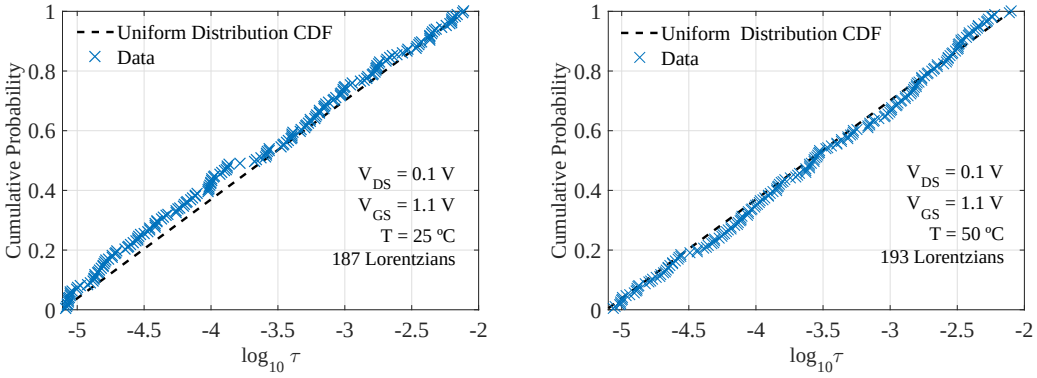

Figure 6.35: Scatter plot of $\log_{10}\tau$ at 25 ºC and 50 ºC for the condition when $\tau(25\,^{\circ}\mathrm{C}) > \tau(50\,^{\circ}\mathrm{C})$, meaning that the Lorentzian is shifter towards higher frequencies with increasing temperature (indicating thermal activation). The number of Lorentzians that satisfy the restriction is 131.

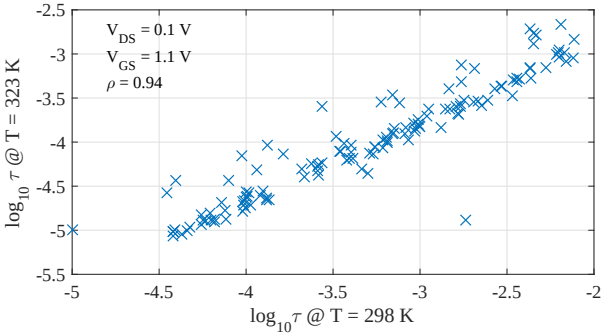

Figure 6.35 displays the scatter plot of $\tau(25^{\circ}\mathrm{C})$ versus $\tau(50\,^{\circ}\mathrm{C})$, aiming to identify whether the characteristic time constants extracted at 25 ºC and 50 ºC are correlated. Assuming thermal activation, then $\tau(25\,^{\circ}\mathrm{C}) > \tau(50\,^{\circ}\mathrm{C})$; thus, only Lorentzians that satisfy this constraint were included in the analysis (a total of 131 spectra). While the correlation is strong ($\rho = 0.94$), the fact that only Lorentzians that satisfied the constraint were included in the analysis shuns any attempts to generalize the behaviour observed for the LFN as a whole. Nevertheless, there is strong indication that thermal activation governs the activity of the observed traps.

Conversely, if τ is assumed to originate from a thermally activated process, then the activation energy can be estimated using

$$E_B = \ln\left(\frac{\tau(T_1)}{\tau(T_2)}\right) \cdot \frac{kT_1T_2}{(T_2 - T_1)} \,. \tag{6.9}$$

If equation (6.9) is applied to data from 6.35, the resulting distribution is not uniform (as shown in figure 6.36). This result indicates that simple thermal activation may not be enough to account for the temperature dependence of τ.

Figure 6.36: Cumulative probability plot of the activation energy extracted from (6.9). The distribution is clearly not uniform.

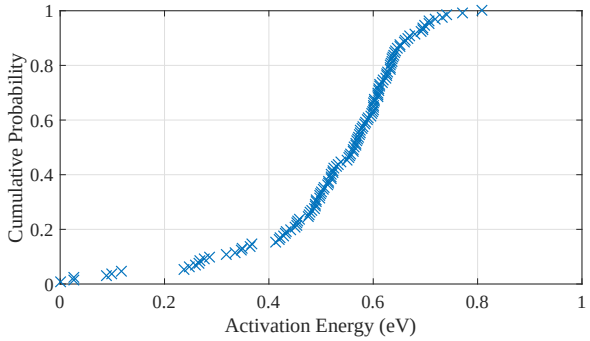

6.6 Summary and Discussion

This chapter provided a discussion on the measured LFN spectra from three different technology nodes (40-nm, 65-nm and 140-nm). The noise distribution at a given frequency, expected value and variance were evaluated, as well the integrated power over a bandwidth. The results were consistent with other works in the literature. Additionally, noise measurements were shown to remain stable when measured after the span of a few weeks.

The analysis of individual Lorentzians from the LFN spectra measured reinforces the view that thermal activation governs the capture and emission process. However, it is insufficient for determining whether trapping/de-trapping is the dominant LFN mechanism; whether thermal activation is primarily responsible for the log-uniform distribution of time constants; or whether the conclusions hold true when no Lorentzians are visible ($1/f$ spectrum). In order to provide a more robust analysis, a statistical methodology is developed and presented in the following chapter of this work.

7 CORRELATION COEFFICIENT ANALYSES

In this chapter, a novel noise analysis technique which is extremely sensitive to the physical mechanisms assumed for the interpretation and modelling of the LFN in MOSFETs is proposed. This technique is based on the analysis of the autocorrelation of the LFN PSD, meaning the analysis is performed entirely in frequency domain. Using this methodology it is possible to draw valuable conclusions about the frequency, temperature and bias dependence of the fundamental noise sources underlying the $1/f$ noise in MOSFETs, as well as the origin of the trapping mechanism.

Notice that the term *autocorrelation* here refers to the fact that the technique estimates the correlation between the noise power density of a given population at a given condition (bias, temperature, frequency), with the same population at a different condition — e.g. $S_{I_D}(f)$ and $S_{I_D}(f+\Delta f)$. While, in principle, such autocorrelation could be defined as *autocorrelation functions* (in frequency domain), the author refrains from using the term in order to avoid misinterpretation given the classic usage of the term for time functions [1].

7.1 Correlation Coefficient Extraction

As discussed in section 6.1, the LFN PSD follows a log-normal distribution. Therefore, the extraction of the correlation coefficient from experimental data was performed using the maximum likelihood estimators from the log-normal distribution. From (4.58), rewritten for convenience, the correlation coefficient between two random variables, X and Y, is given by

$$\mathrm{R}[\mathrm{X},\mathrm{Y}] = \frac{\mathrm{Cov}[\mathrm{X},\mathrm{Y}]}{\sqrt{\mathrm{Var}[\mathrm{X}]\cdot\mathrm{Var}[\mathrm{Y}]}} \ . \tag{7.1}$$

Using the definition of Covariance, (4.69), and the properties of the log-normal distribution

$$\mathrm{E}[\mathrm{X}] = e^{\mu_x+\frac{1}{2}\sigma^2} \ , \tag{7.2}$$

$$\mathrm{Var}[\mathrm{X}] = \left(e^{\sigma_x^2}-1\right)e^{2\mu_x+\sigma^2} \ , \tag{7.3}$$

[1] See section 2.2.

$$\mathrm{E}[\mathrm{XY}] = e^{\mu_x+\mu_y+\frac{1}{2}\left(\sigma_x^2+2\rho\sigma_x\sigma_y+\sigma_y^2\right)} , \tag{7.4}$$

where μ_x and μ_y are the expected value of the logarithm of the random variables X and Y, respectively (notice that ln(X) and ln(Y) are normally distributed); σ_x and σ_y are the standard deviations of ln(X) and ln(Y), respectively; and ρ is the correlation coefficient between ln(X) and ln(Y), (7.1) can be rewritten as

$$\mathrm{R}[\mathrm{X},\mathrm{Y}] = \frac{e^{\rho\sigma_x\sigma_y}-1}{\sqrt{\left(e^{\sigma_x^2}-1\right)\cdot\left(e^{\sigma_y^2}-1\right)}} \tag{7.5}$$

for log-normal distributions. This expression will be used throughout this chapter to extract the correlation coefficient between measured LFN PSD populations.

7.2 Frequency Autocorrelation

The frequency autocorrelation analysis provide valuable information on the frequency dependence of the fundamental noise sources underlying the $1/f$ noise. In order to verify whether the assumption that the $1/f$ spectrum observed in large-area devices is indeed composed of a superposition of Lorentzians, an analytical expression for the correlation coefficient in terms of Δf is derived from the RTS framework and compared to the data.

7.2.1 Model Derivation

The correlation coefficient of the LFN PSD in terms of Δf when the LFN is assumed to result from multiple switching traps — i.e. multiple superimposed Lorentzian spectra, $L(f)$ — can be calculated theoretically using (4.71) as

$$\mathrm{R}\left[S_{I_D}(f_{ref}), S_{I_D}(f_{ref}+\Delta f)\right] = \frac{\mathrm{E}\left[L(f_{ref})\cdot L(f_{ref}+\Delta f)\right]}{\sqrt{\mathrm{E}\left[L(f_{ref})^2\right]\cdot\mathrm{E}\left[L(f_{ref}+\Delta f)^2\right]}} , \tag{7.6}$$

where $L(f)$ is given in the context of RTS by (4.14), rewritten here for convenience

$$L(f) = 4{\Delta I_D}^2\cdot\frac{\beta}{(1+\beta)^2}\cdot\frac{\tau}{1+(2\pi f\tau)^2} , \tag{7.7}$$

where ΔI_D, β, and τ are the current fluctuation caused by a trap, the ratio between the emission and capture time constants (τ_e/τ_c) of a trap and the characteristic time constant of a trap ($1/\tau = 1/\tau_c + 1/\tau_e$), respectively. The ratio between emission and capture times is given by $\beta = exp[(E_F - E_T)/kT]$, where E_T, E_F, k, and T are the trap energy, Fermi energy, Boltzmann's constant, and temperature, respectively. For simplicity, f_{ref} and $f_{ref} + \Delta f$ are substituted for f_1 and f_2, respectively.

The problem is thus reduced to the solution of $\mathrm{E}[L(f_1) \cdot L(f_2)]$ and $\mathrm{E}\left[L(f_1)^2\right]$. Using

$$\mathrm{E}[g(\mathrm{X})] = \int_{-\infty}^{\infty} g(x) \cdot f_{\mathrm{X}} dx \,, \tag{7.8}$$

yields

$$\mathrm{E}\left[L(f_1)^2\right] = 16 \cdot \int_{-\infty}^{\infty}\int_{-\infty}^{\infty}\int_{-\infty}^{\infty} {\Delta I_D}^4 \cdot \frac{\beta^2}{(1+\beta)^4} \cdot \frac{\tau^2}{[1+(2\pi f_1 \tau)^2]^2} f_{\Delta I_D} f_\beta f_\tau d\Delta I_D d\beta d\tau \,, \tag{7.9}$$

and

$$\begin{aligned} &\mathrm{E}[L(f_1) \cdot L(f_2)] \\ &= 4 \cdot \int_{-\infty}^{\infty}\int_{-\infty}^{\infty}\int_{-\infty}^{\infty} {\Delta I_D}^4 \cdot \frac{\beta^2}{(1+\beta)^4} \cdot \frac{\tau^2}{[1+(2\pi f_1 \tau)^2] \cdot [1+(2\pi f_2 \tau)^2]} f_{\Delta I_D} f_\beta f_\tau d\Delta I_D d\beta d\tau \,. \end{aligned} \tag{7.10}$$

If the random variables ΔI_D, β and τ of any given trap are assumed to be frequency independent (meaning they remain constant at all frequencies), τ to be log-uniformly distributed between τ_{min} and τ_{max}, and the channel to be uniformly inverted (no position dependence of the traps), (7.6) simplifies to

$$\mathrm{R}[S(f_1), S(f_2)] = \frac{\int_{-\infty}^{\infty} \frac{\tau^2}{[1+(2\pi f_1 \tau)^2] \cdot [1+(2\pi f_2 \tau)^2]} f_\tau d\tau}{\sqrt{\int_{-\infty}^{\infty} \frac{\tau^2}{[1+(2\pi f_1 \tau)^2]^2} f_\tau d\tau \cdot \int_{-\infty}^{\infty} \frac{\tau^2}{[1+(2\pi f_2 \tau)^2]^2} f_\tau d\tau}} \,, \tag{7.11}$$

which can be solved to

$$\mathrm{R}[S(f_1), S(f_2)] = 2 \cdot \frac{\ln\left(\frac{f_1}{f_2}\right)}{(f_1^2 - f_2^2)} f_1 f_2 \,. \tag{7.12}$$

This result is particularly noteworthy because it is free of parameters; the shape of

R only depends on the spectra of the fundamental noise sources and their superposition. If, for instance, the observed $1/f$ noise would be the sum of microscopic $1/f$ noise sources with a perfect slope of -1, R would be equal to 1 for all Δf. Therefore, this correlation coefficient is a signature of the frequency dependence of the fundamental noise sources constituting the $1/f$ noise.

Equation (7.12) can be written in terms of $\Delta f'$, which is the ratio between f_1 and f_2, i.e. $\Delta f' = f_1/f_2$. In this case, (7.12) simplifies to

$$\mathrm{R}\left[S(f_1), S(f_2)\right] = 2 \cdot \frac{\ln\left(\Delta f'\right)}{\left(1-\Delta f'^2\right)} \cdot \Delta f' \ , \tag{7.13}$$

highlighting the fact that the shape of the correlation coefficient curve is independent of the reference frequency, f_{ref} when analysed in log-scale. Figure 7.1 depicts the correlation coefficient as a function of $\Delta f'$.

Figure 7.1: Correlation coefficient as a function of $\Delta f'$.

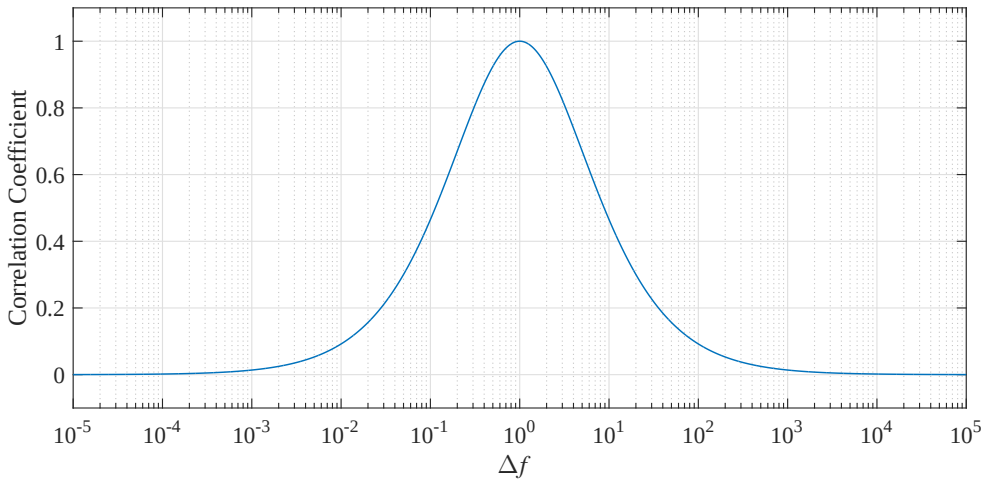

The correlation coefficient decreases as Δf increases. This means that for small frequency increments (small Δf), devices that have the higher noise levels at f_{ref} are more likely to have the higher noise levels at $f_{ref} + \Delta f$. Conversely, for large frequency increments (large Δf), as the correlation coefficient approaches zero, it is not possible to predict which devices have the higher noise levels at $f_{ref} + \Delta f$ based on their levels at f_{ref}.

The bell-like shape of the correlation coefficient curve is directly related to the frequency dependence of the fundamental noise sources underlying the LFN.

7.2.2 Experimental Results

Using equation (7.5), the correlation coefficient as a function of frequency was extracted for several N- and PFET populations from different technology nodes. In this section, the extracted correlation coefficient is compared to that obtained analytically, (7.12), and the results are discussed.

For small-area devices, the impact of individual traps is more significant, resulting in prominent lumps in the spectrum due to the Lorentzian-like PSD of a single trap. For these devices, however, telegraphic signals are usually visible in time domain measurements; therefore, there is usually consensus that RTS is the dominant noise mechanism in small-area devices. Figure 7.2 displays the LFN PSD of several small-area NFETs, highlighting Lorentzian-like spectra. For large-area devices as well as for PFETs, on the other hand, the primary mechanism underlying the LFN is debated (HAARTMAN; ÖSTLING, 2007; VANDAMME; HOOGE, 2008). While Lorentzian-like spectra may not be clearly visible, in the previous section it was shown that, if RTS is the primary mechanism underlying the LFN in MOSFETs, then experimental data should satisfy (7.12). The findings for 40-nm, 65-nm and 140-nm technologies are reported.

Following (7.12), the correlation coefficient is independent of the trap impact (ΔI_D). One should note, however, that the LFN distribution deviates from the log-normal distribution under high drain bias, as shown in section 6.1. Thus, in order to avoid distortions due to these deviations, comparisons are made, preferably, under low drain bias (uniformly charge channel condition).

Figure 7.2: LFN spectra of 320 small-area devices and highlighted Lorentzian-like spectra.

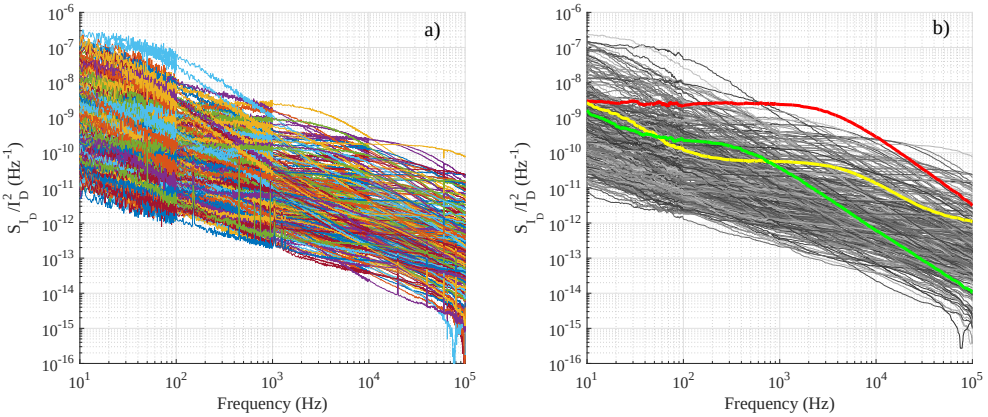

Figure 7.3: a) LFN spectra of a 320-DUT small-area NFET population (40-nm technology); and b) extracted (blue markers) versus theoretically calculated (red line) correlation coefficients. Transistor dimensions are W=0.3 μm and L=0.04 μm; bias conditions are V_{GS} = 1.1 V and V_{DS} = 0.1 V.

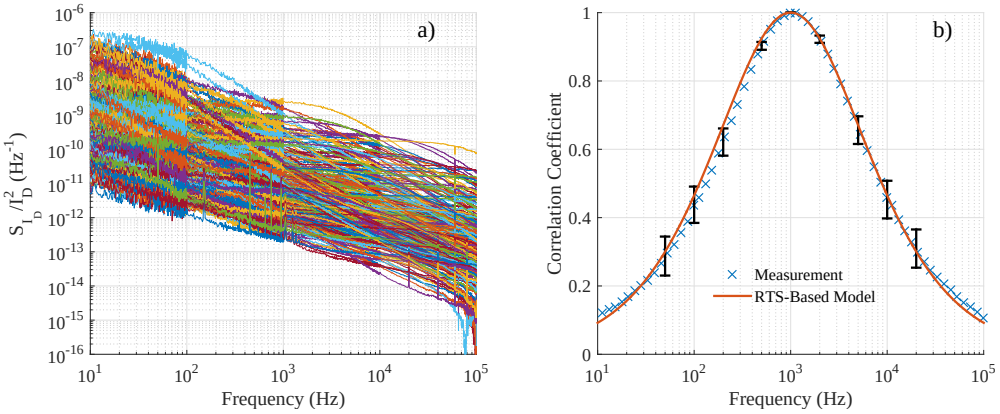

7.2.2.1 40-nm Technology

The population presented in Figure 7.2 has prominent Lorentzian-like spectra, indicating that RTS is indeed the primary cause of LFN. The comparison between extracted and calculated correlation coefficient is shown in Figure 7.3. As expected, (7.12) provides an accurate prediction of the dependence of the correlation coefficient with frequency, indicating, from an statistical perspective, that the RTS is the dominating noise mechanism in this population. For a similar small-area NFET population (albeit fewer samples), shown in Figure 7.4, the theoretically calculated correlation coefficient also gives a reasonable prediction of the measured correlation coefficient.

Figure 7.4: a) LFN spectra of a 60-DUT small-area NFET population (40-nm technology); and b) extracted (blue markers) versus theoretically calculated (red line) correlation coefficients. Transistor dimensions are W=1 μm and L=0.04 μm; bias conditions are V_{GS} = 0.9 V and V_{DS} = 0.05 V.

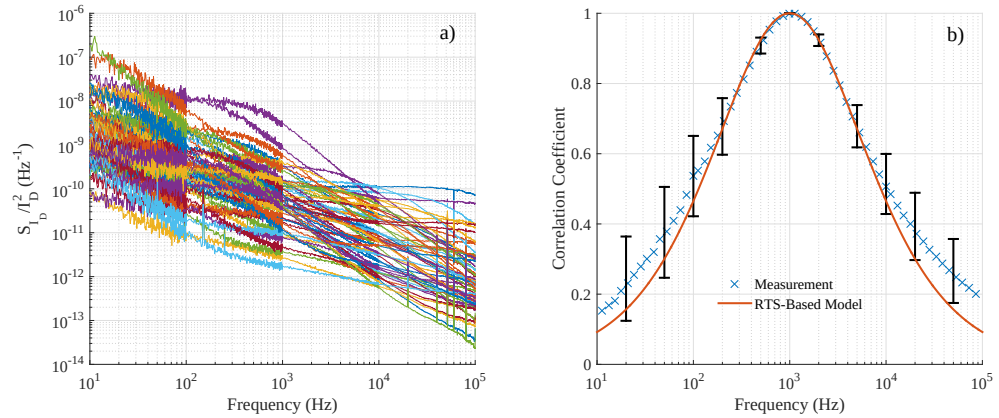

Figure 7.5: a) LFN spectra of a 60-DUT small-area PFET population (40-nm technology); and b) extracted (blue markers) versus theoretically calculated (red line) correlation coefficients. Transistor dimensions are W=0.3 μm and L=0.04 μm; bias conditions are V_{GS} = 0.7 V and V_{DS} = 0.05 V.

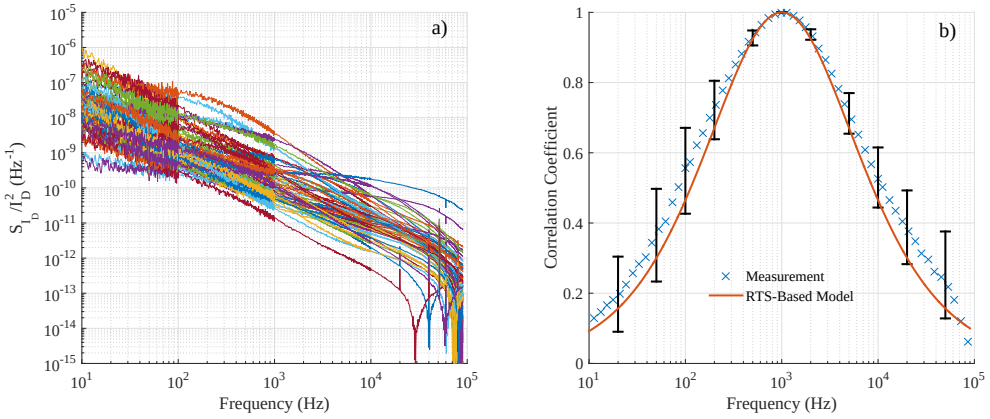

Interestingly, when a PFET population is analysed (Figure 7.5), Lorentzian-like spectra are also visible. Despite the reduced number of prominent lumps, the measured correlation coefficient is also well predicted by the model. This is a strong indication that the primary LFN mechanism in PFETs is the capture and emission of charge carriers.

Figure 7.6: a) LFN spectra of a 60-DUT large-area NFET population (40-nm technology); and b) extracted (blue markers) versus theoretically calculated (red line) correlation coefficients. Transistor dimensions are W=16 μm and L=0.2 μm; bias conditions are V_{GS} = 1.1 V and V_{DS} = 0.05 V.

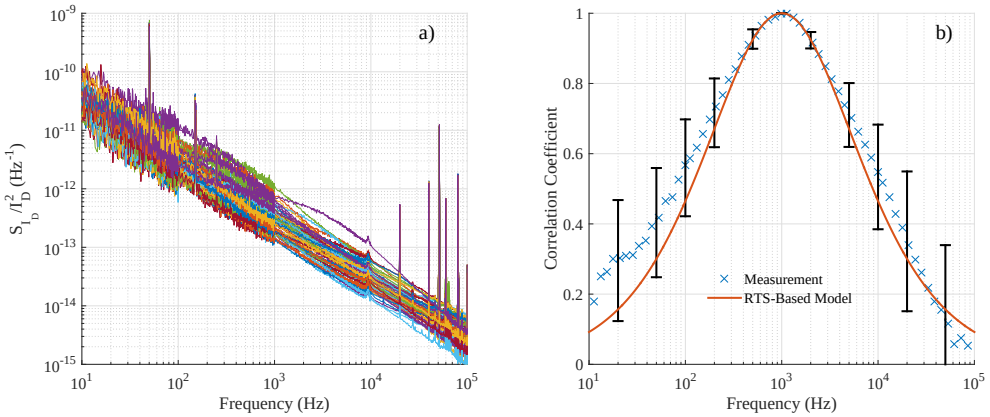

For large-area devices (Figures 7.6 and 7.7), Lorentzian-like spectra are hardly visible for both N- and PFET populations. The correlation coefficient, however, follows the RTS-predicted behaviour. This is a strong indication that the $1/f$ noise in large-area devices is composed by a superposition of Lorentzians, similarly to small-area devices. Notice that the de-correlation with increasing Δf means that the spectra do not have a constant slope; they intertwine at a certain rate which is well described by the RTS model.

Figure 7.7: a) LFN spectra of a 60-DUT large-area PFET population (40-nm technology); and b) extracted (blue markers) versus theoretically calculated (red line) correlation coefficients. Transistor dimensions are W=16 μm and L=0.2 μm; bias conditions are V_{GS} = 1.1 V and V_{DS} = 0.05 V.

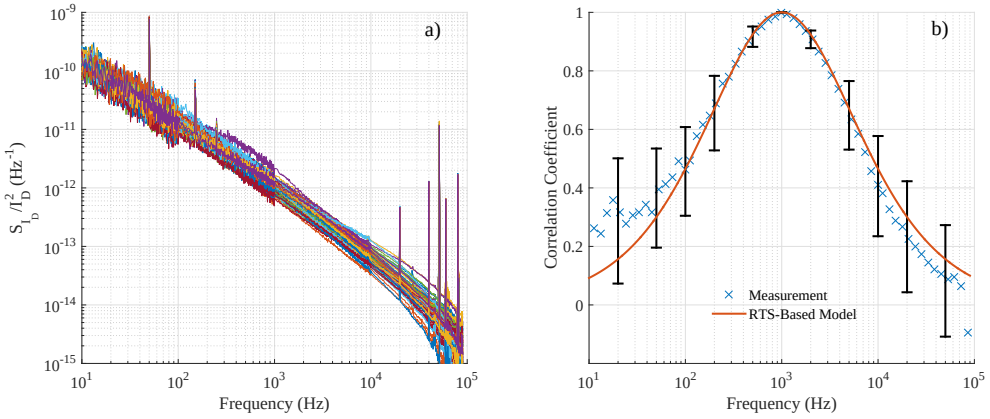

7.2.2.2 65-nm Technology

Since the correlation coefficient is independent of transistors parameters and technology process, different technology processes should yield similar results. For the small-area NFET population shown in Figure 7.8, Lorentzian-like spectra are clearly visible. As expected, the correlation coefficient is accurately predicted by the RTS-based model, despite the larger drain voltage when compared to that used for the 40-nm technology.

Figure 7.8: a) LFN spectra of a 282-DUT small-area NFET population (65-nm technology); and b) extracted (blue markers) versus theoretically calculated (red line) correlation coefficients. Transistor dimensions are W=1 μm and L=0.06 μm; bias conditions are V_{GS} = 1.2 V and V_{DS} = 0.5 V.

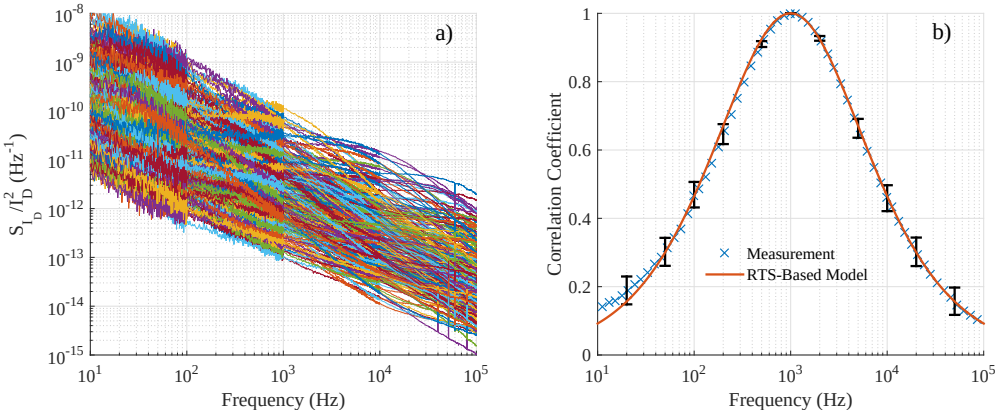

For a large-area NFET population (Figure 7.9), the extracted correlation coefficient also indicates that a superposition of Lorentzians is the primary source of LFN, despite the small number of visible lumps. Notice that, for this population, measurements

above 10 kHz are unreliable due to the noise level being close or below the measurement noise floor.

Figure 7.9: a) LFN spectra of a 282-DUT large-area NFET population (65-nm technology); and b) extracted (blue markers) versus theoretically calculated (red line) correlation coefficients. Transistor dimensions are W=10 μm and L=10 μm; bias conditions are V_{GS} = 1.2 V and V_{DS} = 0.5 V.

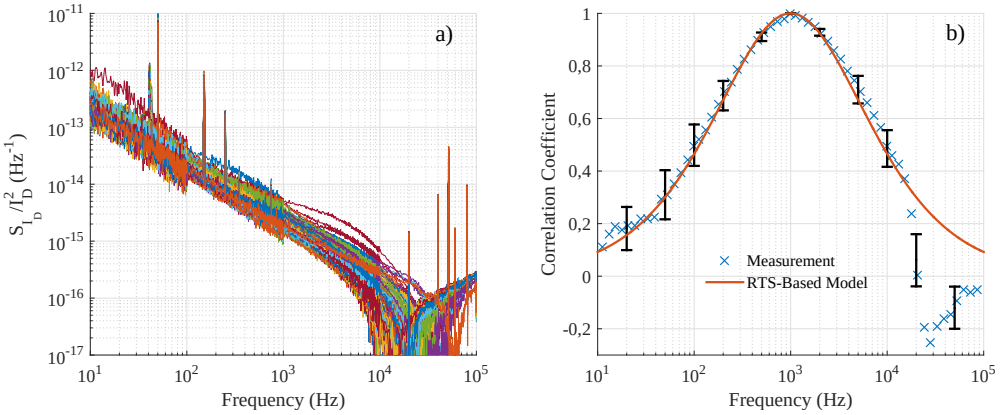

7.2.2.3 140-nm Technology

Similarly to the results obtained for the previous technologies, both small-area N- and PFET populations display Lorentzian-like spectra (Figures 7.10 and 7.11), indicating RTS-based LFN.

Figure 7.10: a) LFN spectra of a 43-DUT small-area NFET population (140-nm technology); and b) extracted (blue markers) versus theoretically calculated (red line) correlation coefficients. Transistor dimensions are W=0.232 μm and L=0.336 μm; bias conditions are V_{GS} = 1.0 V and V_{DS} = 0.1 V.

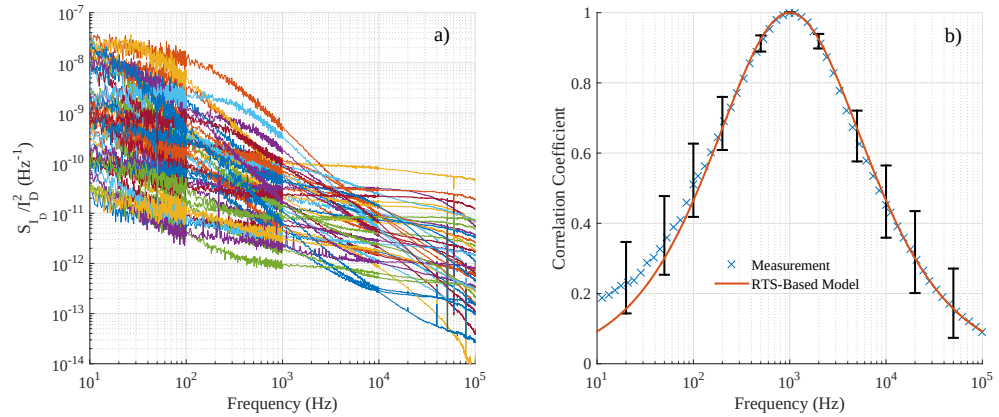

For the large-area devices (7.12 and 7.13), while the spectra are approximately $1/f$, i.e. lumps are not visible in the spectra, the correlation coefficient follows the be-

Figure 7.11: a) LFN spectra of a 43-DUT small-area PFET population (140-nm technology); and b) extracted (blue markers) versus theoretically calculated (red line) correlation coefficients. Transistor dimensions are W=0.232 μm and L=0.336 μm; bias conditions are V_{GS} = 1.8 V and V_{DS} = 0.1 V.

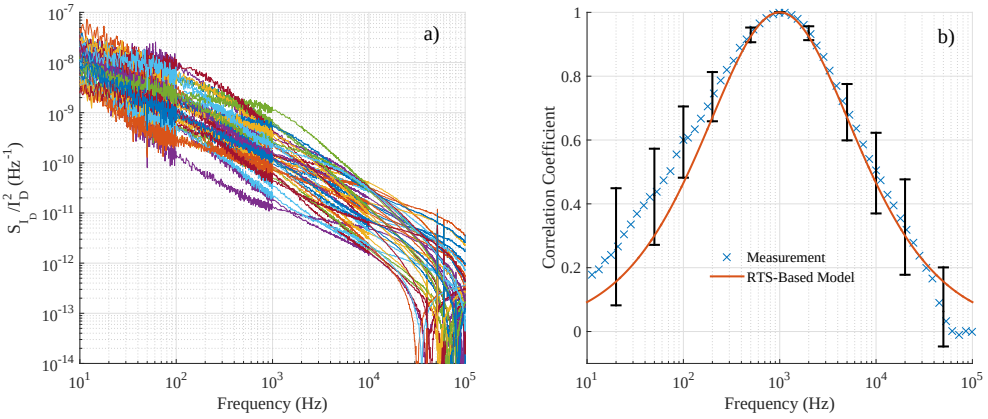

haviour predicted by the RTS-based model. This trend was observed for all measured technologies, reinforcing the idea that the $1/f$ noise is composed by a summation of Lorentzian-like spectra, regardless of device type and area.

Figure 7.12: a) LFN spectra of a 43-DUT large-area NFET population (140-nm technology); and b) extracted (blue markers) versus theoretically calculated (red line) correlation coefficients. Transistor dimensions are W=8 μm and L=1 μm; bias conditions are V_{GS} = 1.0 V and V_{DS} = 0.1 V.

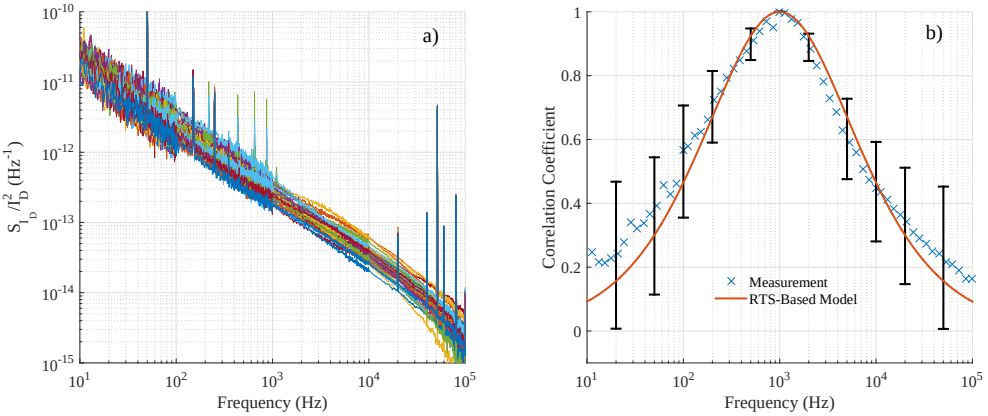

These results reinforce the validity of LFN models based on the summation of individual telegraphic signals resulting in a $1/f$ spectra. If there is a fundamental $1/f$ noise source underlying the LFN — from bulk mobility fluctuations, for instance —, its effects are overshadowed by the Lorentzian-like PSD of the multiple RTS, as observed by the autocorrelation coefficient analysis.

Figure 7.13: a) LFN spectra of a 43-DUT large-area PFET population (140-nm technology); and b) extracted (blue markers) versus theoretically calculated (red line) correlation coefficients. Transistor dimensions are W=8 μm and L=0.16 μm; bias conditions are V_{GS} = 1.8 V and V_{DS} = 0.1 V.

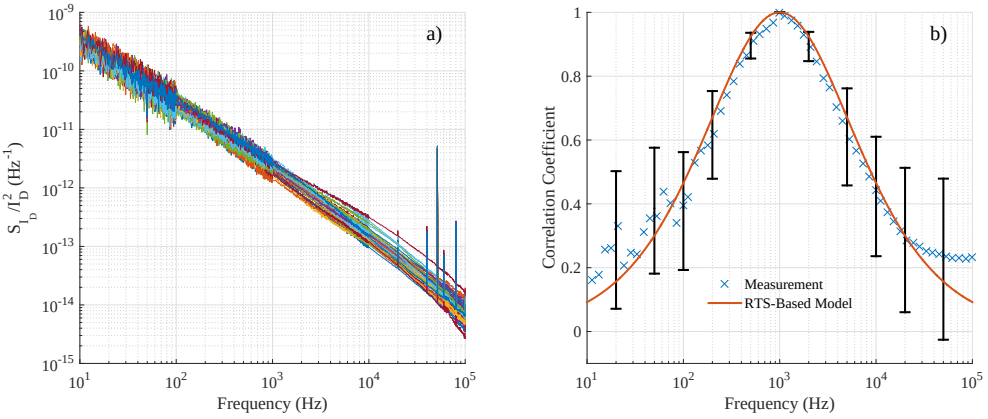

7.3 Temperature Autocorrelation

The autocorrelation can also be analysed in terms of temperature shifts. Even though $1/f$ noise is known for being weakly temperature dependent, the sensitivity of the autocorrelation technique proves useful to draw conclusions regarding the temperature dependence of the characteristic time constant of the traps.

Three different trapping models were considered for comparison. The first is the direct-tunnelling model (MCWHORTER, 1957), in which

$$\tau = \tau_o \cdot \exp(\gamma z) \ , \tag{7.14}$$

with z and γ being the trap depth in the oxide, and the wave function attenuation factor, respectively. In this model, τ is unaffected by temperature shifts, causing the PSD distribution to be strongly correlated to itself, regardless of ΔT. This assumptions hold true if the Fermi energy is weakly affected by the temperature shifts, which is reasonable for strong inversion.

The second model introduces thermal activation (DUTTA; HORN, 1981; SURYA; HSIANG, 1988) using

$$\tau = \tau_o \cdot \exp\left(\frac{E_B}{kT}\right) \ , \tag{7.15}$$

where E_B is an activation energy. In this model, increasing temperature reduces τ, shifting the entire LFN PSD towards higher frequencies, causing de-correlation at f_{ref}. Notice that for a wide spread of activation energies, this shift means the number of traps in a given

interval of time constants increases.

The third model is the Kirton and Uren model (KIRTON; UREN, 1989). It combines tunnelling and thermal activation, and is given by

$$\tau = \frac{1}{n v_{th} \sigma_0} \cdot \exp\left(\gamma z + \frac{E_B}{kT}\right) \cdot \frac{\beta}{1+\beta}\,, \tag{7.16}$$

where n, v_{th}, and σ_0 are the carrier concentration, thermal velocity and capture cross-section pre-factor, respectively. For all models, z and E_B were assumed uniformly distributed. As observed by (KIRTON; UREN, 1989; VANDAMME; HOOGE, 2008), (7.16) does not produce a log-uniformly distributed random variable for E_B and z uniform, though the resulting PSD is approximately $1/f$.

Figure 7.14 shows the measured correlation coefficient between different temperatures for two NFET populations. The theoretical correlation coefficient was calculated numerically using the three models introduced above.

Figure 7.14: Correlation coefficient as a function of temperature (T_{ref} = 25 °C) at 100 Hz for a) two independent 80-DUT NFET populations ($1 \times 0.04\ \mu m^2$) and b) two independent 78-DUT NFET populations ($1 \times 1\ \mu m^2$). The first population of each geometry was measured at -25 °C, 0 °C, and 25 °C; whereas the second was measured at 25 °C, 50 °C and, 75 °C. All populations were measured on the same wafer.

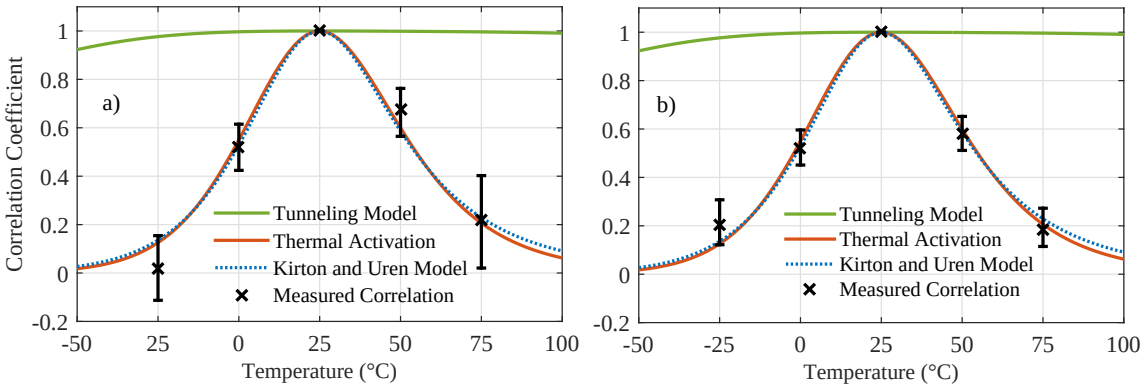

The decorrelation observed in Figure 7.14 with increasing ΔT indicates that, at the reference frequency (100 Hz), different traps are responsible for the LFN PSD at different temperatures. Two explanations are possible for the observed behaviour, however. The first, previously discussed, is that the characteristic time constant of the traps is temperature dependent; in this case, with increasing temperature traps become faster, causing the entire noise PSD to shift towards higher frequencies. The second is the case in which different traps are active altogether when temperature is modified, causing the LFN spectrum

to change its shape entirely with temperature.

While the analysis in Figure 7.14 is not sufficient to clarify on the matter, a combined temperature and frequency correlation analysis, presented in the following section, provides an answer to this question.

7.4 Temperature and Frequency Correlation

In the previous section it was established that temperature shifts cause the de-correlation of the LFN PSD at a given frequency, even though it was not possible to determine whether the temperature affects the occupation probability of the traps (i.e. the β parameter) or the characteristic time constant of the traps (τ). If the first assumption is true — that is the β parameters is responsible for the observed de-correlation with ΔT — then different traps are responsible for the noise PSD at different temperatures, meaning the correlation would drop at all frequencies with increasing temperature. On the other hand, if the second assumption is true — τ is thermally activated — then the same traps would be responsible for the noise PSD at a different temperature; however, their influence would be shifted in frequency.

While the findings of Dutta and Horn (1981) as well as the analysis of individual Lorentzians presented in Section 6.5 point towards a thermally activated τ, these techniques are inadequate for a statistical analysis. The first — the Dutta and Horn identity — requires several temperature measurements (thus, is suitable for individual devices), while the second — the analysis of individual Lorentzians — requires identification of PSD profiles that are not present in large area devices. Conveniently, if the correlation technique presented in this work is applied to the measured data, combining both temperature and frequency correlations. ($\mathrm{R}\left[S_{I_D}(f_{ref},T_{ref}),S_{I_D}(f_{ref}+\Delta f,T_{ref}+\Delta T)\right]$), it is possible to statistically demonstrate that the time constants of the traps are thermally activated, for both small-area (in which Lorentzian profiles are visible) and large-area devices (in which the LFN PSD is approximately $1/f$).

Figures 7.15 and 7.16 display the extracted correlation coefficient as a function of frequency and temperature for a reference frequency of 1 kHz and a reference temperature of 25 ºC for two NFET populations from the same wafer (symbols). The prediction given by the theoretical model, calculated numerically using the Kirton and Uren model, is also presented (solid line). At $\Delta T = 0$ ºC the analysis is reduced to the frequency auto-correlation. Notice, however, that as ΔT increases the peak of the correlation coefficient

Figure 7.15: Correlation coefficient extracted from measured data (symbols) from two 80-DUT NFET, 40-nm technology, populations (A and B) from the same wafer. Each population was measured at three temperatures as shown in the legend. Device geometry is $W = 1\mu$m and $L = 0.04\mu$m; $T_{ref} = 25$ ºC and $f_{ref} = 1$ Hz; bias conditions were a) $V_{GS} = 1.1$ V, $V_{DS} = 0.1$ V and b) $V_{GS} = 0.7$ V, $V_{DS} = 0.5$ V. Solid lines indicate theoretical prediction.

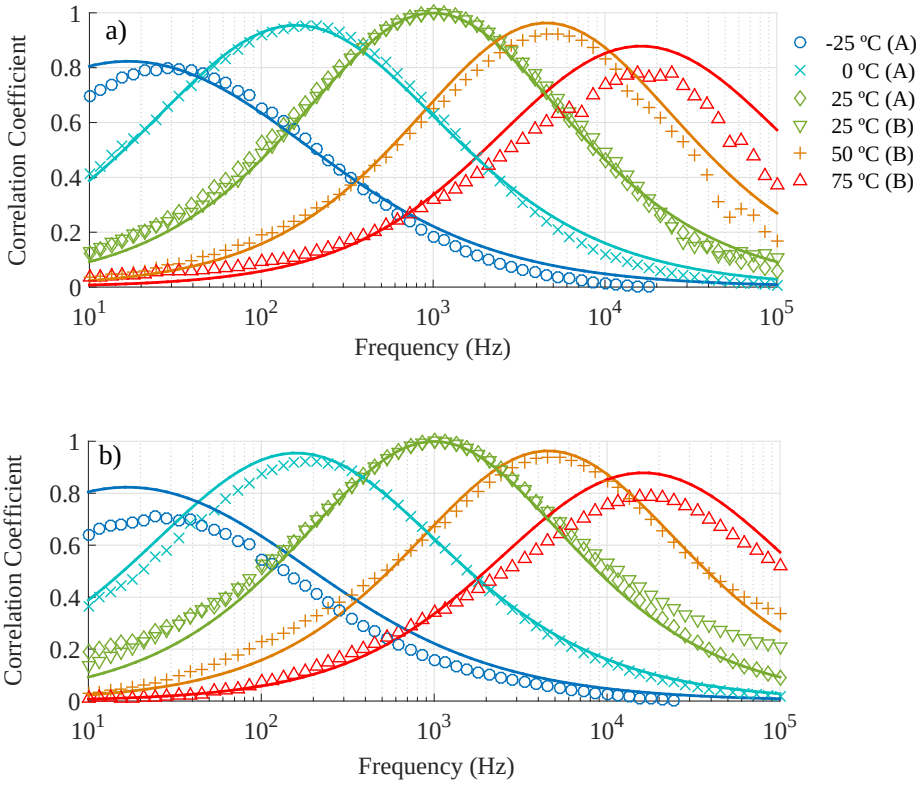

is shifted in frequency. This provides strong indication that the "shape" of the PSD is unaltered with temperature, but shifted in frequency; in other words, it is an indication that the same traps are active at different temperatures (i.e. their occupation probability, β is primarily unaffected with temperature), but their characteristic time, τ, is strongly temperature dependent. This is in line with the concept that τ decreases with increasing T. This is a well-known observation for RTS, but is now also revealed in the context of $1/f$ noise.

Despite the fact that the frequency-temperature autocorrelation follows the now-familiar bell shape, it does not fully reach 1 when $\Delta T > 0$, which indicates that the stochastic process underlying the LFN contains at least two independent stochastic components as is, e.g., the case for the Kirton and Uren model. Figure 7.17 illustrates the difference between the correlation coefficient estimation using thermal activation and using Kirton and Uren model.

Due to the complexity of measuring the same device several times (e.g. degradation of the pads), each population was split into two groups. The first, named group A,

was measured at -25 ºC, 0 ºC and 25 ºC; while the second, group B, was measured at 25 ºC, 50 ºC and 75 ºC.

Figure 7.16: Correlation coefficient extracted from measured data (symbols) from two 78-DUT NFET, 40-nm technology, populations (A and B) from the same wafer. Each population was measured at three temperatures as shown in the legend. Device geometry is $W = 1\mu$m and $L = 1\mu$m; $T_{ref} = 25$ ºC and $f_{ref} = 1$ Hz; bias conditions were a) $V_{GS} = 1.1$ V, $V_{DS} = 0.1$ V and b) $V_{GS} = 0.7$ V, $V_{DS} = 0.5$ V. Solid lines indicate theoretical prediction.

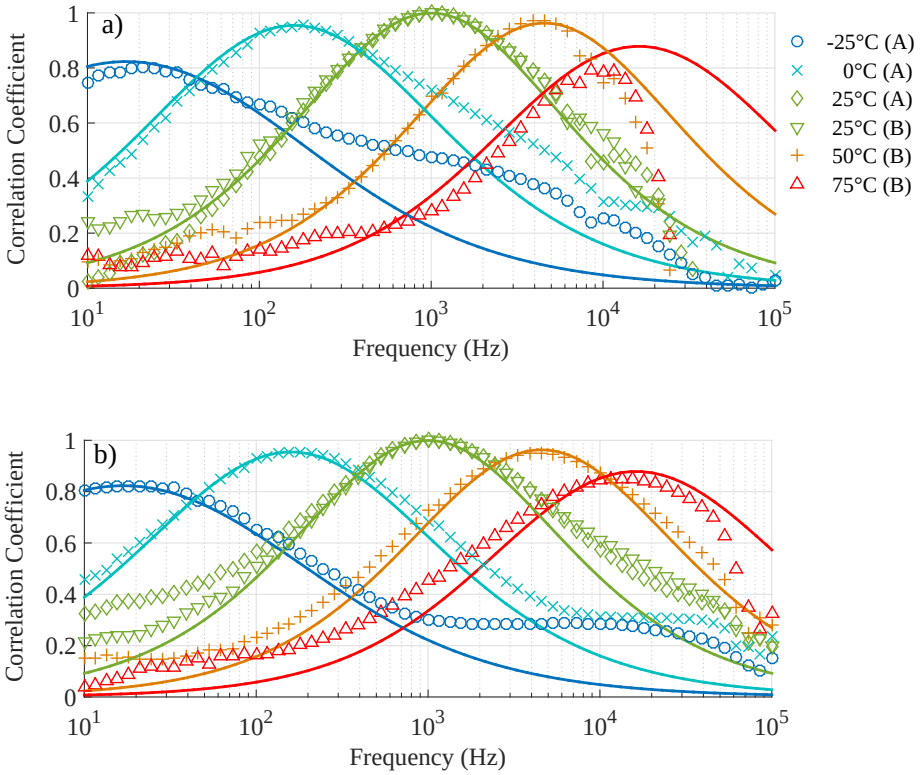

Figure 7.17: Estimated correlation coefficient using thermal activation (dashed lines) and the Kirton and Uren model (solid lines).

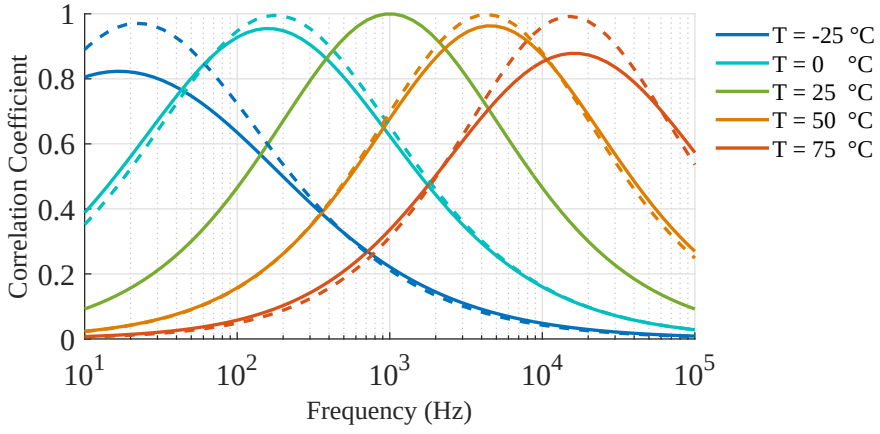

7.5 Gate Voltage Autocorrelation

The proposed technique can also be applied to study the gate voltage dependence of the LFN PSD. From the RTS and bias temperature instability (BTI) framework, the capture and emission time constants are expected to be strongly gate bias dependent. Therefore, the β parameter (the ratio between capture and emission time constants), which describes how much a given trap contributes to noise power (maximum contribution when $\tau_c = \tau_e$), should also be gate bias dependent. Simply put, given that $\beta = \tau_e/\tau_c = \exp[(E_T - E_F)/kT]$, if the trap energy, E_T, is close to the Fermi energy, E_F, then $\tau_c \approx \tau_e$, causing the trap to switch often, in which case the trap contributes significantly to noise power. Thus, since E_F varies with gate bias, different traps are expected to contribute to noise power at different gate biases. In order to demonstrate that shifts in gate bias indeed have a profound effect on the contribution of a single trap to noise power, as predicted by the RTS model, the frequency and gate bias autocorrelations are analysed in tandem (R$[S_{I_D}(f_{ref}, V_{GS,ref}), S_{I_D}(f_{ref} + \Delta f, V_{GS,ref} + \Delta V_{GS})]$).

In figures 7.18 and 7.19, the correlation coefficient as a function of frequency and gate bias was extracted for two NFET and two PFET 60-DUT, 40-nm technology, populations, respectively. The significant drop in the correlation with increasing ΔV_{GS} demonstrates that there is a strong dependence of β with V_{GS}. It is important to notice that, contrary to the temperature and frequency autocorrelation, there is no clear shift in the peak of the correlation coefficient, indicating the β parameter was more significantly affected than τ (i.e. traps did not become overall faster of slower with increasing ΔV_{GS}; their overall contribution to noise power was modified with increasing ΔV_{GS}).

Figure 7.18: Extracted correlation coefficient as a function of frequency and gate bias for two 60-DUT NFET populations (40-nm technology). The reference gate bias is 0.9 V and drain bias is 50 mV.

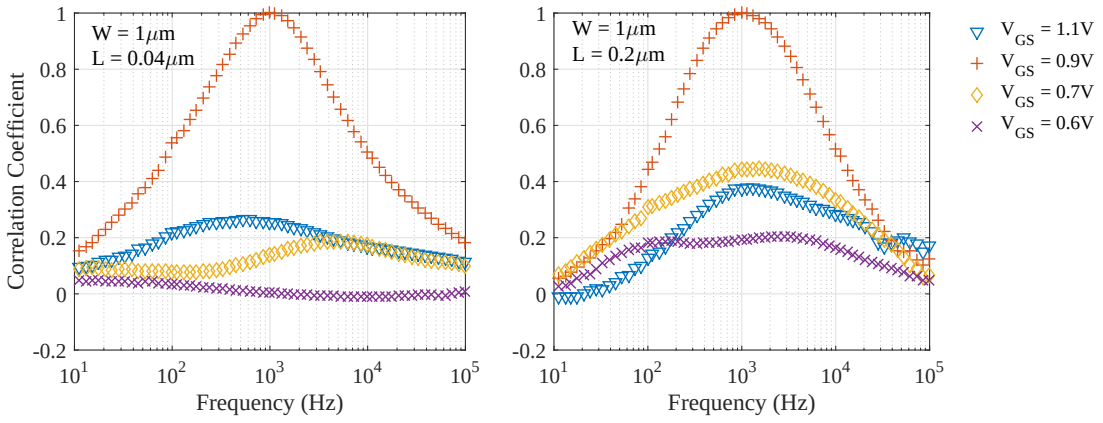

Figure 7.19: Extracted correlation coefficient as a function of frequency and gate bias for two 60-DUT PFET populations (40-nm technology). The reference gate bias is 0.9 V and drain bias is 50 mV.

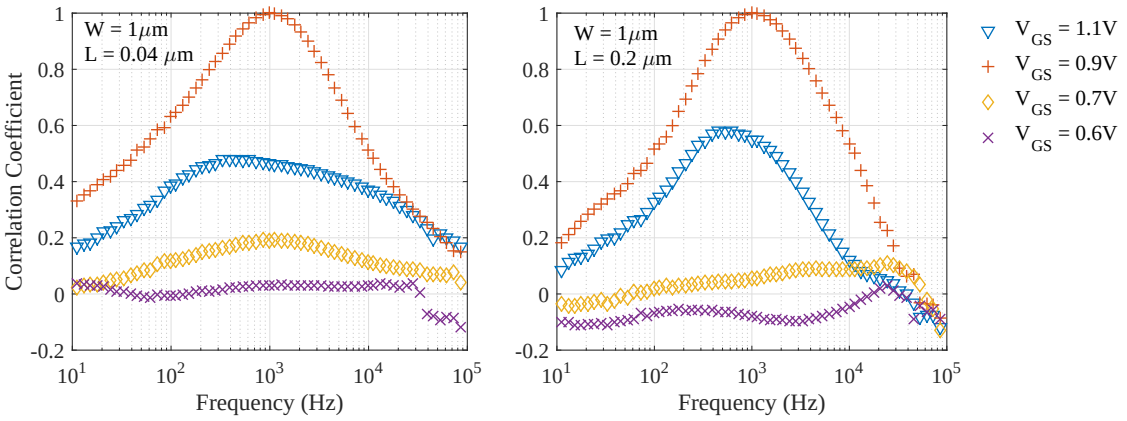

Notice, however, the observed de-correlation with ΔV_{GS} may be attributed to E_T or E_F; that is, not only may E_F depend on gate voltage, but also E_T. Typically, if traps are assumed to be located at the oxide/semiconductor interface, then E_T is constant, with only E_F bias dependent. If, on the other hand, the trap is assumed to be at a certain depth within the oxide, then E_T and E_F are both bias dependent. The dependence of E_T on the electric field across the oxide is given by

$$E_T = E_{T0} + qz_{tr}E_{ox} \tag{7.17}$$

where E_{T0} and z_{tr} are the trap energy in flat band conditions and trap depth, respectively; and the electric field, E_{ox}, is given by

$$E_{ox} = \frac{1}{T_{ox}}\left(V_{GB} - V_{FB} - \phi_s\right) \tag{7.18}$$

where V_{GB}, V_{FB}, ϕ_s and T_{ox} are the gate to substrate voltage, flat band voltage, surface potential and gate oxide thickness, respectively. The impact of trap depth on the bias dependence of the trap energy is illustrated in Figure 7.20, in which the transition from weak to strong inversion ($\Delta V_{GS,1}$) and the application of an additional voltage in strong inversion ($\Delta V_{GS,2}$) are shown.

In the first case, notice that both $E_F - E_v$ and E_{ox} increase with $\Delta V_{GB,1}$, causing the trap to shift from well above E_F to slightly below E_F. In the second case, however, further increases in V_{GB} barely affect E_F, primarily increasing E_{ox}. If the trap were located at the semiconductor/oxide interface, then ΔE_T would be equal to zero. Due to the trap depth however, $\Delta V_{GB,2}$ causes the trap to shift from slightly below E_F to deeply below E_F.

Figure 7.20: MOS capacitor energy band diagram for three different gate bias conditions ($V_{blue} < V_{red} < V_{green}$).

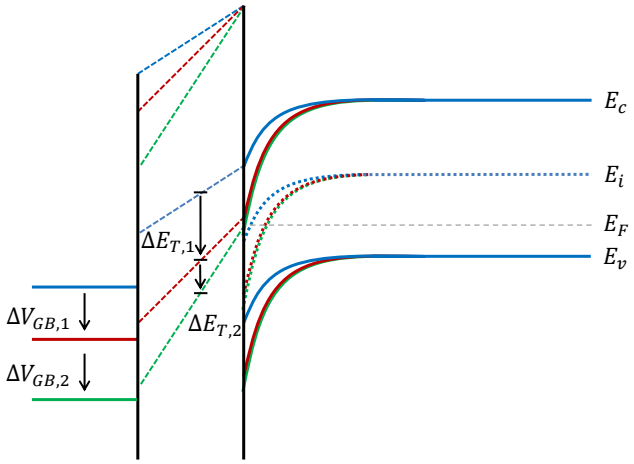

Consequently, if traps are located inside the oxide and not at the semiconductor/oxide interface, increasing ΔV_{GS} may cause significant de-correlation even if E_F remains roughly constant.

Figure 7.21 displays the estimated correlation coefficient from a generic device ($V_T \approx 0.65V$), using the Monte Carlo simulation tool, assuming traps are located at the interface and 0.5 nm inside the gate oxide. The comparison between measured and simulated results indicate that, on average, traps are not located at the interface, but rather inside the oxide, so that E_T is also bias dependent. One should be aware, however, that

Figure 7.21: Estimated correlation coefficient versus frequency for different gate voltages applied using Monte Carlo simulation. Solid black line is the frequency correlation at the reference gate voltage (0.9 V). Solid lines (blue and red) are the estimated correlation coefficient assuming traps are located at the interface for 0.7 V and 1.1 V, respectively; dashed lines (blue and red) are assuming traps are located approximately 0.5 nm inside the gate oxide for 0.7 and 1.1 V, respectively.

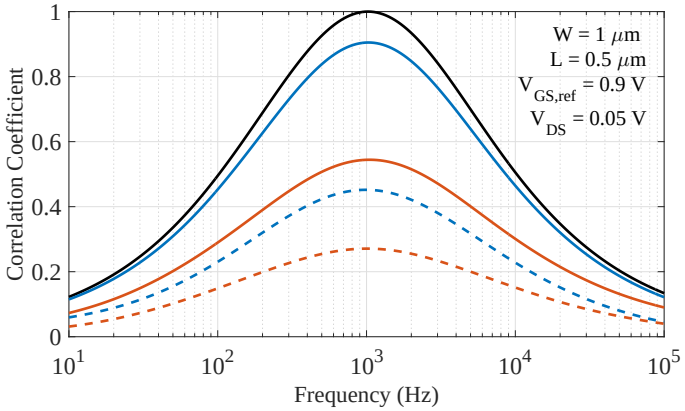

the estimation of the Fermi energy through basic semiconductor equations may not be adequate for sub-micrometer devices. Therefore, in order to properly estimate the average trap depth using the proposed technique, additional analyses, supported by TCAD simulations, are required for future studies.

7.6 Drain and Source Swap

Another interesting analysis is presented in Figure 7.22, in which the LFN PSD of a population of thick gate oxide PFETs is measured twice, swapping the drain and source terminals. Due to the symmetry of the MOSFET, the average value and the variance of the noise are similar regardless of which terminal is taken as drain or source. The correlation coefficient, however, is strongly dependent on the region of operation of the device. This is a consequence of the trap impact dependence on the position along the channel. Following number fluctuation solely,

$$\mathrm{E}\left[\Delta\widetilde{I_D}(x_{tr})\right] = \frac{1}{N(x_{tr}) + (k_B T/q^2)\,(C_{ox} + C_D + C_{it})}\,, \tag{7.19}$$

where $N(x_t)$ is the surface carrier density at position x_{tr}.

Figure 7.22: Correlation coefficient of the LFN PSD at 20 Hz as a function of gate voltage for a 68-DUT PFET population measured swapping the drain and source terminals (solid blue dots). Black dashed line obtained through Monte Carlo simulation of 5,000 devices. The threshold voltage of the devices is approximately 0.5 V.

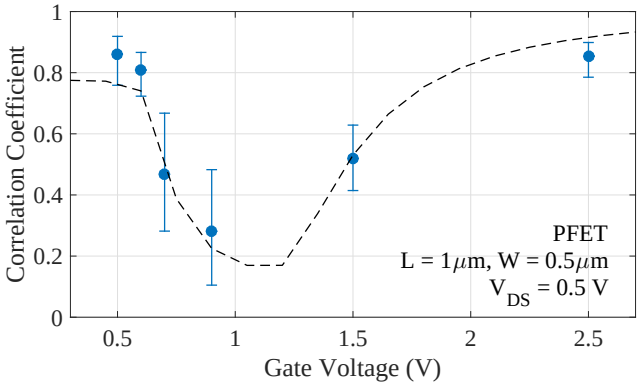

In weak inversion, the channel is not yet formed; due to the low surface carrier density, the trap impact is dominated by the oxide capacitance, which is position independent. Therefore, correlation coefficient is high, given that the impact of a trap is independent of its position along the channel.

As gate voltage increases, the channel is formed; however, given that $V_{DS} > V_{GS} -$

V_T the device operates in saturation region. In this region, the surface carrier concentration varies along the channel, thus the trap impact becomes position dependent. Traps near the pinch-off region become more prominent due to the lower surface carrier density, a effect which is enhanced by the pocket (halo) implants, availing to the observed drop in correlation.

Further increasing the gate voltage causes the device to operate in linear region ($V_{DS} < V_{GS} - V_T$), causing the surface carrier concentration to become approximately constant along the channel for sufficiently high gate voltages. The trap impact becomes again position independent, and, therefore the correlation coefficient increases.

For the Monte Carlo simulation presented in Figure 7.22, the surface carrier density, required in (7.19), was obtained through numerical solution of the 1-d Poisson equation of the MOSFET. The trap impact as a function of position for three different gate voltages are presented in Figure 7.23. As expected, in subthreshold and linear region, $V_{GS} = 0.45$ V and $V_{GS} = 2.4$ V, respectively, $\mathrm{E}\left[\Delta\widetilde{I_D}(x_{tr})\right]$ is approximately constant, and can be approximated by $q^2/(k_B T C_{ox})$ and $1/N$, respectively. On the other hand, when $V_{GS} - V_T \approx V_{DS}$, $\mathrm{E}\left[\Delta\widetilde{I_D}(x_{tr})\right]$ is strongly position dependent, since the surface carrier concentration, N, is also position dependent. It is important to observe that the purpose of the Monte Carlo simulation is to provide the qualitative behaviour of the correlation coefficient across multiple gate voltages for a generic device population. This means that the simulation was not parametrized to represent the measured 65-nm technology (with the exception of the threshold voltage).

Figure 7.23: Average trap impact as a function of trap position for three different gate voltages.

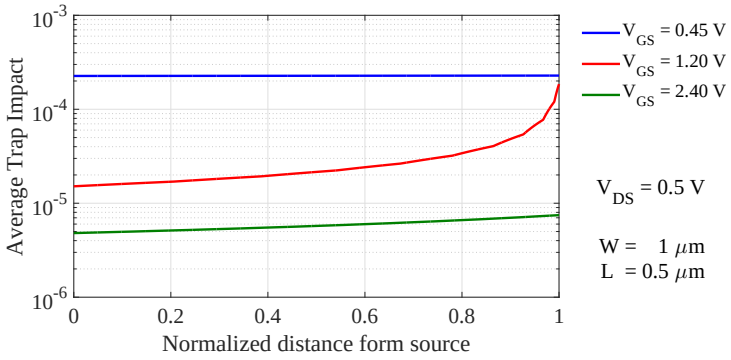

The trap impact as a function of channel position for different device geometries and biases was more deeply explored through TCAD simulation by Banaszeski da Silva et al. (2016), accounting for non-uniform channel doping.

7.7 Summary and Discussions

The correlation coefficient methodology developed and presented in this chapter provided strong indication that the low-frequency noise in the analysed CMOS technologies is primarily composed by a superposition of Lorentzians, reinforcing trapping/de-trapping noise models. No evidence was found to support bulk mobility fluctuations in these devices. Moreover, it was demonstrated that the characteristic time constant of these Lorentzians is temperature dependent, in line with a thermally activated process, as proposed by Dutta and Horn (1981), Surya and Hsiang (1988), and Kirton and Uren (1989).

Additionally, the results indicate that the gate bias primarily affects the occupation probability of the traps — i.e. the ratio between capture and emission time constants —, but not necessarily their characteristic time constants. Also, the observed de-correlation when gate bias is varied in strong inversion indicates that traps are located within the oxide rather than at the oxide/semiconductor interface.

Finally, by swapping the source and drain terminals, it was demonstrated that trap impact is strongly position dependent when the device is operated in saturation, which must be accounted for in LFN models. This is particularly important for modern CMOS technologies due to channel engineering. Pocket implants, for instance, may enhance trap impact, causing both the expected value and the variance of the LFN to significantly increase, as demonstrated by Banaszeski da Silva et al. (2016).

8 FINAL REMARKS

In this work, a new technique for low-frequency noise analysis has been proposed, in which autocorrelations between LFN spectra at different frequencies, biases, and temperatures are investigated. The strength of the method lies in the fact that different physical models yield significantly different predictions for these autocorrelations. Additionally, being a statistical method, it captures the dominant behaviour of the entire population, despite the subtleties of individual devices.

An analytical model for the correlation coefficient as a function of frequency was derived from the RTS-based framework and compared to extracted correlation coefficient from measured data from three different CMOS mixed-signal technologies. The comparison reinforced that the $1/f$ noise in MOSFETs is composed by a summation of Lorentzians.

The temperature dependence of the LFN was also evaluated using the autocorrelation technique; the extracted correlation coefficient as a function of frequency and temperature was compared to a RTS-based numerical model. The results provided a strong case for predominantly thermally activated time constants for the trapping process, in accordance with the temperature dependence observed by Surya and Hsiang (1988) and Kirton and Uren (1989), which should be accounted for in compact LFN models.

A similar analysis was conducted in terms of the gate bias, which indicated that, while gate bias has no noticeable impact on the characteristic time constant, it significantly affects trap occupancy, i.e. which traps contribute more significantly to noise at a given condition. Monte Carlo simulations were employed to evaluate the impact of trap depth within the oxide on the correlation coefficient, suggesting that traps might not be located at the interface.

Also, by swapping the drain and source contacts it was possible to observe that trap impact is significantly affected by trap position. Therefore, for accurate LFN modelling it is imperative to account for the non-uniform channel doping of modern MOSFET devices.

Overall, the measured data from three different commercial CMOS mixed-signal technologies provide strong support for an LFN model based on the sum of thermally activated random telegraph signals for all measured N-and PFETs, regardless of device area. No evidence supporting bulk mobility fluctuations was found.

The methodology presented in this work can be applied to study LFN in advanced CMOS technologies (such as FinFETs) and in other device structures (such as bipolar

junction transistors). These analysis avail the understanding and quantification of the physical mechanisms underlying LFN in new devices and materials.

REFERENCES

ARNAUD, A.; GALUP-MONTORO, C. A compact model for flicker noise in mos transistors for analog circuit design. **IEEE Transactions on Electron Devices**, v. 50, n. 8, p. 1815–1818, Aug 2003.

ARNAUD, A.; GALUP-MONTORO, C. Consistent noise models for analysis and design of cmos circuits. **IEEE Transactions on Circuits and Systems I: Regular Papers**, v. 51, n. 10, p. 1909–1915, Oct 2004.

ASENOV, A. et al. Rts amplitudes in decananometer mosfets: 3-d simulation study. **IEEE Transactions on Electron Devices**, v. 50, n. 3, p. 839–845, March 2003.

BAK, P.; TANG, C.; WIESENFELD, K. Self-organized criticality: An explanation of the 1/f noise. **Physical review letters**, APS, v. 59, n. 4, p. 381, 1987.

BANASZESKI DA SILVA, M. et al. A physics-based RTN variability model for MOSFETs. In: **2014 IEEE International Electron Devices Meeting**. [S.l.: s.n.], 2014. p. 35.2.1–35.2.4.

BANASZESKI DA SILVA, M. et al. A Physics-Based Statistical RTN Model for the Low Frequency Noise in MOSFETs. **IEEE Transactions on Electron Devices**, v. 63, n. 9, p. 3683–3692, Sept 2016.

BARTLETT, M. S. Periodogram analysis and continuous spectra. **Biometrika**, [Oxford University Press, Biometrika Trust], v. 37, n. 1/2, p. 1–16, 1950. ISSN 00063444. Disponível em: <http://www.jstor.org/stable/2332141>.

BRUCCOLERI, F.; KLUMPERINK, E. A.; NAUTA, B. Wide-band cmos low-noise amplifier exploiting thermal noise canceling. **Solid-State Circuits, IEEE Journal of**, IEEE, v. 39, n. 2, p. 275–282, 2004.

CAMPBELL, J. et al. Random telegraph noise in highly scaled nmosfets. In: **Reliability Physics Symposium, 2009 IEEE International**. [S.l.: s.n.], 2009. p. 382–388.

CARLSON, A. B.; CRILLY, P. B. **Communication systems. An introduction to signals and noise in electrical engineering**. [S.l.]: McGraw-Hill New York, 2010.

CHANG, J.; ABIDI, A. A.; VISWANATHAN, C. R. Flicker noise in cmos transistors from subthreshold to strong inversion at various temperatures. **IEEE Transactions on Electron Devices**, v. 41, n. 11, p. 1965–1971, Nov 1994.

COHEN, L. The history of noise on the 100th anniversary of its birth. **IEEE Signal Processing Magazine**, v. 22, n. 6, p. 20–45, Nov 2005.

DA SILVA, R.; WIRTH, G. I.; BRUSAMARELLO, L. An appropriate model for the noise power spectrum produced by traps at the si–sio 2 interface: a study of the influence of a time-dependent fermi level. **Journal of Statistical Mechanics: Theory and Experiment**, v. 2008, n. 10, p. P10015, 2008.

DING, Y. M.; MISRA, D.; SRINIVASAN, P. Bias temperature instability and its correlation to flicker (1/f) noise in finfets. In: **2016 IEEE International Integrated Reliability Workshop (IIRW)**. [S.l.: s.n.], 2016. p. 103–106.

DUNGA, M. et al. **BSIM4.6.0 MOSFET Manual**. Berkeley, USA, 2006.

DUTTA, P.; HORN, P. M. Low-requency fluctuations in solids: $1/f$ noise. **Rev. Mod. Phys.**, American Physical Society, v. 53, p. 497–516, Jul 1981.

EFRON, B. Bootstrap methods: Another look at the jackknife. **The Annals of Statistics**, Institute of Mathematical Statistics, v. 7, n. 1, p. 1–26, 1979. ISSN 00905364.

GHIBAUDO, G. et al. Improved Analysis of Low Frequency Noise in Field-Effect MOS Transistors. **physica status solidi (a)**, v. 124, n. 2, p. 571–581, 1991.

GRASSER, T. et al. Switching oxide traps as the missing link between negative bias temperature instability and random telegraph noise. In: IEEE. **Electron Devices Meeting (IEDM), 2009 IEEE International**. [S.l.], 2009. p. 1–4.

HAARTMAN, M. V.; ÖSTLING, M. **Low-frequency noise in advanced MOS devices**. [S.l.]: Springer Science & Business Media, 2007.

HANDEL, P. H. Quantum approach to $1/f$ noise. **Phys. Rev. A**, American Physical Society, v. 22, p. 745–757, Aug 1980.

HANSEN, M. Achieving accurate on-wafer flicker noise measurements through 30 mhz. **Cascade Microtech, Inc., May**, 2009.

HAYKIN, S. S.; MOHER, M. **An introduction to analog and digital communications**. [S.l.]: Wiley New York, 2007. v. 1.

HOOGE, F. $1/f$ noise is no surface effect. **Physics Letters A**, v. 29, n. 3, p. 139 – 140, 1969. ISSN 0375-9601.

HOOGE, F.; VANDAMME, L. Lattice scattering causes $1/f$ noise. **Physics Letters A**, v. 66, n. 4, p. 315 – 316, 1978. ISSN 0375-9601.

HUNG, K. et al. Random telegraph noise of deep-submicrometer mosfets. **IEEE electron device letters**, v. 11, n. 2, p. 90–92, 1990.

HUNG, K. K. et al. A physics-based MOSFET noise model for circuit simulators. **IEEE Transactions on Electron Devices**, v. 37, n. 5, p. 1323–1333, May 1990.

HUNG, K. K. et al. A unified model for the flicker noise in metal-oxide-semiconductor field-effect transistors. **IEEE Transactions on Electron Devices**, v. 37, n. 3, p. 654–665, Mar 1990.

JENSEN, H. J.; CHRISTENSEN, K.; FOGEDBY, H. C. 1/f noise, distribution of lifetimes, and a pile of sand. **Phys. Rev. B**, American Physical Society, v. 40, p. 7425–7427, Oct 1989.

JINDAL, R. P.; VAN DER ZIEL, A. Model for mobility fluctuation 1/f noise. **Applied Physics Letters**, v. 38, n. 4, p. 290–291, 1981.

JOHNSON, J. B. Thermal Agitation of Electricity in Conductors. **Phys. Rev.**, American Physical Society, v. 32, p. 97–109, Jul 1928.

KESHNER, M. S. 1/f noise. **Proceedings of the IEEE**, v. 70, n. 3, p. 212–218, March 1982.

KIRTON, M.; UREN, M. Noise in solid-state microstructures: A new perspective on individual defects, interface states and low-frequency (1/f) noise. **Advances in Physics**, Taylor & Francis, v. 38, n. 4, p. 367–468, 1989.

LATHI, B. P.; DING, Z. **Modern Digital and Analog Communication Systems 3e Osece**. [S.l.]: Oxford university press, 2009.

LEE, J.-H. et al. $1/f$ noise characteristics of sub-100 nm MOS transistors. **JSTS: Journal of Semiconductor Technology and Science**, The Institute of Electronics Engineers of Korea, v. 6, n. 1, p. 38–42, 2006.

LUKYANCHIKOVA, N. et al. On the 1/f noise of triple-gate field-effect transistors with high-k gate dielectric. **Applied Physics Letters**, v. 95, n. 3, p. 032101, 2009.

MACHLUP, S. Noise in Semiconductors: Spectrum of a Two-Parameter Random Signal. **Journal of Applied Physics**, v. 25, n. 3, p. 341–343, 1954.

MAVREDAKIS, N.; ANTONOPOULOS, A.; BUCHER, M. Measurement and modelling of 1/f noise in 180 nm nmos and pmos devices. In: **Circuits and Systems for Communications (ECCSC), 2010 5th European Conference on**. [S.l.: s.n.], 2010. p. 86–89.

MAVREDAKIS, N. et al. Charge-based compact model for bias-dependent variability of 1/ f noise in mosfets. **IEEE Transactions on Electron Devices**, v. 63, n. 11, p. 4201–4208, Nov 2016.

MCWHORTER, A. 1/f noise and germanium surface properties. **Semiconductor surface physics**, Philadelphia, PA: Univ. Pennsylvania Press, p. 207–228, 1957.

NAGUMO, T. et al. Statistical characterization of trap position, energy, amplitude and time constants by rtn measurement of multiple individual traps. In: **Electron Devices Meeting (IEDM), 2010 IEEE International**. [S.l.: s.n.], 2010. p. 28.3.1–28.3.4.

NGAI, K. L. Unified theory of $1/f$ noise and dielectric response in condensed matter. **Phys. Rev. B**, American Physical Society, v. 22, p. 2066–2077, Aug 1980.

NYQUIST, H. Thermal Agitation of Electric Charge in Conductors. **Phys. Rev.**, American Physical Society, v. 32, p. 110–113, Jul 1928.

SAH, C.-T.; NOYCE, R.; SHOCKLEY, W. Carrier generation and recombination in p-n junctions and p-n junction characteristics. **Proceedings of the IRE**, v. 45, n. 9, p. 1228–1243, Sept 1957.

SCHOLTEN, A. J. et al. Noise modeling for RF CMOS circuit simulation. **IEEE Transactions on Electron Devices**, v. 50, n. 3, p. 618–632, March 2003.

SCHOTTKY, W. Über spontane stromschwankungen in verschiedenen elektrizitätsleitern. **Annalen der Physik**, WILEY-VCH Verlag, v. 362, n. 23, p. 541–567, 1918.

SILVA, R. da; WIRTH, G. I.; BREDERLOW, R. Novel analytical and numerical approach to modeling low-frequency noise in semiconductor devices. **Physica A: Statistical Mechanics and its Applications**, v. 362, n. 2, p. 277 – 288, 2006.

SIMOEN, E.; CLAEYS, C. On the flicker noise in submicron silicon {MOSFETs}. **Solid-State Electronics**, v. 43, n. 5, p. 865 – 882, 1999.

STOICA, P.; MOSES, R. L. **Introduction to spectral analysis**. [S.l.]: Prentice hall Upper Saddle River, NJ, 1997. v. 1.

SURDIN, M. Fluctuations de courant thermionique et le "flicker effect". **J. Phys. Radium**, v. 10, n. 4, p. 188–189, 1939.

SURYA, C.; HSIANG, T. Y. A thermal activation model for $1/f^y$ noise in Si-MOSFETs. **Solid-State Electronics**, v. 31, n. 5, p. 959 – 964, 1988.

TAKEUCHI, K. et al. Single-charge-based modeling of transistor characteristics fluctuations based on statistical measurement of rtn amplitude. In: **2009 Symposium on VLSI Technology**. [S.l.: s.n.], 2009. p. 54–55. ISSN 0743-1562.

TEDJA, S.; SPIEGEL, J. V. der; WILLIAMS, H. H. Analytical and experimental studies of thermal noise in mosfet's. **IEEE Transactions on Electron Devices**, v. 41, n. 11, p. 2069–2075, Nov 1994.

TEGA, N. et al. Increasing threshold voltage variation due to random telegraph noise in fets as gate lengths scale to 20 nm. In: **2009 Symposium on VLSI Technology**. [S.l.: s.n.], 2009. p. 50–51. ISSN 0743-1562.

TUINHOUT, H.; DUIJNHOVEN, A. Z. v. Evaluation of 1/f noise variability in the subthreshold region of MOSFETs. In: **2013 IEEE International Conference on Microelectronic Test Structures (ICMTS)**. [S.l.: s.n.], 2013. p. 87–92.

VAN DER WEL, A. et al. Relating random telegraph signal noise in metal-oxide-semiconductor transistors to interface trap energy distribution. **Applied Physics Letters**, AIP, v. 87, n. 18, p. 183507, 2005.

VANDAMME, L. K. J.; HOOGE, F. N. What Do We Certainly Know About 1/f Noise in MOSTs. **IEEE Transactions on Electron Devices**, v. 55, n. 11, p. 3070–3085, Nov 2008.

WANG, P. et al. $1/f$ noise in as-processed and proton-irradiated algan/gan hemts due to carrier number fluctuations. **IEEE Transactions on Nuclear Science**, v. 64, n. 1, p. 181–189, Jan 2017.

WEI, C.; XIONG, Y. Z.; ZHOU, X. Investigation of Low-Frequency Noise in N-Channel FinFETs From Weak to Strong Inversion. **IEEE Transactions on Electron Devices**, v. 56, n. 11, p. 2800–2810, Nov 2009.

WEISSMAN, M. B. $\frac{1}{f}$ and other slow, nonexponential kinetics in condensed matter. **Rev. Mod. Phys.**, American Physical Society, v. 60, p. 537–571, Apr 1988.

WELCH, P. The use of fast fourier transform for the estimation of power spectra: A method based on time averaging over short, modified periodograms. **IEEE Transactions on Audio and Electroacoustics**, v. 15, n. 2, p. 70–73, Jun 1967.

WIRTH, G. I.; DA SILVA, R.; BREDERLOW, R. Statistical model for the circuit bandwidth dependence of low-frequency noise in deep-submicrometer mosfets. **IEEE Transactions on Electron Devices**, v. 54, n. 2, p. 340–345, Feb 2007.

WIRTH, G. I. et al. Modeling of statistical low-frequency noise of deep-submicrometer mosfets. **IEEE Transactions on Electron Devices**, v. 52, n. 7, p. 1576–1588, July 2005.

WIRTH, G. I.; SILVA, R. da; KACZER, B. Statistical model for mosfet bias temperature instability component due to charge trapping. **IEEE Transactions on Electron Devices**, v. 58, n. 8, p. 2743–2751, Aug 2011.

WONG, H.; CHENG, Y. C. Study of the electronic trap distribution at the SiO2-Si interface utilizing the low-frequency noise measurement. **IEEE Transactions on Electron Devices**, v. 37, n. 7, p. 1743–1749, Jul 1990.

XIONG, H. D. et al. Temperature dependence and irradiation response of $1/f$-noise in MOSFETs. **IEEE Transactions on Nuclear Science**, v. 49, n. 6, p. 2718–2723, Dec 2002.

YAMAMOTO, Y. **Fundamentals of Noise Processes**. [S.l.]: Cambridge University Press, 2004.

YU, B. et al. Modeling local variation of low-frequency noise in MOSFETs via sum of lognormal random variables. In: **Proceedings of the IEEE 2012 Custom Integrated Circuits Conference**. [S.l.: s.n.], 2012. p. 1–4.

PUBLISHED WORK

BOTH, T. H.; FURTADO, G. F.; WIRTH, G. I. Modeling and Simulation of the Charge Trapping Component of BTI and RTS. **Microelectronics Reliability**, v. 80, p. 278-283, Jan 2018.

BOTH, T. H.; FURTADO, G. F.; WIRTH, G. I. A Compact Model for BTI Simulation under Cyclo-Stationary Conditions. In: **Microelectronics Technology and Devices (SBMicro), 2017 32nd Symposium on**. Fortaleza, 2017, pp. 1-4.

FURTADO, G. F.; BOTH, T. H.; WIRTH, G. I. Deterministic methodology to evaluate BTI impact on logic gates propagation delay. In: **Microelectronics Technology and Devices (SBMicro), 2017 32nd Symposium on**. Fortaleza, 2017, pp. 1-4.

FURTADO, G. F.; BOTH, T. H.; VIEIRA, M. ; WIRTH, G. I. Deterministic Methodology for Electrical Simulation of BTI Induced Pulse Broadening. **IEEE Transaction on Device and Materials Reliability**, v. 17, n. 3, p. 5017-5013, May 2017.

BOTH, T. H.; CROON, J. A.; BANASZESKI DA SILVA, M.; TUINHOUT, H. P.; ZEGERS-VAN DUIJNHOVEN, A.; SCHOLTEN, A. J.; WIRTH, G. I. A variability-based analysis technique revealing physical mechanisms of MOSFET low-frequency noise. In: **2017 IEEE International Conference on Microelectronic Test Structures (ICMTS)**. [S.l.: s.n.], 2017. p. 165-169. ISSN 1071-9032.

BOTH, T. H.; CROON, J. A.; BANASZESKI DA SILVA, M.; TUINHOUT, H. P.; ZEGERS-VAN DUIJNHOVEN, A.; SCHOLTEN, A. J.; WIRTH, G. I. Autocorrelation analysis as technique to study physical mechanisms of MOSFET low-frequency noise . **IEEE Transaction on Electron Devices**, vol. 64, n. 7, p. 2919-2926, Jul 2017.

BOTH, T. H.; WIRTH, G. I.; VASILESKA, D. 1/f noise simulation in MOSFETs under cyclo-stationary conditions using SPICE simulator. **Journal of Computational Electronics**, v. 14, n. 1, p. 15-20, 2015.

KASTENSMIDT, F. L.; TONFAT, J.; BOTH, T.; RECH, P.; WIRTH, G.; REIS, R.; BRUGUIER, F.; BENOIT, P.; TORRES, L.; FROST, C. Voltage scaling and aging effects on soft error rate in SRAM-based FPGAs. **Microelectronics Reliability**, v. 54, n. 9–10, p. 2344-2348, Sep-Oct 2014. ISSN 0026-2714.